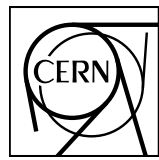


EUROPEAN ORGANIZATION FOR NUCLEAR RESEARCH



CERN-PH-EP-2016-3447
January 15, 2017 2016

Σ^0 and $\bar{\Sigma}^0$ Baryon Production in pp Collisions at $\sqrt{s} = 7$ TeV from the Analysis of 2010 Pass-4 ALICE Data

A. Borissov¹, H. Oelscher^{1,2}, J. Song¹, I.-K. Yoo¹

1. Pusan National University, South Korea
2. Physikalisches Institut, Ruprecht-Karls-Universität Heidelberg, Heidelberg, Germany

Email: Alexander.Borissov@cern.ch, Jihye.Song@cern.ch, Yoo@hipex.phys.pusan.ac.kr

Abstract

The first measurements of the $\Sigma^0 + \bar{\Sigma}^0$ transverse momentum spectrum, integrated yield and mean transverse momentum in pp collisions at $\sqrt{s} = 7$ TeV at the LHC are presented. The Σ^0 ($\bar{\Sigma}^0$) baryon is reconstructed via the decay of the Λ ($\bar{\Lambda}$) baryon into $p + \pi^-$ ($\bar{p} + \pi^+$) and γ conversion into an $e^+ + e^-$ pair using the unique capability of the ALICE detector to measure low energy photons. The yield of the Σ^0 is compared to that of Λ baryons, which have the same quark content but different isospin. The yields are also compared to results from simulations using the pQCD based PYTHIA event generator. These data contribute to the understanding of hadron production mechanisms and provide a reference for constraining pQCD inspired models and tuning the corresponding event generators.

17 Contents

18	1 Introduction	4
19	1.1 Motivations for the analysis of Σ^0 from pp collisions	4
20	1.2 Relevant indico presentations	4
21	1.3 Analysis framework	5
22	1.4 Data sample	5
23	1.5 Monte Carlo sample	6
24	1.6 Event selection	7
25	2 Detection of $\Sigma^0(\bar{\Sigma}^0) \rightarrow \Lambda(\bar{\Lambda}) + \gamma$ decay	8
26	2.1 $\Lambda(\bar{\Lambda})$ selection	8
27	2.2 γ^{PCM} selection	9
28	3 Raw yields of Σ^0 and $\bar{\Sigma}^0$ baryons	13
29	3.1 Signal extraction	13
30	3.2 Mass of Σ^0 and/or $\bar{\Sigma}^0$ hyperons	15
31	4 Monte Carlo simulations and correction factors	16
32	5 $\Sigma^0 p_T$-spectrum from pass-2 and pass-4 productions	18
33	6 Optimization of p_Tbins	21
34	7 Systematic uncertainties	22
35	7.1 Systematic uncertainty of Λ detection	22
36	7.2 Systematic uncertainty of γ detection	25
37	7.3 Systematic uncertainty of $\Sigma^0 + \bar{\Sigma}^0$ yield extraction	26
38	7.4 Total systematic uncertainties	26
39	8 Fitted $\Sigma^0 p_T$spectrum	30
40	8.1 World data on $\frac{\Sigma^0}{\Lambda}$ cross section ratio	34
41	9 Summary	35
42	10 References	36
43	11 Appendices	38
44	11.1 Comparison of selected events with the analysis of PCM group	38

45	11.2 Run lists used for the comparison of pass-2 and pass-4 productions of 2010 pp data	39
46	11.3 Optimization of p_T -bins of Σ^0 spectrum	40
47	11.4 Systematic studies of Λ detection	41
48	11.5 Systematic studies of γ detection	45
49	11.6 Fits of Σ^0 spectrum resulting to large values of χ^2/NDF	49
50	11.7 ALICE Preliminary plots of Σ^0 and/or $\bar{\Sigma}^0$ mass and width	50
51	11.8 $\Sigma^0 \rightarrow \Lambda + \gamma^{PHOS}$ from 2011 d+e data	52

52 1 Introduction

53 Below, for brevity, we refer on Σ^0 as for both Σ^0 and $\bar{\Sigma}^0$ baryons.

54 1.1 Motivations for the analysis of Σ^0 from pp collisions

55 *Those who are only interested to the details of the analysis can skip this section.*

56 The main items of Σ^0 analysis in pp data are presented below.

- 57 – Tests of pQCD and current parametrization of fragmentation functions from comparison with sim-
58 ulations. Substantial disagreement of Λ transverse momentum distributions in pp data at 0.9 and
59 7 TeV with Monte Carlo (MC) predictions was observed in ALICE, see Ref. [1, 2] and ATLAS
60 publication in Ref. [3]. See section 7 for a comparison of data and MC for Σ^0 .
- 61 – Measurement of cross section ratios. Is the cross section ratio $\Sigma^0/\Lambda = 0.33$ at LHC energies?
62 Note the quite limited data on the Σ^0/Λ ratio, see subsection 8.1 for current results and world data
63 presented in Refs. [4–6].
- 64 – Comparison of the yield ratios Σ^0/Λ and $\Sigma^0/\Sigma(1385)^{\pm}$ with THERMUS and EPOS model calcu-
65 lations.
- 66 – Discrimination of prompt and decay hyperons, e.g. prompt Λ and one from Σ^0 decay. Con-
67 tamination of Σ^0 decay products ($p\pi^+$, $\bar{p}\pi^-$) in the transverse momentum spectrum of charged
68 particles [7].
- 69 – Contamination of photon from Σ^0 decay in the low-momentum part of the spectrum of direct
70 photons.
- 71 – Estimation of contamination and dilution of Λ from Σ^0 decay in the Λ polarization measurement,
72 see Refs. [8, 9].
- 73 – Note measurement of Σ^0 polarization in p-Be collisions at intermediate energies [10].
- 74 – Σ^0 is an additional observable for the enhancement of strange baryon production at very high
75 multiplicity in pp data at 7 and 13 TeV, see Refs. [2, 11, 12].

76 1.2 Relevant indico presentations

77 The plots of invariant mass distributions of Σ^0 and $\bar{\Sigma}^0$ have been presented from pass-2 2010 pp data
78 at $\sqrt{s}=7$ TeV as ALICE Preliminary figures at Quark Matter 2014, see Ref. [13]. The same data and
79 analysis subroutines have been used for Σ^0 spectrum analysis, the results of which are presented in
80 Ref. [14]. The 2010 pass-4 pp data at $\sqrt{s}=7$ TeV, available since fall 2015, are used in the current
81 analysis.

82 Here is a list of relevant talks presented in PAG-Resonance meetings presented in reverse chronological
83 order for pass-4 2010 pp data:

84 RSN meeting 16.11.2016 <https://indico.cern.ch/event/588521/>

85 RSN meeting 02.11.2016 <https://indico.cern.ch/event/581243/>

86 RSN meeting 24.08.2016 <https://indico.cern.ch/event/564543/>

87 RSN meeting 20.07.2016 <https://indico.cern.ch/event/556850/>

88 RSN meeting 27.04.2016 <https://indico.cern.ch/event/524657/>

89 RSN meeting 03.02.2016 <https://indico.cern.ch/event/492276/>

90 RSN meeting 04.11.2015 <https://indico.cern.ch/event/459268/>.

91 Pass-2 data have been analyzed with an almost fully independent approach, have been presented many
92 times and reported on RSN meetings in 2013–2015, and summarized in the analysis notes: [13, 14].

93 1.3 Analysis framework

94 Codes for ESD based Σ^0 analysis updated for pass-4 2010 data and Monte Carlo production can be found
95 in
96 \$ALICE_PHYSICS/PWGGA/Hyperon/AliAnalysisTaskSigma0.cxx (h)
97 and AliAnalysisTaskSigma0Spectra.cxx (h).

98 The following software packages have been used for the analysis:

99 AliPhysics: vAN-20160131-1

100 AliRoot: v5-07-20-4

101 Root: v5-34-30.

102

103 1.4 Data sample

104 The data analysis is carried out using a total sample of 542 million events which have been readout in
105 ALIROOT UserExec subroutine from pp collisions at $\sqrt{s} = 7$ TeV collected during the 2010 run at the
106 LHC from the pass-4 production. Number of minimum-bias events is presented in Appendix 11.1.

107 The run numbers for this analysis are the same used in the analysis of direct photons using the Photon
108 Conversion Method (PCM), see the analysis note [15]. Note that these runs (presented below) have been
109 checked for the detection of direct photons by means of PCM [15]. The run list includes:

110

111 42 runs from LHC10b:

112 114786 114798 114918 114920 114924 114931 115186 115193 115310 115318 115322 115328 115335
113 115345 115393 115399 115401 116079 116081 116102 116288 116402 116403 116562 116571 116574
114 116643 116645 117048 117050 117052 117053 117059 117060 117063 117092 117099 117109 117112
115 117116 117220 117222,

116

117 36 runs from LHC10c:

118 119159 119161 119163 119841 119842 119844 119845 119846 119849 119853 119856 119859 119862
119 120067 120069 120072 120073 120076 120079 120244 120503 120504 120505 120616 120617 120671
120 120741 120750 120758 120820 120821 120822 120823 120824 120825 120829,

121

122 57 runs from LHC10d:

123 122374 122375 124751 124850 125083 125085 125097 125100 125133 125134 125139 125140 125156
124 125186 125295 125296 125630 125632 125842 125843 125847 125848 125849 125850 125851 125855
125 126004 126007 126008 126073 126078 126081 126082 126088 126090 126097 126158 126160 126167
126 126168 126283 126284 126285 126351 126352 126359 126403 126404 126405 126406 126407 126408
127 126409 126422 126424 126425 126432,

128 119 runs from LHC10e:

129 128366 128452 128494 128495 128498 128503 128504 128505 128506 128582 128590 128592 128594
130 128596 128605 128609 128611 128615 128621 128677 128678 128777 128778 128819 128820 128823
131 128824 128833 128834 128835 128836 128843 128850 128853 128855 128913 129042 129512 129513
132 129514 129515 129516 129519 129520 129521 129523 129524 129525 129527 129528 129536 129540
133 129586 129587 129599 129639 129641 129647 129650 129651 129652 129653 129659 129666 129723
134 129726 129729 129734 129735 129736 129738 129742 129744 129959 129960 129961 129962 129966
135 130149 130151 130157 130158 130168 130172 130178 130342 130343 130354 130356 130358 130360
136 130375 130480 130481 130517 130519 130520 130524 130526 130601 130608 130609 130620 130621
137 130623 130628 130696 130704 130793 130795 130798 130799 130834 130840 130842 130844 130847

138 130848 130850,

139

140 14 runs from LHC10f:

141 133006 133007 133010 133327 133329 133330 133414 133563 133670 133762 133800 133920 133969

142 133982.

143 1.5 Monte Carlo sample

144 All runs are from pass-4 Monte Carlo productions for 2010 pp data. The PYTHIA Perugia-2011 generator has been used. In total 526 million reconstructed events have been readout in ALIROOT UserExec subroutine. Number of simulated minimum-bias events is presented in Appendix 11.1.

147 It includes:

148 45 runs from LHC14j4b:

149 114786 114798 114918 114920 114924 114930 114931 115186 115193 115310 115318 115322 115328
150 115335 115345 115393 115399 115401 115414 115521 116079 116081 116102 116288 116402 116403
151 116562 116571 116574 116643 116645 117048 117050 117052 117053 117059 117060 117063 117092
152 117099 117109 117112 117116 117220 117222,

153

154 45 runs from LHC14j4c:

155 118506 118507 118512 118518 118556 118558 118560 118561 119159 119161 119163 119841 119842
156 119844 119845 119846 119849 119853 119856 119859 119862 120067 120069 120072 120076 120079
157 120244 120503 120504 120505 120616 120617 120671 120741 120750 120758 120820 120821 120822
158 120823 120824 120825 120829 121039 121040,

159

160 62 runs from LHC14j4d:

161 122374 122375 124751 125023 125083 125085 125097 125100 125101 125133 125134 125139 125140
162 125156 125186 125295 125296 125628 125630 125632 125633 125842 125843 125844 125847 125848
163 125849 125850 125851 125855 126004 126007 126008 126073 126078 126081 126082 126088 126090
164 126097 126158 126160 126167 126168 126283 126284 126285 126350 126351 126352 126359 126403
165 126404 126405 126406 126407 126408 126409 126422 126424 126425 126432,

166

167 123 runs from LHC14j4e:

168 128366 128452 128486 128494 128495 128498 128503 128504 128505 128506 128582 128590 128592
169 128594 128596 128605 128609 128611 128615 128621 128677 128678 128777 128778 128819 128820
170 128823 128824 128833 128834 128835 128836 128843 128850 128853 128855 128913 129042 129512
171 129513 129514 129515 129516 129519 129520 129521 129523 129524 129525 129527 129528 129536
172 129540 129586 129587 129599 129639 129641 129647 129650 129651 129652 129653 129659 129666
173 129723 129725 129726 129729 129734 129735 129736 129738 129742 129744 129959 129960 129961
174 129962 129966 129983 130149 130151 130157 130158 130168 130172 130178 130342 130343 130354
175 130356 130358 130360 130375 130479 130480 130481 130517 130519 130520 130524 130526 130601
176 130608 130609 130620 130621 130623 130628 130696 130704 130793 130795 130798 130799 130834
177 130840 130842 130844 130847 130848 130850,

178

179 and 16 runs from LHC14j4f production:

180 133006 133007 133010 133327 133329 133330 133414 133563 133670 133762 133800 133920 133969
181 133982 134198 134297.

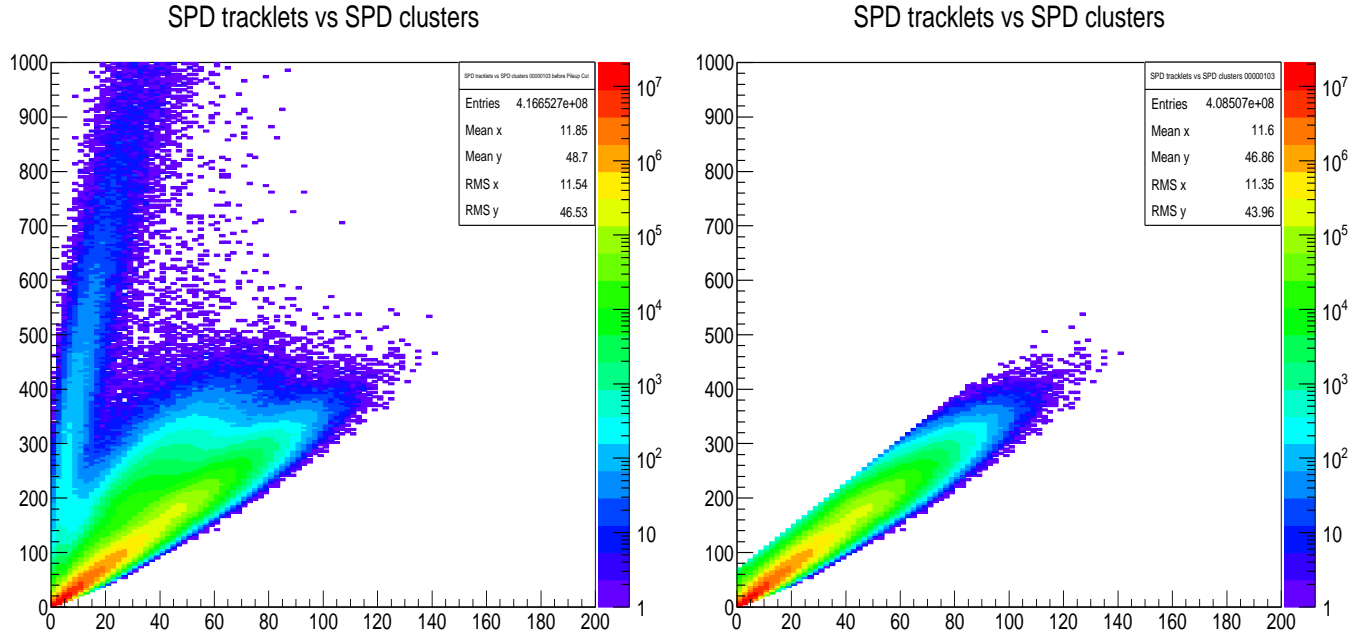


Fig. 1: SPD based event selection before (left) and after (right) restriction on pileup.

182 1.6 Event selection

183 Event selection is based on the application of the
 184 `/aliphysics/master/src/PWGGA/GammaConv/AliV0ReaderVI.cxx` package. This approach was used for
 185 ALICE publications [16, 17].

186 The following event selections have been performed:

- 187 – V0OR trigger hit in either of two VZERO detectors,
- 188 – events with $|Z_{\text{Vertex}}| < 10$ cm were accepted,
- 189 – vertex is reconstructed, if global tracks or only Silicon Pixel Detector (SPD) tracklets contribute
 190 to the vertex,
- 191 – pileup events were rejected on the base of SPD data, see Fig. 1.

192 For the details of the event selection used for Σ^0 analysis see Appendix 11.1 and a dedicated presentation
 193 at the RSN meeting on 20.07.2016. The data and MC productions for the current analysis have been
 194 compared with the analysis from the PCM group [15]. The results of this comparison are presented in
 195 Appendix 1.1 and are in full agreement with each other.

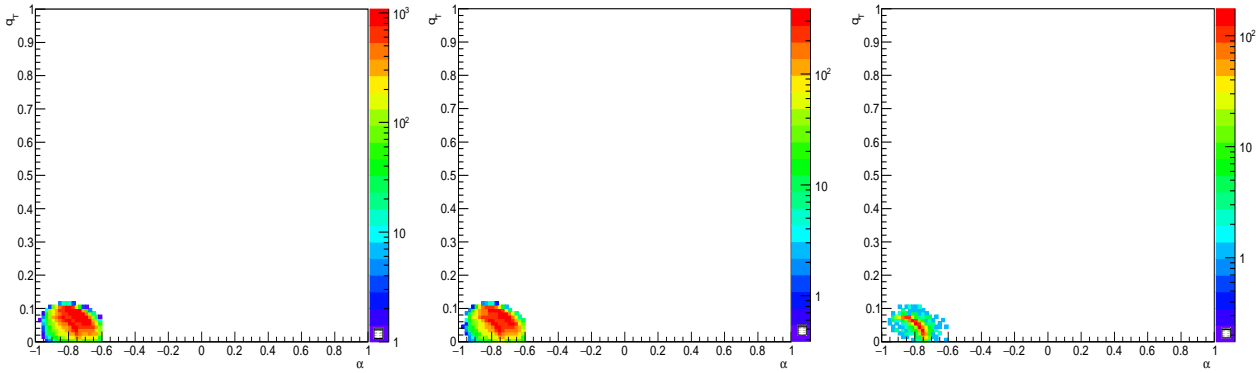


Fig. 2: Armenteros-Podolanski distributions of selected $\Sigma^0 + \bar{\Sigma}^0$ entries from the data (left), reconstructed simulated events (middle) and simulated “true” $\Sigma^0 + \bar{\Sigma}^0$.

196 2 Detection of $\Sigma^0(\bar{\Sigma}^0) \rightarrow \Lambda(\bar{\Lambda}) + \gamma$ decay

197 The $\Sigma^0(1192) \rightarrow \Lambda + \gamma$ and $\bar{\Sigma}^0(1192) \rightarrow \bar{\Lambda} + \gamma$ electromagnetic decay, which has a branching ratio of
 198 100 % was reconstructed. (Note, that $\Sigma^0(1192)$ consists of uds quarks and has isospin 1, $c\tau = 22\,200$
 199 fm.) The decay of $\Lambda(1115) \rightarrow p + \pi^-$, $\bar{\Lambda}(1115) \rightarrow \bar{p} + \pi^+$ with a branching ratio $\sim 64\%$ and $c\tau = 7.89$
 200 cm is measured from the secondary vertex (V0) of the daughter tracks, $p(p)$ and $\pi^-(\pi^+)$. Tracks from
 201 the secondary vertex (V0) are reconstructed in the ALICE tracking system, which consists of the Inner
 202 Tracking System (ITS) and the Time Projection Chamber (TPC) [19]. The combined acceptance of the
 203 ITS and TPC is $|\eta| < 0.9$. The pairs of tracks are selected using a secondary vertex finding algorithm
 204 which is described in detail in Refs. [19–21]. The photon is measured through its conversion to an e^+e^-
 205 pair using Photon-Conversion Method (PCM) through application of the V0ReaderV1 package described
 206 below. The restrictions on Λ and γ selections are described below.

207 The invariant mass of Λ and γ was calculated from each independently accumulated Λ and γ entry in
 208 the same event. An Armenteros-Podolanski cut on Σ^0 : $\alpha > 0.6 \&& q_T < 0.12$ was applied, see Fig. 2,
 209 where $\alpha = |\frac{p_\gamma^\gamma - p_\Lambda^\Lambda}{p_\gamma^\gamma + p_\Lambda^\Lambda}|$, where p_l^i is the longitudinal momentum of a particle i (γ or Λ) with respect to the Σ^0
 210 momentum direction. q_T corresponds to transverse momentum of Λ with respect to the Σ^0 momentum.
 211 For each combination of Λ and γ an entry to TTTree based output and quality assurance histograms was
 212 written. Note that the impact of the variation of Armenteros-Podolanski limits on the selected Σ^0 entries
 213 was studied in notes[13, 14].

214 For the comparison with Λ transverse momentum spectra, the rapidity range of detected Σ^0 is taken to be
 215 the same as for Λ : $|\Delta y| < 0.5$. The p_T range of detected Σ^0 is between 1.1 and 8 GeV/c. The p_T binning
 216 is determined by the statistics of the events, see section 4. Current bins of p_T are the following:
 217 $1.1 \div 1.6 \div 2.0 \div 2.4 \div 2.8 \div 3.4 \div 4.0 \div 5.0 \div 8.0$ GeV/c.

218 2.1 $\Lambda(\bar{\Lambda})$ selection

219 The Λ from Σ^0 decay is reconstructed with almost the same cuts as in the stand-alone subroutine in the
 220 analysis of D.D.Cinellato (Ref. [1, 22]). The cuts in that subroutine use a similar approach as in the
 221 official codes in /PWGLF/STRANGENESS/LambdaK0/AliAnalysisTaskExtractV0.cxx.

222 $\Lambda(\bar{\Lambda})$ is detected from V0 and invariant mass analysis using a secondary vertex finding algorithm, see
 223 Fig. 3 for the reconstructed invariant mass and p_T distributions. The following restrictions have been
 224 applied to select Λ from the V0 vertex in the tracking system.

225 V0 vertex was accepted if:

226 - V0 finder is on-the fly,

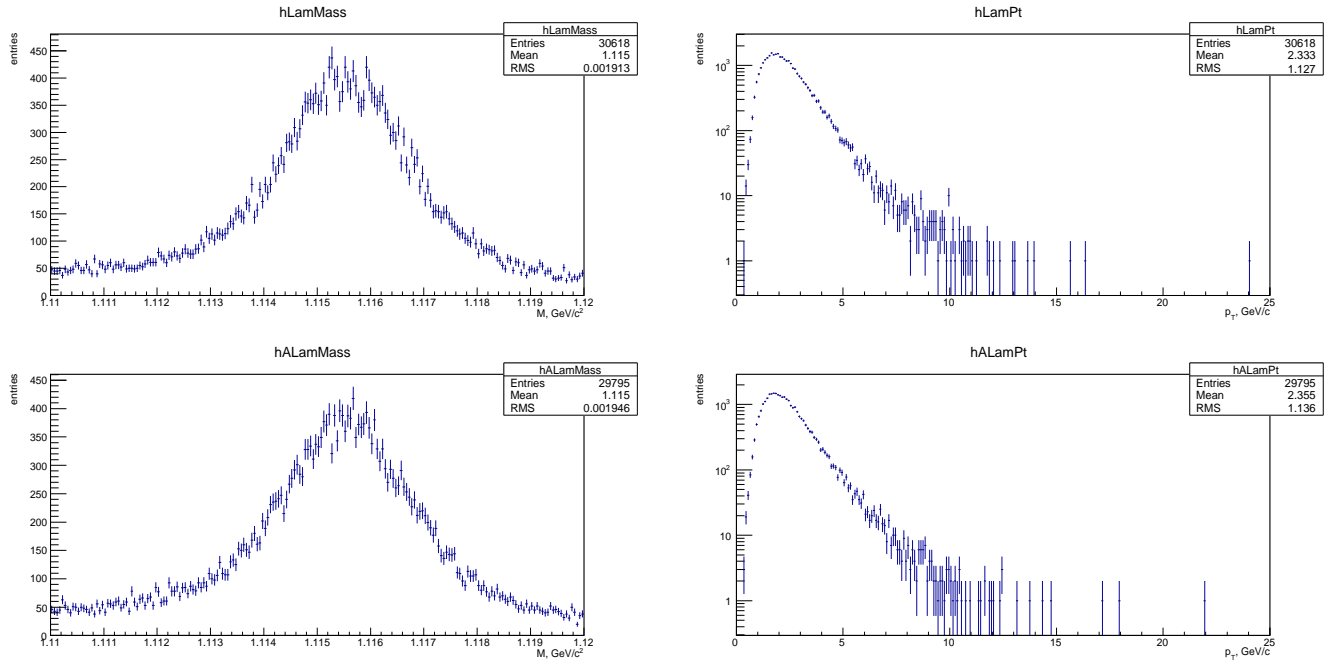


Fig. 3: Invariant mass and p_T distributions of selected Λ and $\bar{\Lambda}$ entries.

- no kink for the track with negative charge,
 - no kink for the track with positive charge,
 - positive TPC track was refitted,
 - negative TPC track was refitted,
 - distance of closest approach (DCA) between positive track and primary vertex > 0.06 cm,
 - DCA between negative track and primary vertex > 0.06 cm,
 - $\cos PA_{\Lambda} > 0.993$, where PA is pointing angle,
 - V0 radius $= \sqrt{x_{V0}^2 + y_{V0}^2} < 180$ cm
 - Λ satisfies the following Armenteros-Podolanski cuts: $0.2 < \alpha < 0.9 \& 0.01 < q_T < 0.17$,
 - $\bar{\Lambda}$ satisfies the following Armenteros-Podolanski cuts: $-0.9 < \alpha < 0.2 \& 0.01 < q_T < 0.17$
 - Λ and $\bar{\Lambda}$ invariant mass window $1.110 < M < 1.120$ GeV/ c^2 .
- Distributions of the α and q_T variables for Λ and $\bar{\Lambda}$ are presented in Fig. 4 and are in good agreement with each other. Note that more tighter restrictions on Λ result in the reduction of Σ^0 entries.

2.2 γ^{PCM} selection

The photon is detected with the application of Photon Conversion Method (PCM) from their conversion in the material of the inner detectors and reconstructed via the e^+e^- pairs which is described in detail in Ref. [23]. The main feature of the Σ^0 electromagnetic decay is the low energy of the photon, $E_{min}^{\gamma} = 77$ MeV. Correspondingly, the mean energy of photon is $\langle E^{\gamma} \rangle \approx 100$ MeV. Such small energy limits the detection of photons from Σ^0 decays in the electromagnetic calorimeter EMCAL due to its resolution and noise. The Σ^0 invariant mass distribution with photon detected in the PHOS is presented in appendix 11.8 in Fig. 59. The very large p_T -bin used for the observation of the Σ^0 invariant mass peak practically does not allow reconstruction of its transverse momentum spectrum on the basis of PHOS data. Therefore, Σ^0 and $\bar{\Sigma}^0$ baryons were reconstructed with the photon detected in PHOS for proof-of-principle only, with much smaller statistics relative PCM [13].

Photon conversion in the material of the inner detectors is reconstructed via the e^+e^- pairs in the central tracking system, see Fig. 5 left plot. Probability of photon conversion in central tracking system is

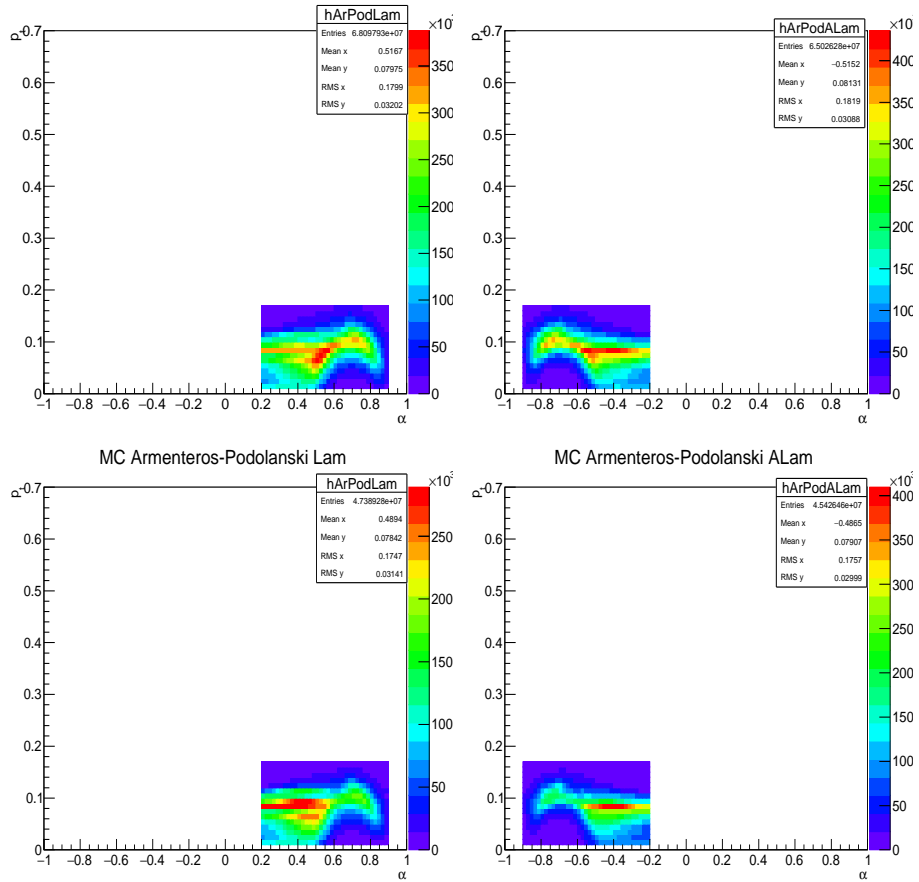


Fig. 4: Armenteros-Podolanski distributions of selected Λ (left plots) and $\bar{\Lambda}$ (right plots) entries. Top plots are from the data, bottom plots are from the simulations.

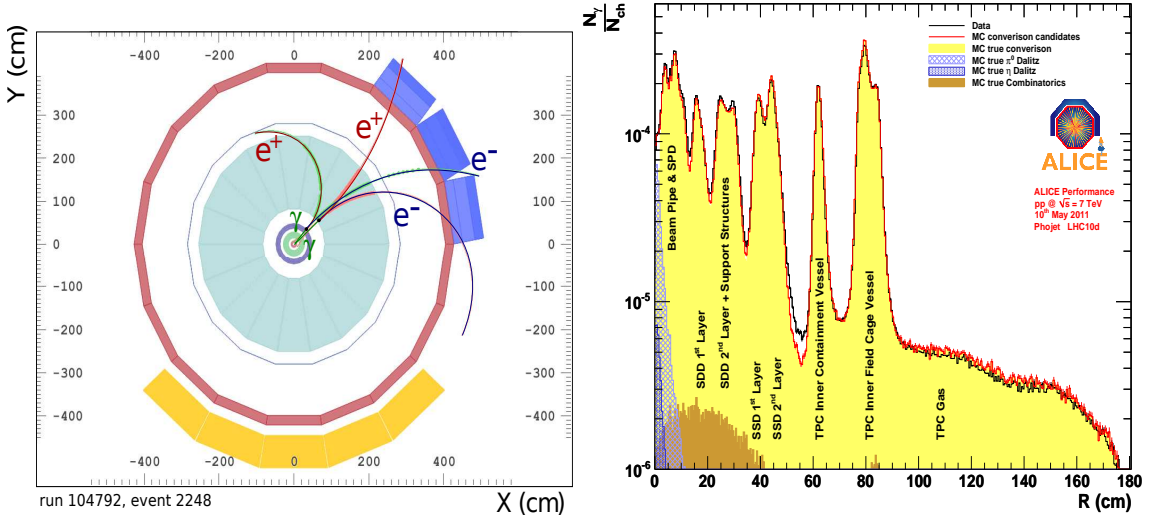


Fig. 5: Schematic representation of the detection of conversion photon.

253 ~ 0.08 ; the reconstruction efficiency is about 0.67 [15, 16]. Note, that ALICE material budget is well
254 described in GEANT, see Fig. 5 right plot.

255 The Aliroot PCM package from `/PWGGA/GammaConv/AliV0ReaderVI.cxx` was applied to the final se-
256 lection of photon from pp data without the tuning of the cuts applied there. This package is described in
257 full detail by PCM group, see Ref [23]. Before, the local and less detailed subroutine
258 (`/PWGGA/GammaConv/AliAnalysisTaskCaloConv.cxx`) was used instead. Nevertheless, the results of Σ^0
259 detection are consistent between final and previous method of photon detection for the Σ^0 yield extrac-
260 tion. The final version of the PCM package provides a smaller background under the Σ^0 invariant mass
261 peak.

262 The following restrictions have been applied to select the photon from its conversion in the tracking sys-
263 tem for pp collisions. Electron and secondary track cuts:

- 264 - accept $\eta_e < 0.90$
- 265 - accept: $0.00 < \phi < 6.28$ with $-0.90 < \eta < 0.90$
- 266 - $p_{T,e} > 0.05$
- 267 - TPC refit: no kinks
- 268 - accept: $-6.00 < n\sigma_{e,TPC} < 7.00$
- 269 - reject: $0.50 < p_{T,e} < 100.00$, at $n\sigma_{pi,TPC} < -10.00$
- 270 - reject: $p_{T,e} > 100.00$, at $n\sigma_{pi,TPC} < -10.00$
- 271 - reject: $p_{T,e} < 0.50$, at $-1.00 < n\sigma_{pi,TPC} < 1.00$
- 272 - reject: $-1.00 < n\sigma_{K,TPC} < 1.00$
- 273 - reject: $-1.00 < n\sigma_{K,TPC} < 1.00$.

274 Photon cuts:

- 275 - using Onfly V0 finder
- 276 - 2 dimensional q_T cut applied with maximum of 0.06
- 277 - 2 dimensional triangle χ^2 and ψ_{pair} cut applied with maximum of $\chi^2 = 30.00$ and $|\psi_{pair}| = 0.20$
- 278 - $5.00 < R_{conv} < 180.00$, $-Z_{conv} < 1000.00$, $-\eta_{conv} < 0.90$
- 279 - for $p_{T,track} > 3.50$, $A_\gamma < 0.06$
- 280 - cluster TPC/ findable clusters TPC (corrected for radius) > 0.35
- 281 - $p_{T,\gamma} > 0.02$
- 282 - $-\cos(\Theta_{point}) > -1.00$,
- 283 - $DCA_R < 1000.00$,
- 284 - $DCA_Z < 1000.00$.

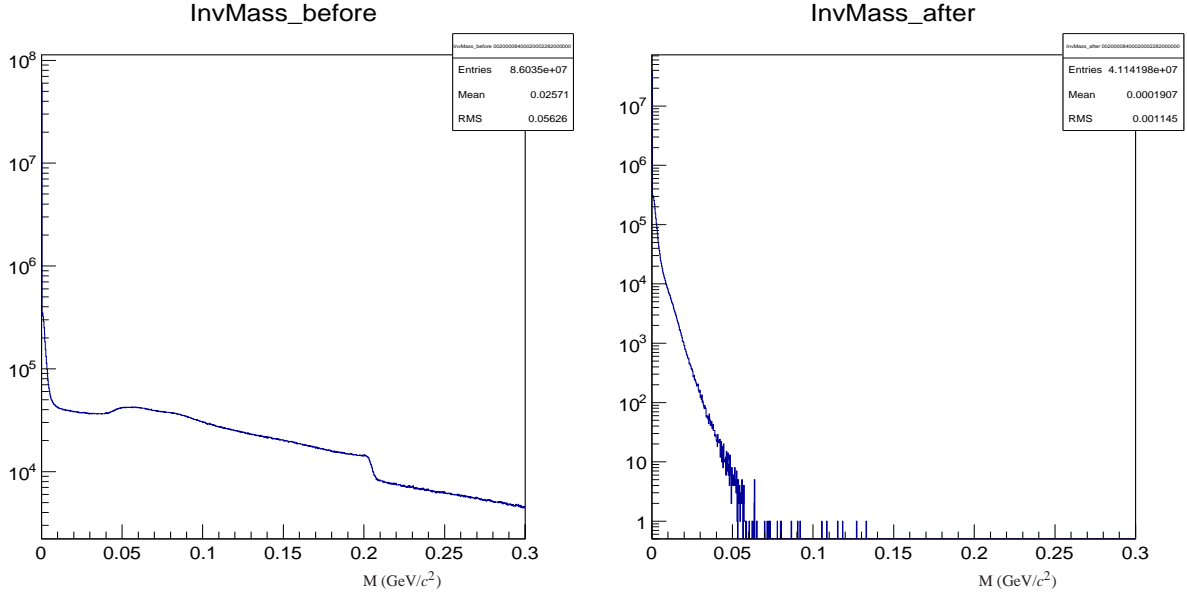


Fig. 6: Invariant mass distributions before and after application of the cuts for photon selection.

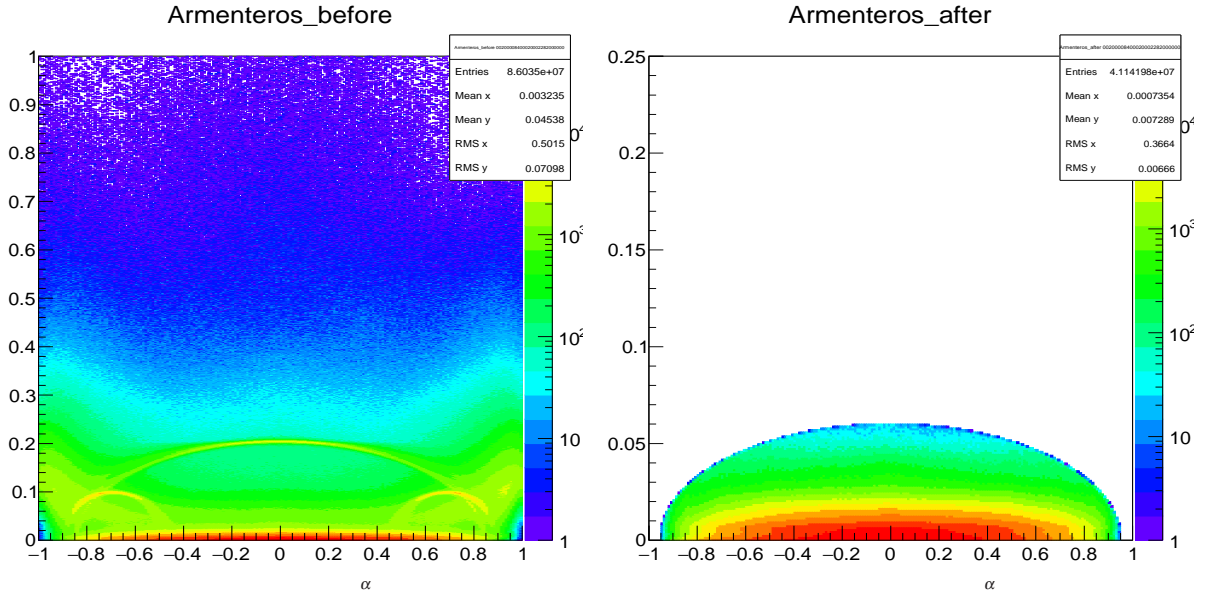


Fig. 7: Armenteros-Podolanski distributions (α vs p_t) before and after application of the cuts for photon selection.

285

286 The invariant mass distribution of reconstructed conversion photons before and after application of the
 287 cuts for selection of conversion photons is presented in Fig. 6. The Armenteros-Podolanski plot before
 288 and after application of the cuts for selection of conversion photons is shown in Fig. 7.

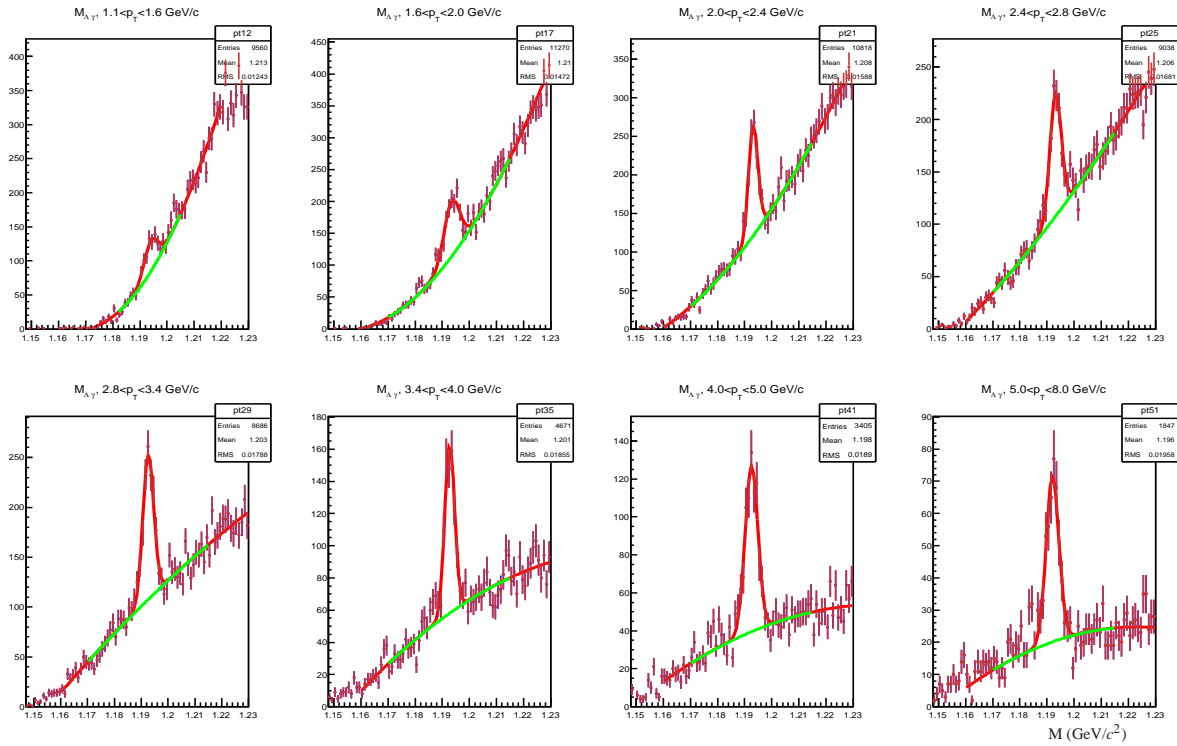


Fig. 8: Second-order polynomial fitted background plus Gauss fit of invariant mass $M_{\gamma\Lambda}$ and $M_{\gamma\bar{\Lambda}}$ of the detected conversion photon and Λ ($\bar{\Lambda}$) from 2010 pass-4 pp data.

289 3 Raw yields of Σ^0 and $\bar{\Sigma}^0$ baryons

290 3.1 Signal extraction

291 The second-order polynomial fitted background and Gauss fitted signal are presented in Fig. 8 for the
 292 combination of Σ^0 and $\bar{\Sigma}^0$. In Fig. 9 the reconstructed simulated events are presented with the combinatorial
 293 background distributions of Σ^0 invariant mass peaks. For the data and MC samples, the background
 294 was fitted in the range of $1.160 \div 1.230 \text{ GeV}/c^2$, the region between $1.175 \div 1.210$ was used for the
 295 search for the peak of invariant mass.

296 Note the significant statistical fluctuations of the residual background at the application of the mixed
 297 event background, see Fig. 10. The mixed-event background distributions were normalized to two fixed
 298 regions around Σ^0 mass peak, namely $1.160 < M_{bg} < 1.170$ and $1.210 < M_{bg} < 1.230 \text{ GeV}/c^2$. Its
 299 normalization was cross checked with another two regions, $1.17 < M_{bg} < 1.178$ and $1.207 < M_{bg} < 1.230$
 300 GeV/c^2 . Due to the much larger statistics on the right part of Σ^0 mass peak the results of the normalization
 301 of mixed background were stable. The Σ^0 ($\bar{\Sigma}^0$) invariant mass was calculated with photons from the
 302 previous events and Λ ($\bar{\Lambda}$) from the current event. The mixed event sample has been accumulated at
 303 the same $|\delta y| < 0.5$ range as for the Σ^0 ($\bar{\Sigma}^0$) candidates. Note that for both fits the value of $\chi^2/ndf \approx 1$
 304 and is always less than two. This indicates that the application of the second-order polynomial fit for the
 305 background and Gauss fits for the invariant mass distribution is sufficient given the current statistics. It
 306 was checked, that the application of third-order polynomial fit of the background and Gaussian fits for the
 307 invariant mass distribution provides very similar results as the application of the second-order polynomial
 308 fit of the background and Gaussian fit of the signal. Therefore, due to the quite small statistics and
 309 significant statistical fluctuations of the entries in the peak region and residual background the second-
 310 order polynomial fit of the background and the Gaussian fit of the invariant mass peak was chosen for
 311 the extraction of the preliminary Σ^0 spectrum. The variations of background subtraction method and
 312 counting of the Σ^0 yield are considered as a systematic uncertainty, see below.

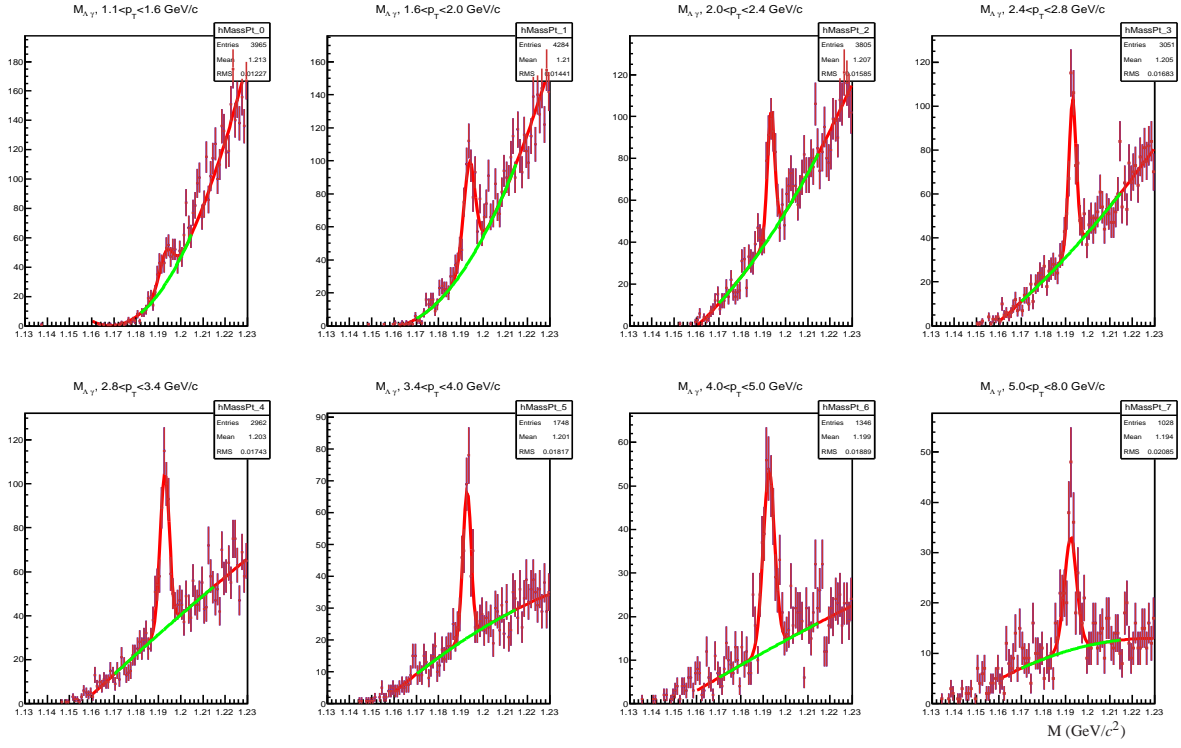


Fig. 9: Simulated events with the Gauss fit of signal of invariant mass of the detected conversion photon and Λ from 2010 pass 2 pp data in the $2.4 < p_T < 2.8$ GeV/c region. The invariant mass distribution after the background subtraction is presented on the bottom part of the plot.

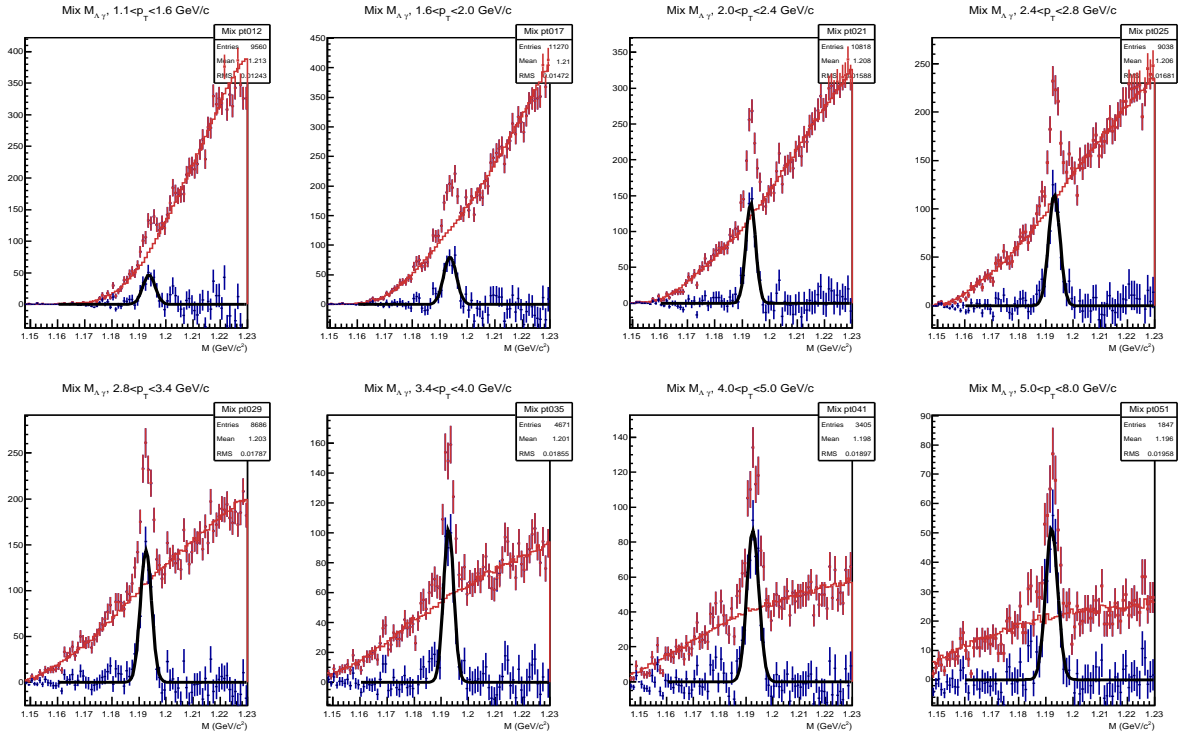


Fig. 10: Mixed background and Gaussian fit of invariant mass $M_{\Lambda\gamma}$ and $(M_{\bar{\Lambda}\gamma})$. The invariant mass distribution after the background subtraction is presented on the bottom part of the plot.

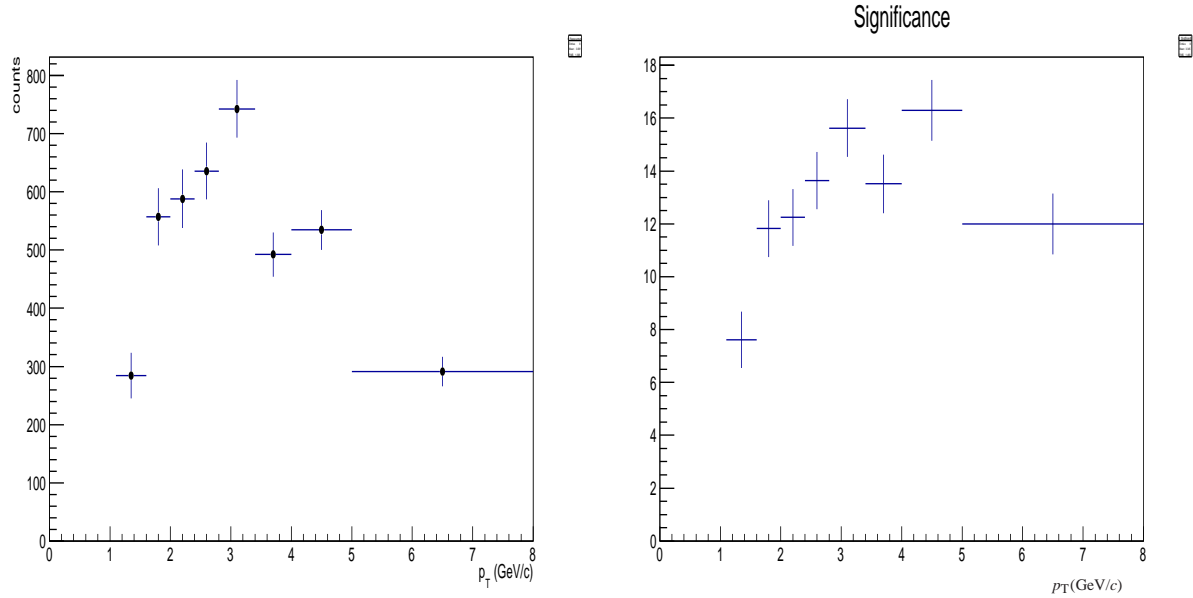


Fig. 11: Σ^0 yields after second-order polynomial background subtraction and Gauss fit of invariant mass of the detected conversion photon and Λ ($\bar{\Lambda}$) from 2010 pp data is on the left panel. Significance of Σ^0 yield is on the right panel.

- 313 The raw yields of $\Sigma^0 + \bar{\Sigma}^0$ hyperons after application of the two methods of background subtraction have
 314 been found using tow methods: the Gaussian fit of the Σ^0 invariant mass peak and bin counting. The raw
 315 yields for the 2010 pp data are presented in Fig. 11 left plot. The statistical uncertainty of the Σ^0 yields
 316 is quite large, it is in the range between 3.5 and 8 % in different bins of p_T . Note, that the applications of
 317 different method (signal yield counting) provided quite similar results, see section 6.
- 318 The significance of the Σ^0 signal is presented on the right plot of Fig. 11. It was calculated in the same
 319 way as in Ref. [24], where the value of significance is defined as $S/\sqrt{S+Bg}$, where S is the number of
 320 signal and Bg is the number of background events. Note that smallest significance is in the lowest p_T -bin
 321 ≈ 8 .
- 322 **3.2 Mass of Σ^0 and/or $\bar{\Sigma}^0$ hyperons**
- 323 The analysis of the mass and the width of the invariant mass peak, determined by the detector resolution,
 324 of Σ^0 and/or $\bar{\Sigma}^0$ hyperons from 2010 pass-2 pp data and MC production samples is presented in details
 325 in Ref. [13]. Here the results are also shown from pass-4 production of 2010 pp data.
- 326 The mean value of the fitted invariant mass distributions of combined Σ^0 and $\bar{\Sigma}^0$ data in different p_T bins
 327 are presented in Fig. 12 as black points. The mean value of the fitted invariant mass distributions of
 328 combined Σ^0 and $\bar{\Sigma}^0$ data from the simulation are presented in Fig. 12 as red points. The mean fitted
 329 value of Σ^0 mass $M = 1.19282 \pm 5.75358e - 05$ is in agreement with PDG [25]. Note that the small
 330 change of the mass with p_T is described by simulations due to the energy loss of electrons or positrons
 331 in the TPC, see Fig. 13. Good agreement of the simulated values of the Σ^0 mass and width with the data
 332 allows application of the Monte Carlo productions to the data for acceptance and efficiency corrections.
- 333 The approved plots from the pass-2 2010 pp data production are presented in the appendix 11.7 for sep-
 334 arated and combined and Σ^0 and $\bar{\Sigma}^0$ data in Figs. 55, 56, 57, 58 before and after background subtraction.

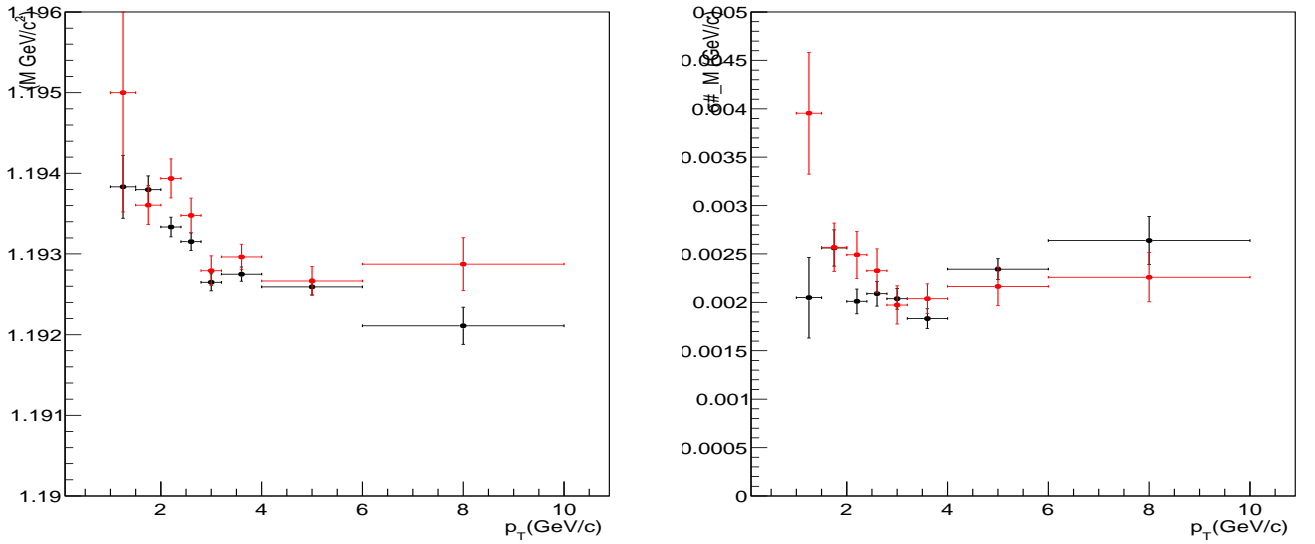


Fig. 12: Σ^0 mass (left) and width (right) after second-order polynomial background subtraction and Gauss fit of invariant mass of the detected conversion photon and Λ , $\bar{\Lambda}$ from pass-4 2010 pp data. Black points correspond to the data, red point to the simulated events. (Layout of the plots will be tuned.)

335 4 Monte Carlo simulations and correction factors

336 A simulated data set is used to get additional information needed to complete the analysis of the Σ^0 p_T
337 spectra in the real data. The main results of the application of Monte Carlo productions are Σ^0 ($\bar{\Sigma}^0$) re-
338 construction efficiency \times acceptance. A closure check for the analysis procedure: running the full analysis
339 on MC data should give a reconstructed Σ^0 spectrum that agrees with the generated spectrum. Due to the
340 limited statistics of the Σ^0 yields, the combined data from the 2010 pass-4 MC productions for pp data
341 have been used:
342 LHC14j4b+LHC14j4c+LHC14j4d+LHC14j4e+LHC14j4f.

343 Acceptance and efficiency corrections are calculated as the ratio of the reconstructed Gauss fit of the
344 invariant mass of simulated 'true' reconstructed Σ^0 ($\bar{\Sigma}^0$) decays to the generated number of Σ^0 in each p_T
345 bin for a given size Δp_T at $|y| < 0.5$:

$$346 \varepsilon(\Delta p_T, \Delta y) = \frac{N_{rec}(\Delta p_T, \Delta y)}{N_{gen}(\Delta p_T, \Delta y)}. \quad (1)$$

347 For combined $\Sigma^0 + \bar{\Sigma}^0$ data the combined efficiency was calculated and presented on the left plot in
348 Fig. 14. Note the statistical uncertainties of efficiency correction factor were included in the statisti-
349 cal uncertainties of the reconstructed Σ^0 transverse momentum spectrum. The amount of reconstructed
350 Σ^0 is determined by the probability of photon conversion in central tracking system is ~ 0.08 and its
351 reconstruction efficiency which is about 0.67 [15, 16]. The branching of $\Lambda \rightarrow p + \pi^-$ and $\bar{\Lambda} \rightarrow \bar{p} + \pi^+$
352 (63.5 %) was included in the presented correction factor. The MC sample was used for the closure test.
353 The simulated and reconstructed, after the subtraction of second-order polynomial fitted background,
354 Σ^0 yields and its ratio, is presented on the right plot of Fig. 14. The fit of the ratio is consistent with unity,
355 therefore no more corrections have been applied.

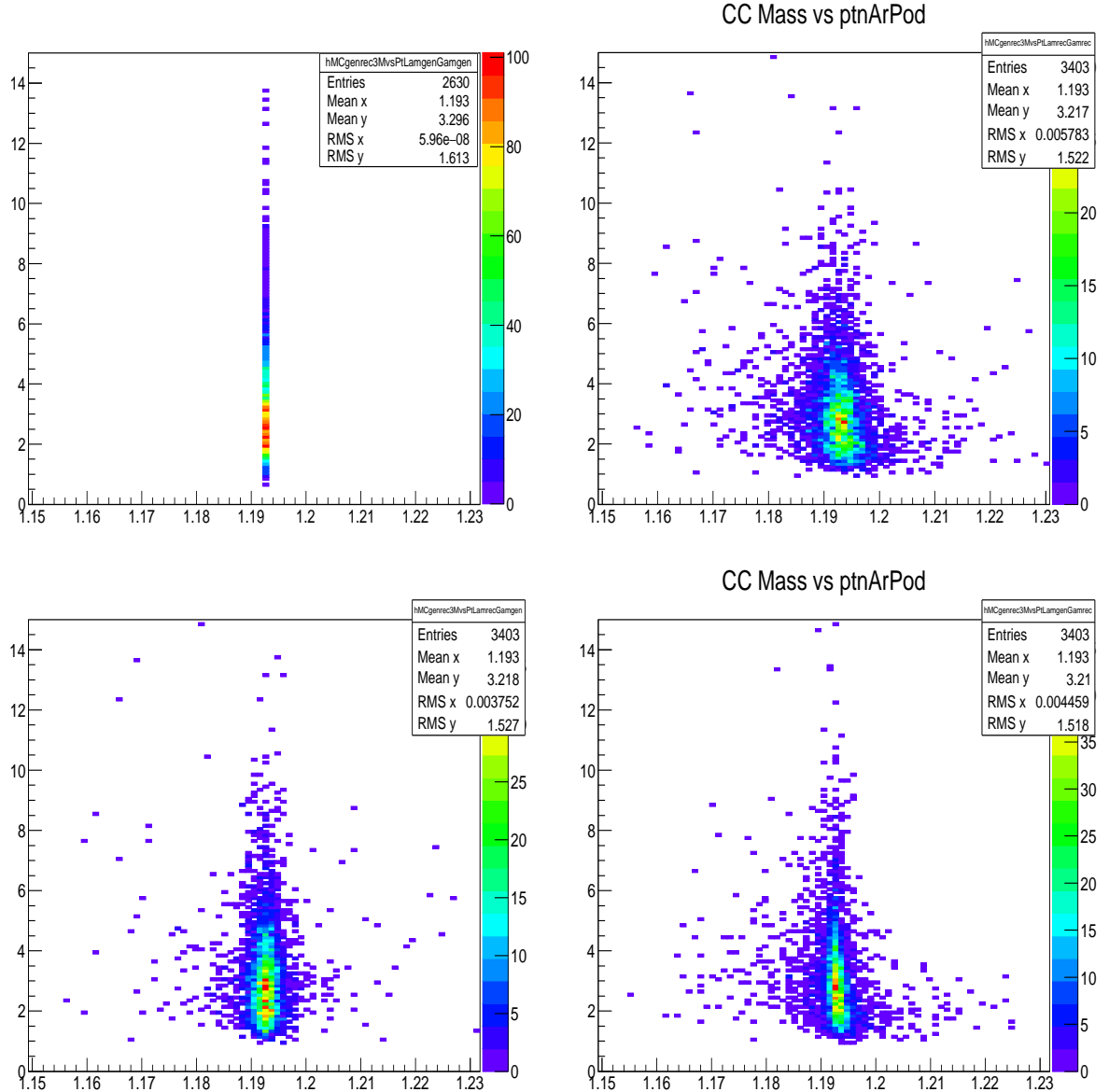


Fig. 13: Mass vs p_T evolution of simulated “true” Σ^0 , with different combination of four-momentum of generated (gen) and reconstructed (rec) photon and Λ . Top plots, left - $\Lambda^{gen}\gamma^{gen}$, right - $\Lambda^{rec}\gamma^{rec}$, bottom plots, left - $\Lambda^{rec}\gamma^{gen}$, right - $\Lambda^{gen}\gamma^{rec}$.

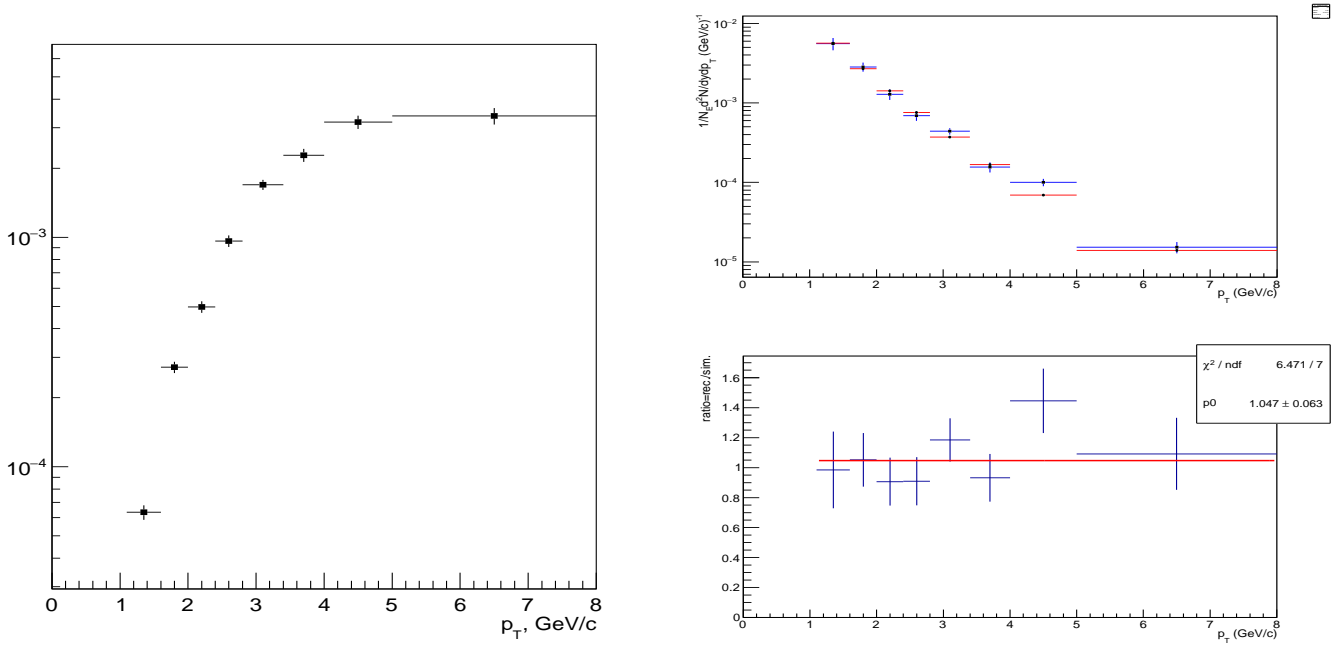


Fig. 14: The product of acceptance, efficiency and branching ratio of $\Sigma^0 \rightarrow \Lambda + \gamma$ and $\bar{\Sigma}^0 \rightarrow \bar{\Lambda} + \gamma$ decays as function of p_T at $|y| < 0.5$ is on the left plot. The reconstructed (blue lines and squares) and simulated (red lines and circles) $(\Sigma^0 + \bar{\Sigma}^0)/2$ yields are on the left-top plot, its ratio with constant fit is presented on the left-bottom plot.

356 5 Σ^0 p_T -spectrum from pass-2 and pass-4 productions

357 As there is no world data with which the results on Σ^0 p_T -spectrum can be compared, the essential point is
 358 to cross-check the agreement between the results obtained from two available, but different productions
 359 of ALICE 2010 pp data at $\sqrt{s} = 7$ TeV. For that purpose the analysis of the data from both productions
 360 was performed with the same codes and readout of the same runs with good quality. As the Monte Carlo
 361 production for pass-2 data corresponds only to 2010 d+e subsets, the runs from pass-4 data have been
 362 used also from the 2010 d+e periods of data taking. Lists of those runs are presented in the appendix
 363 11.2.

364 The inelastic p_T -spectrum represents the number of produced particles of a given type in the desired
 365 interval of rapidity y and p_T phase-space normalized on the number of inelastic collisions. The spectrum
 366 is calculated as:

$$\frac{1}{N_E} \times \frac{d^2N}{dy dp_T} = \frac{1}{N_{E,\text{PhysSel}}} \times \frac{N_{\text{raw}}}{dp_T dy} \frac{1}{\varepsilon}, \quad (2)$$

367 where N_E represents the number inelastic collisions, the $\frac{d^2N}{dy dp_T}$ is the yield per range of rapidity y , per
 368 unit in p_T . On the right hand side $N_{E,\text{PhysSel}}$ is the number of events counted by the PhysSelection trigger
 369 which is equal to the number of minimum bias triggers. N_{raw} is the raw extracted number of particle
 370 in the rapidity and p_T bin of width $|\Delta y| = 0.5$ and Δp_T , respectively, ε is the reconstruction efficiency
 371 estimated from Monte Carlo simulations which is different for the pass-2 and pass-4 productions, see the
 372 left plot in Fig. 15.

373 The Σ^0 normalized yields from pass-2 and pass-4 data are presented in the right plot of Fig. 15 and are
 374 in agreement with each other within statistical uncertainty. For completeness, the agreement between
 375 the total sample of Σ^0 yields from pass-4 data and the restricted one, used for comparison with pass-2
 376 production, is shown in Fig. 16.

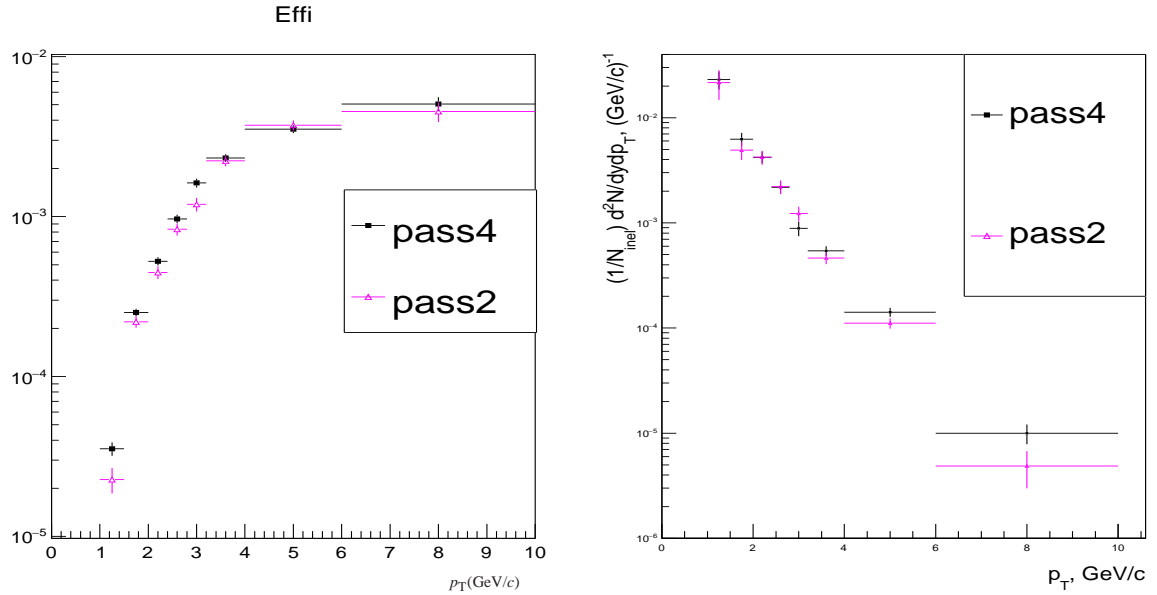


Fig. 15: Acceptance and efficiency of reconstructed Σ^0 (left plot), and Σ^0 normalized yields (left plot) from pass-4 and pass-2 from the same good runs.

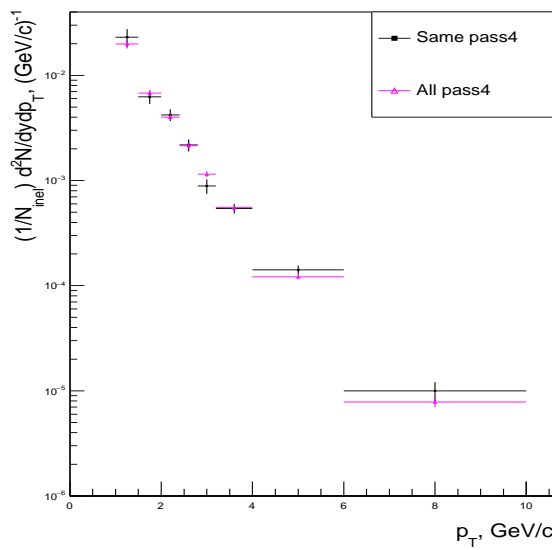


Fig. 16: Σ^0 normalized yields from pass-4 production from the selected for comparison same with pass-2 good runs all pass-4 good runs.

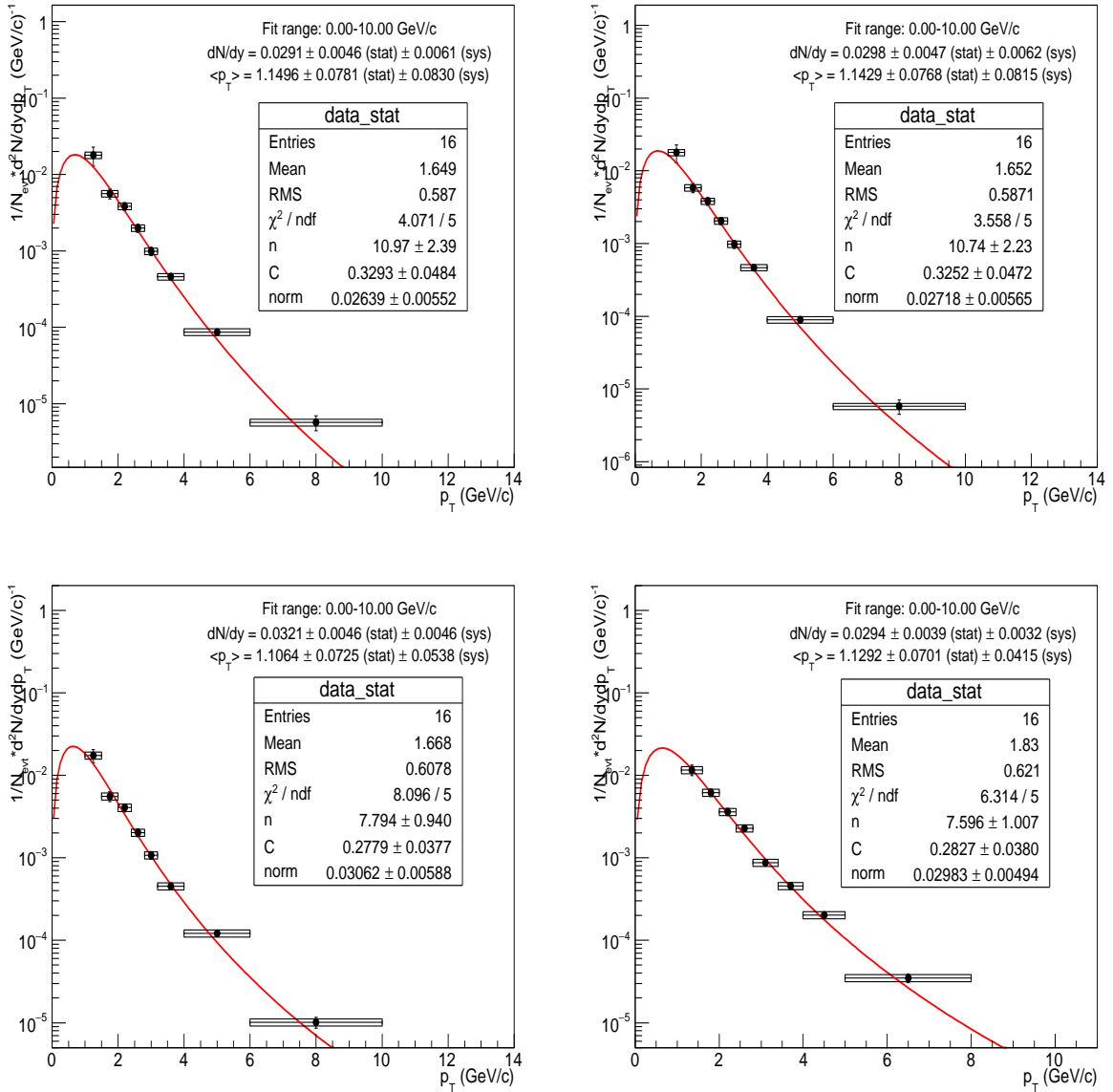


Fig. 17: Lévy-Tsallis fits of same (left plots) and all runs (right) from pass-2 (top) and pass-4 (bottom) data.

377 Further cross-check of pass-2 and pass-4 data was done with the Lévy-Tsallis fits of the spectra, shown
378 in Fig. 17. For consistency in the fit results, the relative systematic uncertainty was estimated to be equal
379 0.1 in all p_T -bins of pass-2 and pass-4 data. A third-order polynomial background and a Gauss fit of the
380 signal was used for the extraction of the yields. The fit results agree within one total error. Note that
381 fit results from the pass-4 total sample have smaller statistical uncertainty due to the significantly larger
382 sample of all runs than the sample of the same runs. The presentation of pass-2 vs pass-4 Σ^0 analysis was
383 done in the RSN meeting on 24th of August 2016.

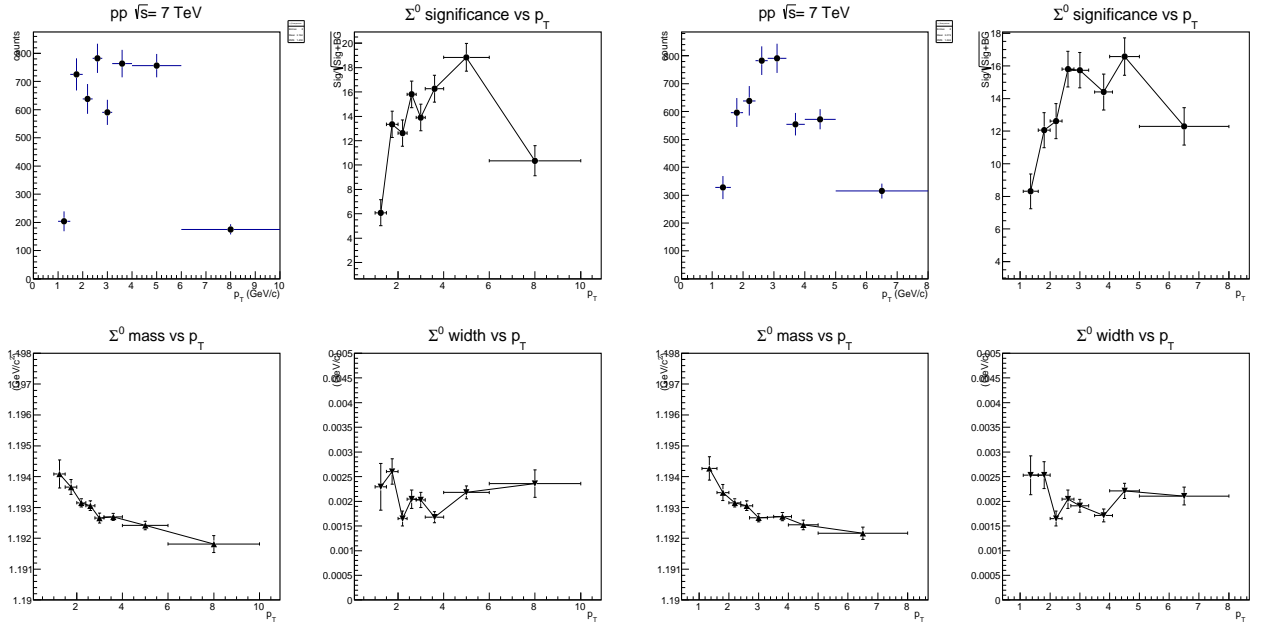


Fig. 18: Raw yields and mass fit results at different p_T -binning: left plot with previous one ($1.0 \div 1.5 \div 2.0 \div 2.4 \div 2.8 \div 3.2 \div 4.0 \div 6.0 \div 10.0 \text{ GeV}/c$), right plot with the current one ($1.1 \div 1.6 \div 2.0 \div 2.4 \div 2.8 \div 3.4 \div 4.0 \div 5.0 \div 8.0 \text{ GeV}/c$).

384 6 Optimization of p_T bins

385 The Σ^0 yields with the old p_T -bins which were used in the analysis notes [13, 14], are presented in the left
386 plots of Fig. 18 with the significance if the yield, mean value of the mass and width of mass distribution.
387 For the old p_T -binning: $1.0 \div 1.5 \div 2.0 \div 2.4 \div 2.8 \div 3.2 \div 4.0 \div 6.0 \div 10.0 \text{ GeV}/c$, the yield in the lowest
388 and highest p_T -bins are marginal and the results of the fits with different functions are unstable. Even
389 more, only a few Σ^0 entries were observed near p_T -edges, i.e. above $1 \text{ GeV}/c$ and below $10 \text{ GeV}/c$ in
390 data and reconstructed Σ^0 from simulations.

391 To prove the stability of fit results several variations of p_T -binnings have been tested, see Tab. 5 in
392 appendix 11.3. The relative systematic uncertainties of 0.1 in each p_T -bin were estimated and used at the
393 fits using the Lévy-Tsallis function from Eq.4. The new p_T boundaries were chosen from the comparison
394 of the fit results from Tab. 5: $1.1 \div 1.6 \div 2.0 \div 2.4 \div 2.8 \div 3.4 \div 4.0 \div 5.0 \div 8.0 \text{ GeV}/c$. The results of
395 the Lévy-Tsallis fits with the old and new p_T -binnings are presented in Fig. 19. A practically negligible
396 increase of statistical uncertainty is observed with the new binning which was chosen for the extraction
397 of systematic uncertainties and the final presentation of the spectrum. For this estimation, a systematic
398 uncertainty of 10 % was accounted in each p_T bin.

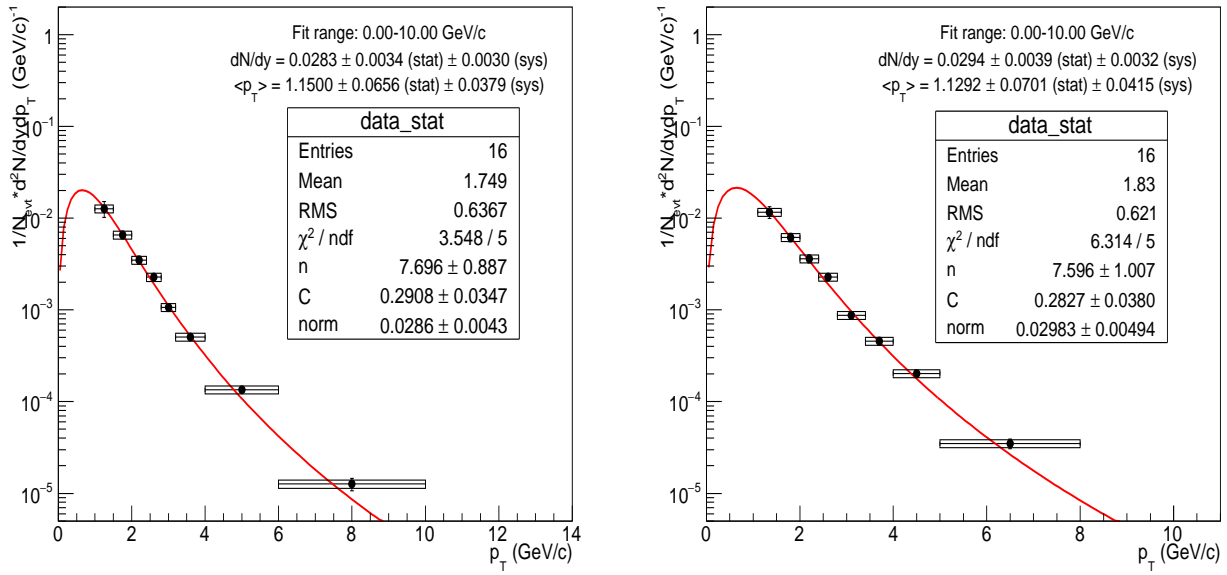


Fig. 19: Lévy-Tsallis fit results at different p_T -binning $1.0 \div 1.5 \div 2.0 \div 2.4 \div 2.8 \div 3.2 \div 4.0 \div 6.0 \div 10.0$ GeV/c and $1.1 \div 1.6 \div 2.0 \div 2.4 \div 2.8 \div 3.4 \div 4.0 \div 5.0 \div 8.0$ GeV/c.

399 7 Systematic uncertainties

400 As the decay products of Σ^0 are a Λ and a photon, the systematic uncertainties have been studied for Λ and
 401 photon selection independently. In addition, the uncertainty of Σ^0 signal extraction has been estimated.
 402 The variation of cuts used for Λ and photon selection in the Σ^0 invariant mass region was done in data and
 403 Monte Carlo samples and the new correction factor and normalized yield was obtained. The variation
 404 of the yield was calculated relative to the yields from the base set of cuts. Due to the limited statistics,
 405 the cuts were specifically chosen to keep the amount of the events inside 80 % of the base sample. From
 406 the application of five cuts, the mean value and the standard deviation was calculated. It was compared
 407 with the statistical uncertainty in the same p_T -bin and a Barlow check was performed. If the deviations
 408 from the variation of certain cuts are large and have a non-Gaussian shape, the standard deviation was
 409 accounted as a source of systematic uncertainty.
 410 Note, that low statistics of the raw yield of $\Sigma^0 + \bar{\Sigma}^0$ limits the possibility of the extraction of many
 411 components of the systematic uncertainties, as was done for Λ and photon analyses, see, for example
 412 Refs. [1, 23, 24].

413 7.1 Systematic uncertainty of Λ detection

414 Variations of the following TTreeee variables was performed to determine the systematic uncertainties of
 415 the Σ^0 yields due to cuts on Λ selection:

- 416 - LambdaCosPointingAngle
- 417 - LambdaMass
- 418 - LambdaVORadius
- 419 - LambdaKOsDiff
- 420 - LambdaDCADaughters
- 421 - LambdaDCAToPVPos
- 422 - LambdaDCAToPVNeg
- 423 - LambdacTau
- 424 - LambdaSigmasProton

425 - LambdaRatioRows.

426

427 One example of the variation of reconstructed DCA to primary vertex (PV) of positive track is presented
428 below, see Fig. 20. The variations of another variables is presented in appendix 11.4.

429 The cuts for $\Lambda + \bar{\Lambda}$ selection were varied within the limits presented in the top-left plot of Fig. 20 in data
430 and Monte Carlo samples. These variations result in variations of the Σ^0 spectra, see the top-right plot
431 of Fig. 20. From this set of variations the its mean value and standard deviation are presented in the
432 bottom-left plot of Fig. 20. The distributions of the Barlow parameter are presented in the top part of the
433 bottom-right plot. The fraction of entries within $\pm 3\sigma$, $\pm 2\sigma$ and $\pm 1\sigma$ are presented as bold blue lines
434 extending to 3, 2 and 1, respectively. The corresponding fractions for an ical Gaussian distribution with
435 mean zero and standard deviation one are indicated by the red lines extending to 3, 2 and 1. Due to the
436 good agreement with the Gaussian distribution, it is concluded that DCA to PV of Λ is not a significant
437 source of systematic uncertainties.

438 The standard deviations and mean values of five sources of systematic uncertainties passed the Bar-
439 low check were added quadratically and are presented in the left plot of Fig. 21. The sources are the
440 following: LambdaCosPointingAngle, LambdaK0sDiff, LambdaDCADaughters, V0Radius, Lambda-
441 RatioRows. Note, that the systematic uncertainty of Λ detection becomes larger than about 2% if all
442 sources are added quadratically.

443 Detailed systematic studies with around ~ 100 times larger statistics have been done for the extraction of
444 Λ and $\bar{\Lambda}$ transverse momentum spectra, see Refs. [1, 2]. The plots representing p_T dependent systematic
445 uncertainties of Λ and $\bar{\Lambda}$ from Ref. [1, 2] are presented in Fig. 21. One can see good agreement between
446 the systematic uncertainty of Λ detection extracted from the selected sources that passed the Barlow
447 check from the Σ^0 analysis and the total systematic uncertainty of the detected Λ ($\bar{\Lambda}$) from the recent
448 dedicated Λ analysis [2].

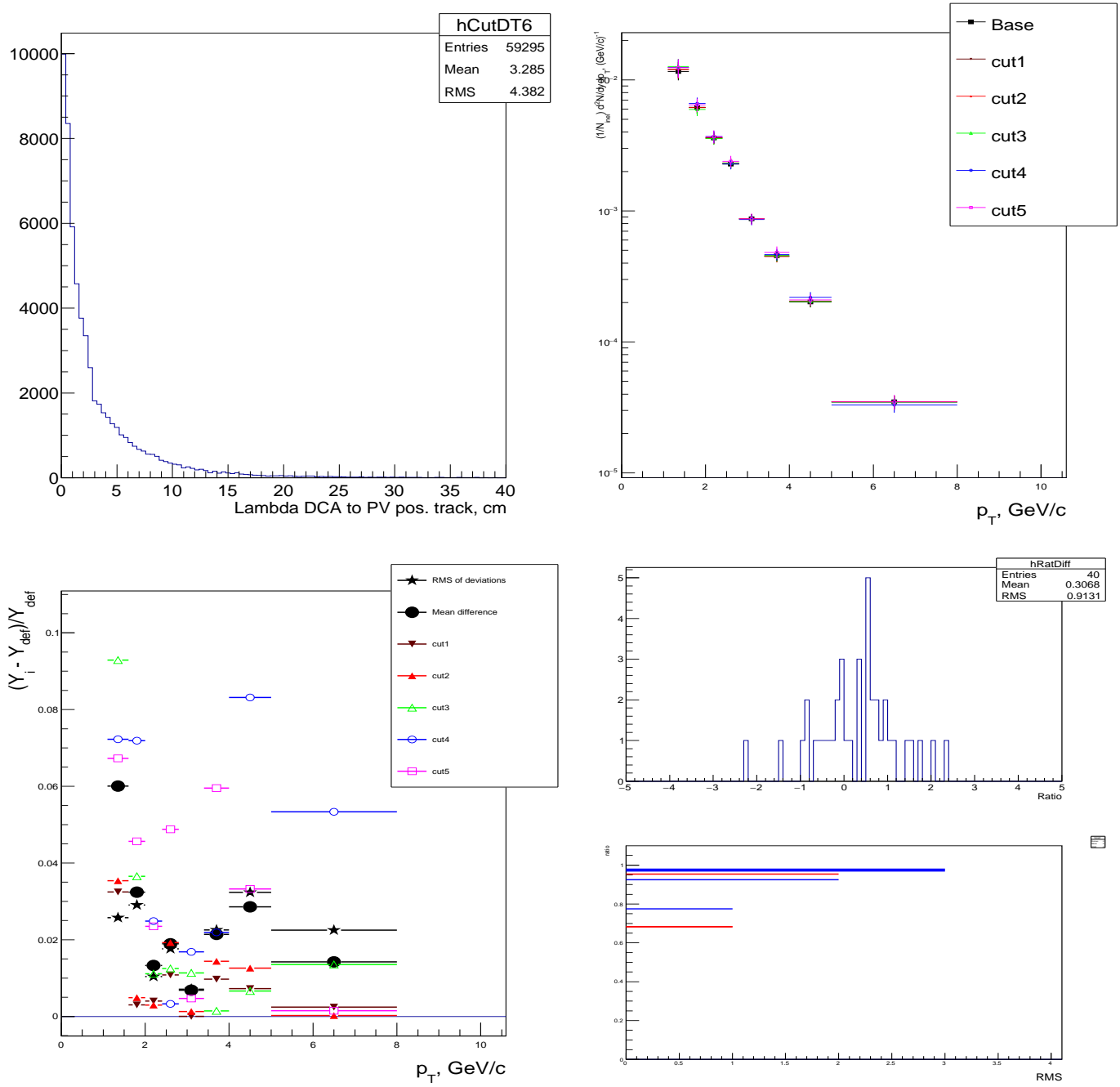


Fig. 20: Example of the variations of the cut on DCA to PV for the positive track of the Λ decay. The distribution of the DCA to PV for the positive track is in the top-left plot. The variations from the base value DCA < 40.0 cm are the following: 10.0, 8.0, 6.0, 4.0, 2.0 cm. The $\Sigma^0 p_T$ spectra from these different cuts are in the top-right plot. The relative variations, their standard deviation (black stars) and mean deviations (black circles) are in the bottom-left plot. The distributions for the Barlow check are in the bottom-right plot, see its explanation in the text.

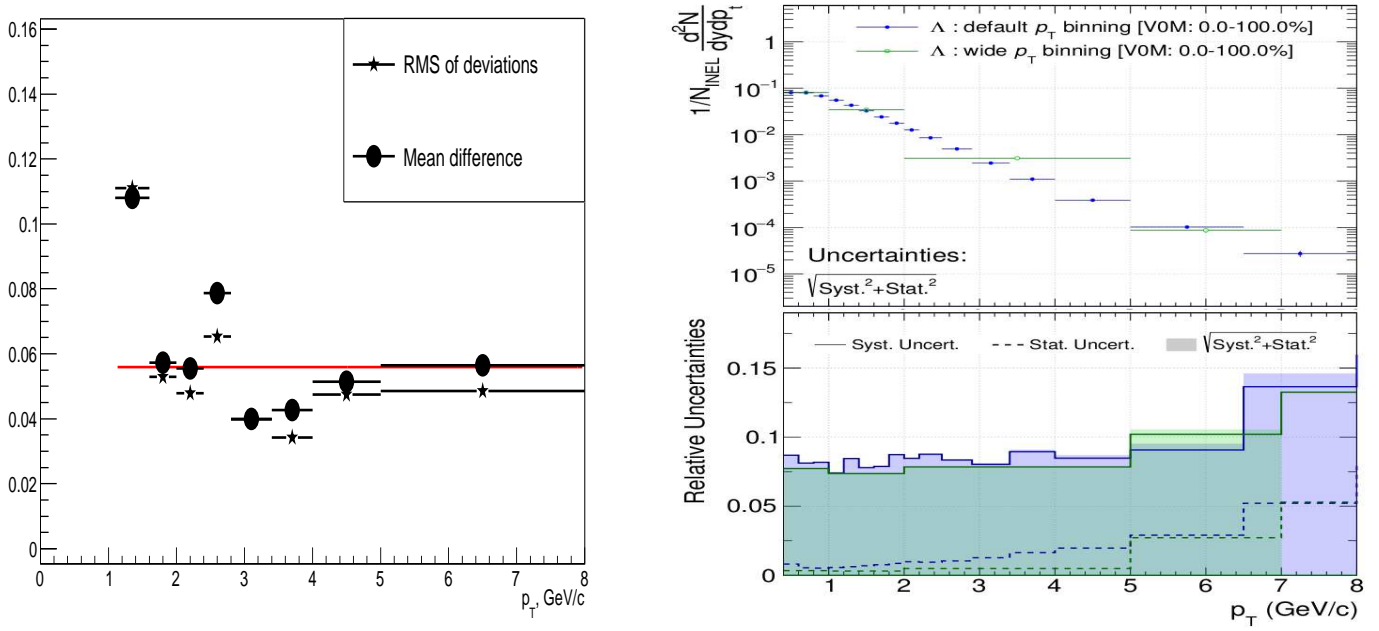


Fig. 21: Left plot: systematic uncertainty of Λ detection extracted from the variations of cuts which passed Barlow check, standard deviations are presented as black circles. The red line represents the mean standard deviation averaged over p_T bins. Right plot: from the systematic uncertainty of the separate Λ analysis in Ref. [2].

449 7.2 Systematic uncertainty of γ detection

450 Cuts on the following parameters were varied to calculate the systematic uncertainty of the Σ^0 yields
451 due to γ selection:

- 452 - $\cos(PA)$
- 453 - DCA daughters
- 454 - DCA to PV
- 455 - χ^2
- 456 - Radius = $\sqrt{x_{V0}^2 + y_{V0}^2}$
- 457 - $N \sigma e^+$
- 458 - $N \sigma e^-$
- 459 - $N \sigma \pi^+$
- 460 - $N \sigma \pi^-$
- 461 - ratio TPC rows
- 462 - $p_T e^+$
- 463 - $p_T e^-$.

464
465 As an example, the variation of the cut on to the reconstructed p_T of the conversion electron is presented
466 below, see Fig. 22. The variations of the other variables are presented in appendix 11.5. The variations
467 with significant deviation from an ideal Gaussian distribution in the Barlow check are accounted as
468 independent sources of systematic uncertainty and added in quadrature.

469 The cuts for γ selection were varied within the limits presented in the top-left plot of Fig. 22 in data
470 and Monte Carlo samples. These variations result in the variation of Σ^0 spectra, see the top-right plot of
471 Fig. 22. From the set of variations the standard deviation and its mean value are presented in the bottom-
472 left plot of Fig. 22. The distributions of Barlow parameter is presented on top part of bottom-right plot.
473 As before, the fraction of the distribution within $\pm 3\sigma$, $\pm 2\sigma$, and $\pm 1\sigma$ are indicated by blue lines, while

474 the expected values assuming an ideal distribution are given by red lines. Due to the good agreement
 475 with the Gaussian distribution, it is concluded that variation of cuts on p_T of conversion electron of Λ is
 476 not a significant source of systematic uncertainties.

477 The standard deviations and mean values of five sources of systematic uncertainties that passed the
 478 Barlow check were added quadratically and are presented in the left plot of Fig. 23. The sources are
 479 following: χ^2 , $N \sigma e^+$, $N \sigma e^-$, $N \sigma \pi^+$, $N \sigma \pi^-$. Note, that the systematic uncertainty of γ detection
 480 becomes larger than about 2% if all sources are added quadratically.

481 7.3 Systematic uncertainty of $\Sigma^0 + \bar{\Sigma}^0$ yield extraction

482 The following approach was used for the estimation of systematic uncertainties of Σ^0 yield extraction.
 483 The base setting with third-order polynomial background and a Gauss fit of the signal is shown on the
 484 left plot of Fig. 24.

485 Five different analysis parameters were varied and considered simultaneously in calculating the system-
 486 atic uncertainty. The corresponding p_T spectra are shown in the right plot of Figure 24. First, a mixed
 487 event background was used instead of a third-order polynomial background. Second, a second-order
 488 polynomial was used. Third, the bin counting method was used to find the integral of the invariant
 489 mass peak. Fourth, both a mixed-event background and the bin-counting method were used. Fifth, a
 490 second-order polynomial background and the bin-counting method were used. Simultaneous variations
 491 of five main parameters was used instead of one, corresponding p_T -spectra are shown on the right plot of
 492 Fig. 24. First, the variation of background subtraction method: third order polynomial background ver-
 493 sus mixed events background and Gaussian fit of signal. The second variation was done for the second
 494 order polynomial background. The third variation was done for the calculation of Σ^0 yield: bin-counting
 495 approach versus integral of Gauss fit of invariant mass peak, see Fig. 25. The fourth variation was done
 496 with the mixed background and bin-counting method. And the fifth variation for the second order poly-
 497 nomial background and bin-counting method. ;;;;

498

499 The resulting p_T -spectra are presented in the left plot of Fig. 26. On the right plot are the relative
 500 deviations of each variation relative to the base setting with a second-order polynomial background and
 501 a Gauss fit of the signal. The mean values of those deviations are presented in the right plot of Fig. 26
 502 in black circles. The values of calculated standard deviations are depicted as black stars in each bin of
 503 p_T . In the right plot of Fig. 26 the results of the Barlow check are presented, indicating the significant
 504 deviation from the Gaussian distribution. The standard deviations are treated as a conservative estimate
 505 of the systematic uncertainties of Σ^0 yield extraction.

506 7.4 Total systematic uncertainties

507 The Σ^0 systematic uncertainty is determined by four general sources:

$$\sigma_{\text{syst}} = \sqrt{\sigma_\gamma^2 + \sigma_\Lambda^2 + \sigma_{\text{Yield}}^2 + \sigma_{\text{mat}}^2}, \quad (3)$$

508 where the fractional systematic uncertainty due to the limited knowledge of material budget for the
 509 conversion photon $\sigma_{\text{mat}} = 0.045$, see Refs. [16, 19, 23]. Its value in p_T bins is: 0.190, 0.108, 0.095,
 510 0.109, 0.079, 0.092, 0.107, 0.149; see also Fig. 27. The value of the total systematic uncertainty averaged
 511 over all p_T -bins is 0.116. Note, that the contributions of the uncertainties passed Barlow check have
 512 been excluded. The most conservative estimate, including all sources of Λ and γ systematic uncertainties
 513 (including those that are insignificant according to the Barlow check) are 0.225, 0.130, 0.126, 0.136,
 514 0.088, 0.107, 0.127, 0.156.

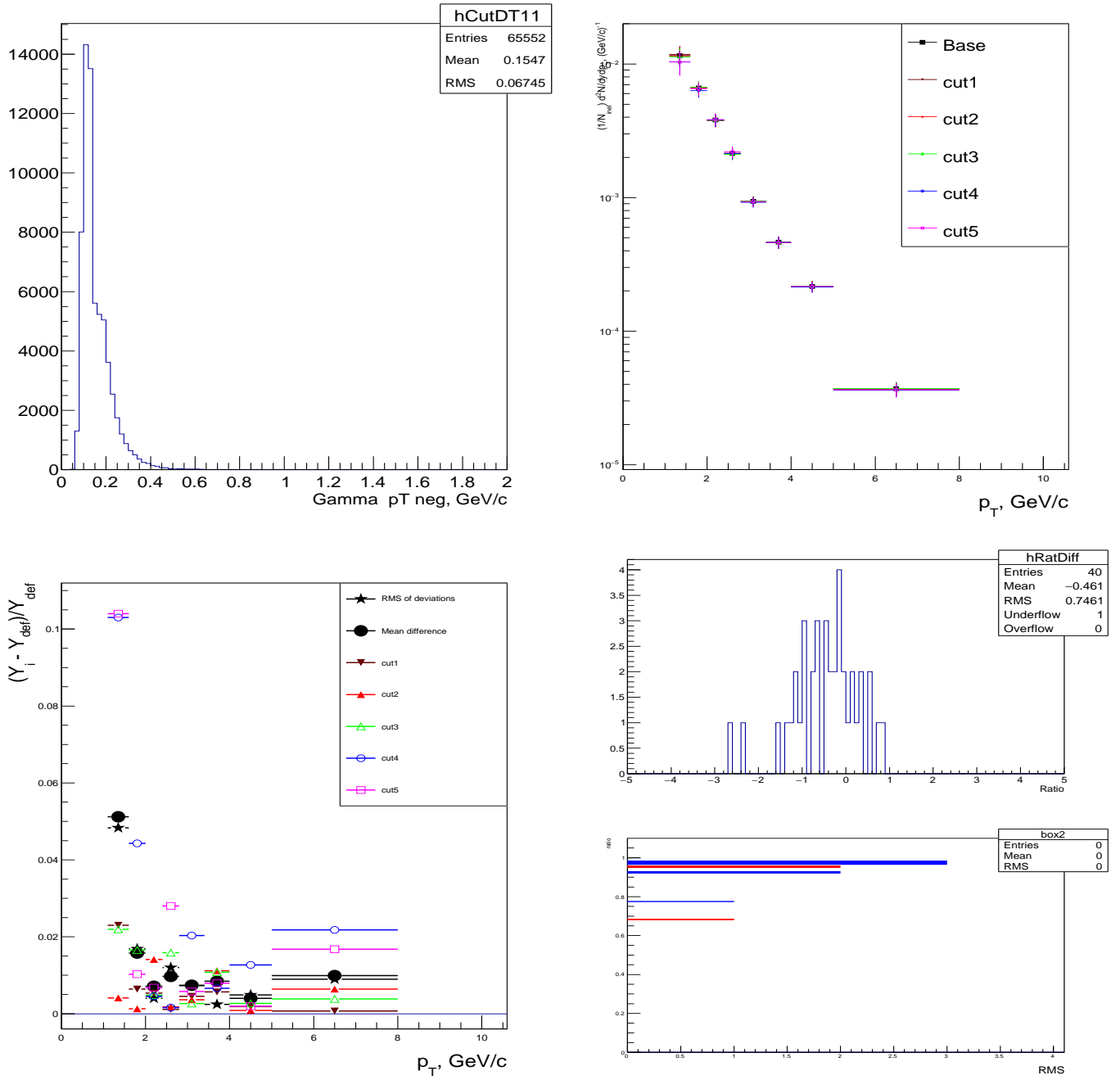


Fig. 22: Example of the variations of the cut on p_T of the conversion electron. The p_T distribution of the conversion electron is in the top-left plot. The base value is a minimum p_T of 0.5 GeV/c, the variations of minimum p_T are: 0.75 ; 0.80 ; 0.85; 0.90 ; 0.95 GeV/c. The Σ^0 p_T spectra from different cuts are on the top-right plot. The relative variation, its standard (black stars) and mean deviation (black circles) are in the bottom-left plot. The distributions for the Barlow check are in the bottom-right plot, see its explanation in the text.

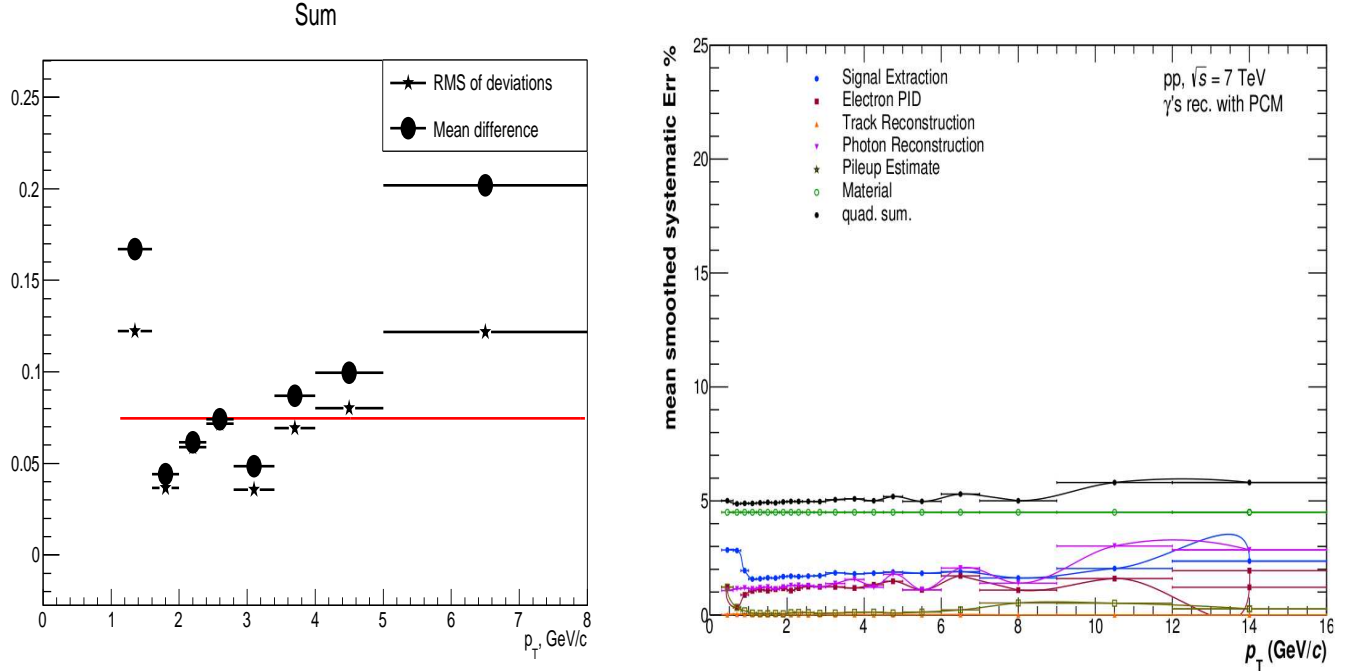


Fig. 23: Left plot: systematic uncertainty of γ detection extracted from the variations of cuts which passed the Barlow check. Standard deviations are black stars, and mean deviation are black circles. The red line represents the mean value of standard deviation averaged over p_T bins. The right plot comes from the analysis of the PCM [15].

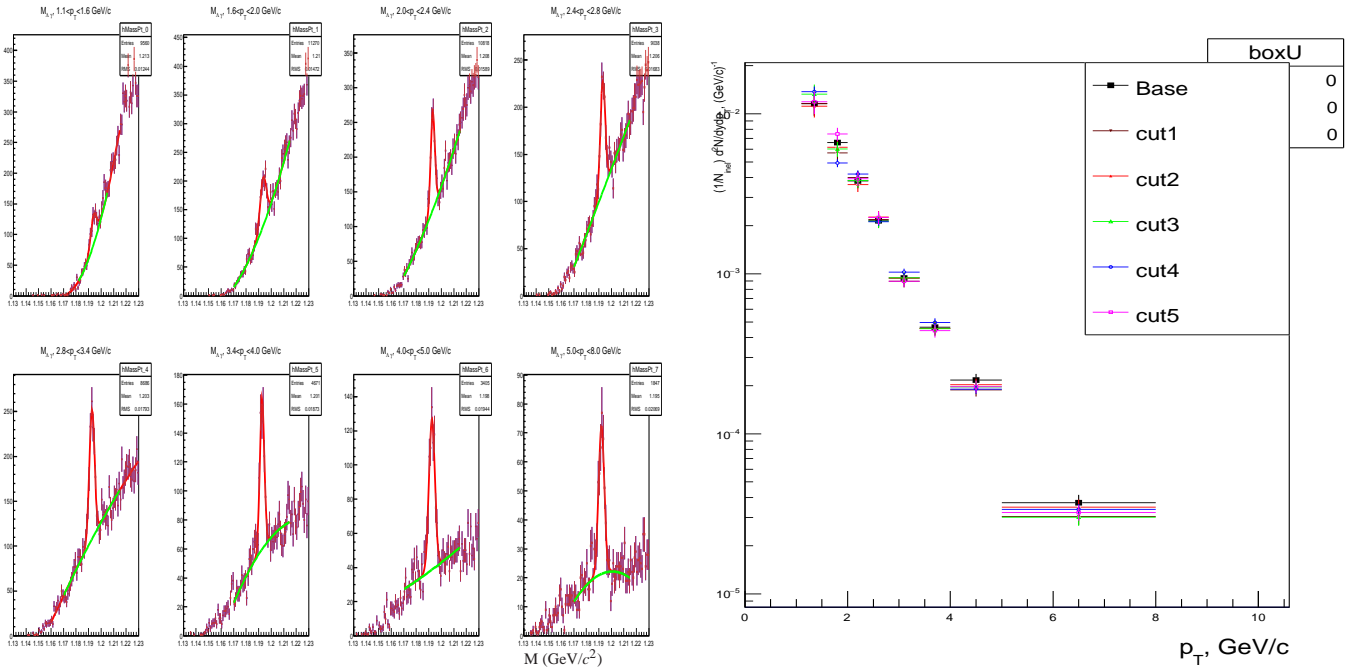


Fig. 24: Left plot. Σ^0 invariant mass distribution with third-order polynomial fit of background and Gaussian fits of the mass-peak. Right plot. p_T spectra of Σ^0 shown with the variations of background treatment and signal extraction. Base - third-order polynomial fit of background and Gaussian fit of the mass-peak. Cut 1 - mixed background and Gaussian fit of the mass-peak; cut 2 - third-order polynomial fit of background and counting of subtracted signal ; cut 3 - mixed background normalized in another region and Gaussian fit of the mass-peak; cut 4 - mixed background and counting of subtracted signal; cut 5 - second order polynomial fit of background and counting of signal. The region of mass for counting of the signal is 1.192 ± 0.010 GeV/c^2 .

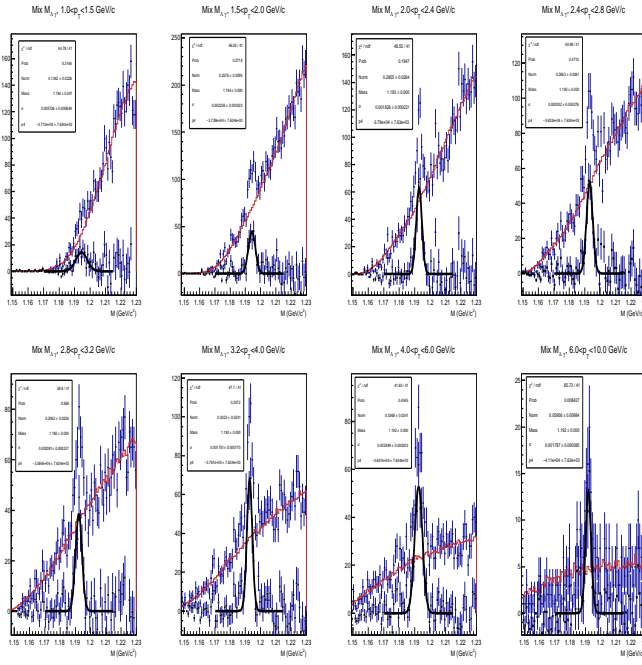


Fig. 25: Subtraction of the mixed background from pass-4 data. Note the significant statistical fluctuations of residual background.

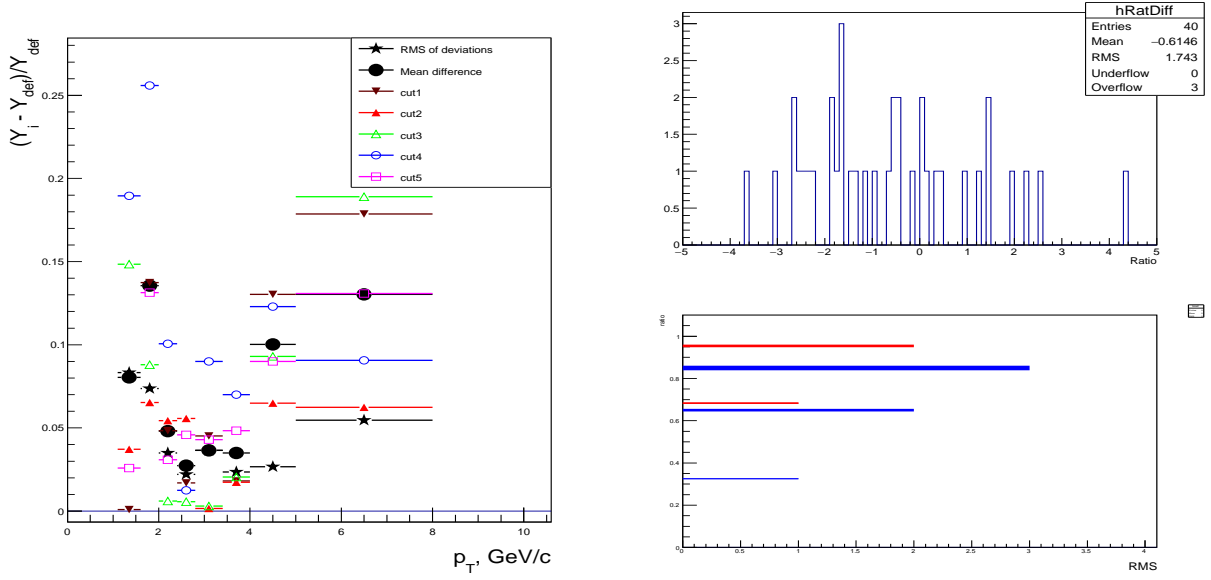


Fig. 26: The relative variations, their standard deviations (black stars) and mean deviations (black circles) are in the left plot, see Fig. 24 for the definitions of the cuts. The distributions for the Barlow check are in the bottom-right plot, see its explanation in the text.

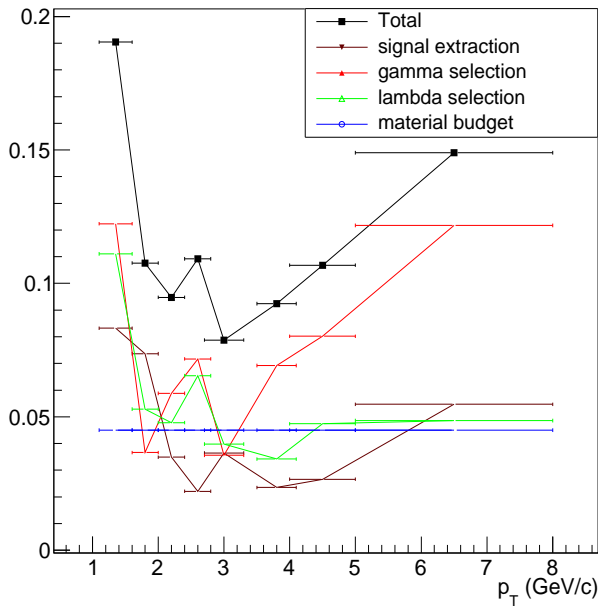


Fig. 27: Total systematic uncertainty and its components.

515 8 Fitted Σ^0 p_T spectrum

516 The transverse momentum spectra of both $(\Sigma^0 + \bar{\Sigma}^0)/2$ and Λ are compared to the Perugia-2011 tune of
517 the PYTHIA generator, see Fig. 28 left and right plots correspondingly. One can see that for the applied
518 generators the overall production cross sections are largely underestimated.

519 The spectra of Σ^0 and Λ are fitted with a Lévy-Tsallis function using YieldMean.C macro, see Ref. [26]:

$$\frac{1}{N_{inel}} \frac{d^2N}{dydp_T} = \frac{(n-1)(n-2)}{nC[nC + m_0(n-2)]} \frac{dN}{dy} p_T \left(1 + \frac{m_T - m_0}{nC}\right)^{-n}, \quad (4)$$

520 where $m_T = \sqrt{m_0^2 + p_T^2}$.

521 As a cross-check of the stability of the ratio, the Σ^0/Λ ratio was calculated with different approaches
522 for the systematic uncertainties. Lévy-Tsallis fit results taking into account all sources of system-
523 atic variations, are presented in the right plot of Fig. 30, and the conservative estimate of the ratio
524 $R^{conserv} = 0.382 \pm 0.113$. If we consider the mean value of the systematic uncertainties from the left
525 plot of Fig. 29 (0.116) as a constant systematic uncertainty in all bins of p_T , the results of Lévy-Tsallis fit
526 are presented in the left plot of Fig. 31. The corresponding estimate of the ratio $R^{const} = 0.373 \pm 0.071$.
527 Note that in the very much independent analysis of pass-2 production of 2010 pp data at $\sqrt{s} = 7$ TeV
528 [14], obtained using the same data, the ratio was equal to 0.346 ± 0.089 , what is in good agreement with
529 the current analysis.

530

531 The results of the fit with a Boltzmann-Gibbs Blast-Wave function [27] are presented in the right plot of
532 Fig. 31.

533 The uncertainty due to the variation of the fit function are included as an independent source of the
534 total uncertainty due to the extrapolation to the unmeasured region of p_T between 0 and 1.1 GeV/c. The
535 fraction of the fit-function in the unmeasured p_T -region between 0 and 1.1 GeV is equal 0.62 from Lévy-
536 Tsallis fit and 0.57 from Boltzmann-Gibbs Blast-Wave fit. The results of the fits with Boltzmann, p_T , m_T

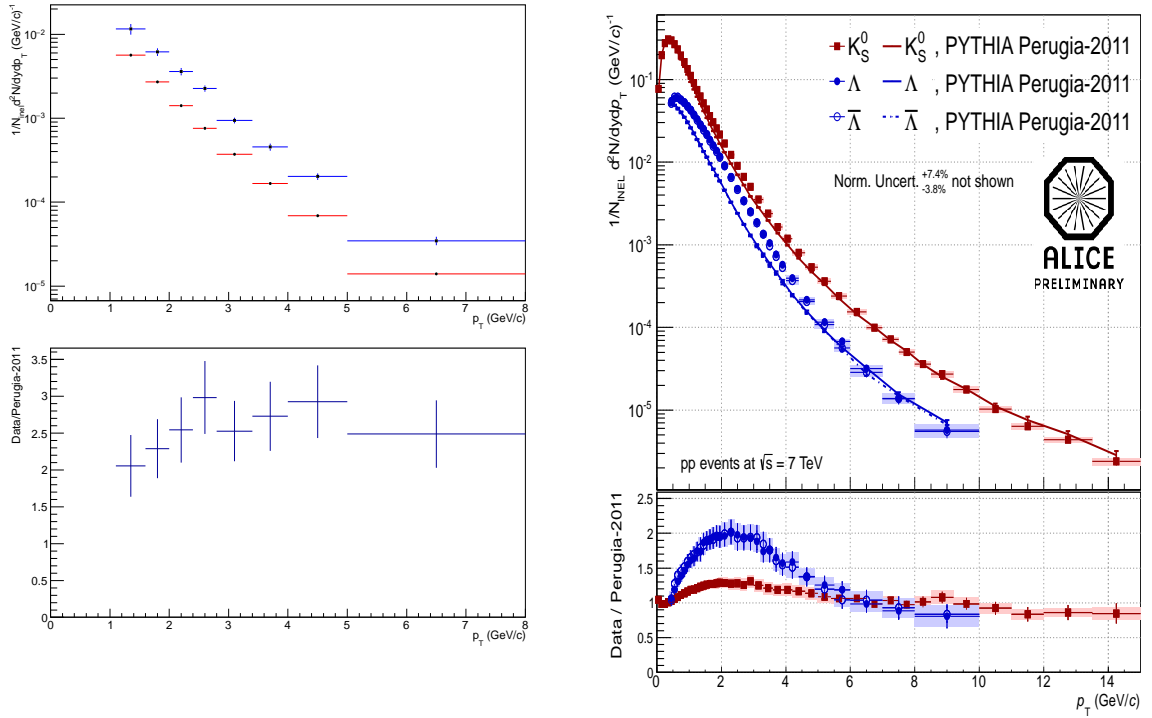


Fig. 28: The transverse momentum spectra of $(\Sigma^0 + \bar{\Sigma}^0)/2$ (left plot blue points) and Λ (right plot, blue points) in comparison with generators and data over MC ratios. The blue points in the left plot correspond to the PYTHIA Perugia-2011 generator. The open blue symbols on the right plot for Λ correspond to the PYTHIA Perugia-2011 generator. Spectra points are plotted at the center of the p_T interval. The lower panel shows the ratio data/MC. p_T -independent uncertainties are not shown. **ALICE Preliminary** approval is requested for the left plot, the layout of which will be improved.

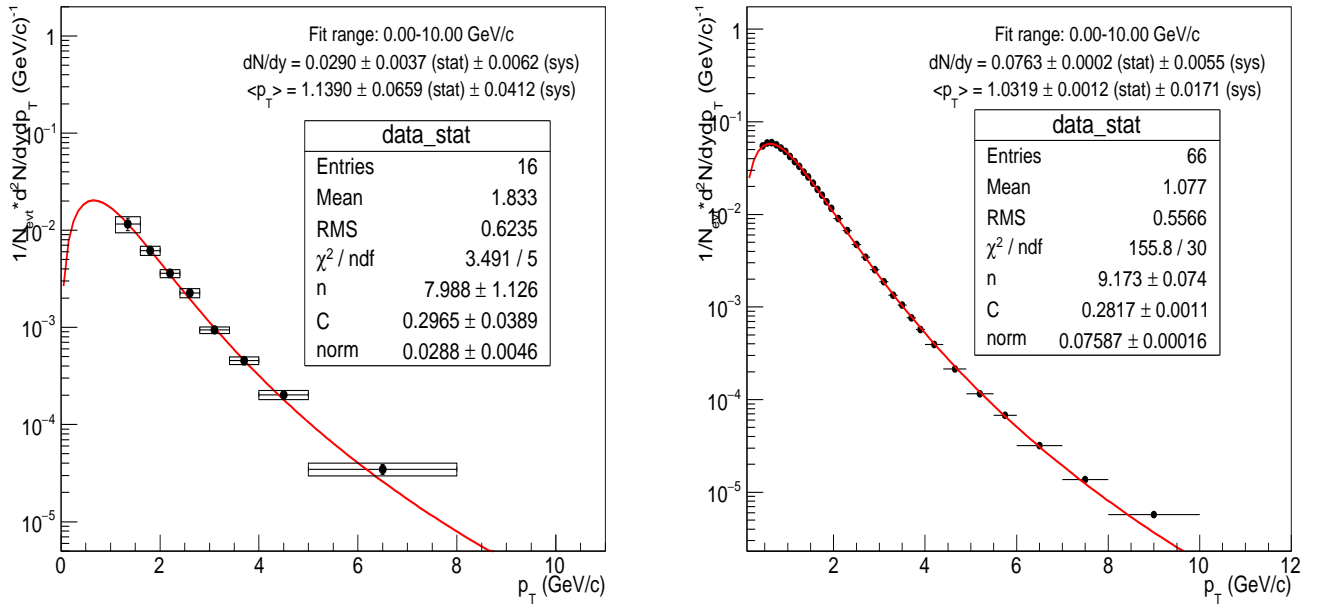


Fig. 29: The transverse momentum spectrum of $(\Sigma^0 + \bar{\Sigma}^0)/2$ and Λ fitted with a Lévy-Tsallis function. Note that Λ fit was performed with only statistical uncertainties, see Ref. [1] and Tab. 5 there for the details of the fit. **ALICE Preliminary** is asked for the left plot.

and Bose-Einstein fit functions [28, 29] have χ^2/NDF values much more than one, see plots in appendix 11.6. Therefore those fits do not contribute to the estimate of the total uncertainty. Note that estimation of systematic uncertainty from the extrapolation of the fit functions to the unmeasured p_T region is under development, and this analysis note will be updated.

The current fit results are presented in Fig. 29. and also in Tab. 1 in comparison with other hyperons, see Refs. [20]. The Σ^0 yield $dN^{\Sigma^0}/dy = 0.290 \pm 0.0072 (\pm 0.0037_{\text{stat}} \pm 0.0062_{\text{syst}})$ is shown on the left plot of Fig. 29 and **ALICE Preliminary** approval for this measurement is requested.

544

The value of the mean p_T of Σ^0 was taken from the result of the fit without the uncertainty on material budget, see left plot in Fig. 30: $\langle p_T \rangle = 1.1369 \pm 0.0810 (\pm 0.0658_{\text{stat}} \pm 0.0456_{\text{syst}})$, **ALICE Preliminary** approval for this measurement is requested.

548

One can see that the C , n and $\langle p_T \rangle$ parameters of Λ and Σ^0 agree within their statistical uncertainties. From the fits: $\frac{dN/dy^{\Sigma^0}}{dN/dy^{\Lambda}} = 0.380 \pm 0.098$, **ALICE Preliminary** approval for this result is requested. ALICE data point from pp collisions at $\sqrt{s} = 7$ TeV is presented with world data in Fig. 32. Note that data point from STAR experiment, presented on the left plot of Fig. 33 (Ref. [5]) was not published by STAR collaboration due to so large uncertainty of the ratio.

Particle	dN/dy	C (MeV)	n	$\langle p_T \rangle$ (GeV/c)
$\Lambda(1.1157)$	0.076 ± 0.0056	281.7 ± 1.1	9.17 ± 0.07	1.032 ± 0.018
$\Sigma(1.1926)^0$	0.0290 ± 0.0072	296.5 ± 38.9	7.988 ± 1.26	1.1369 ± 0.0801
$\Sigma(1385)^{\pm}$	$0.009 - 0.010 \pm 0.001$	$294 - 308 \pm 50$	$8.9 - 9.8 \pm 4$	1.175 ± 0.05

Table 1: Fit results for Λ , Σ^0 and other hyperons in pp collisions at $\sqrt{s} = 7$ TeV. Value of dN/dy for Λ is from the analysis note [1], values for $\Sigma(1385)^{\pm}$ are from Ref. [20].

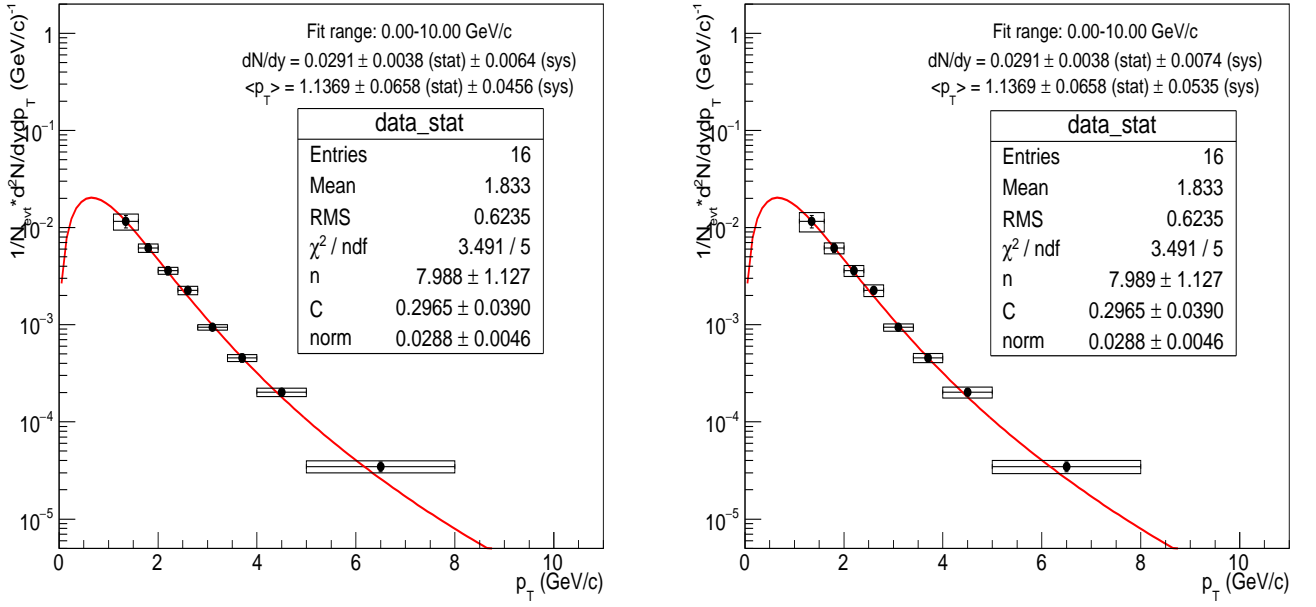


Fig. 30: The transverse momentum spectrum of $(\Sigma^0 + \bar{\Sigma^0})/2$ fitted with a Lévy-Tsallis function without systematic uncertainty of material budget(left plot) and with the most conservative estimate of the total systematic uncertainty including all sources of the variations of the applied cuts for Λ and γ selection (right).

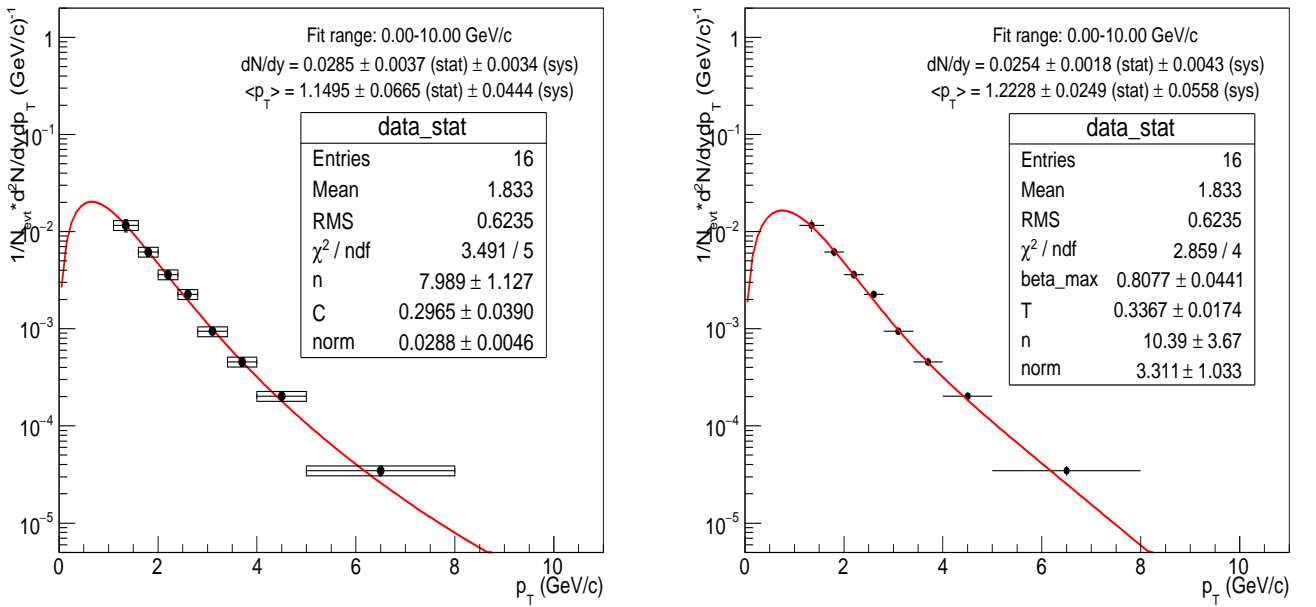


Fig. 31: The transverse momentum spectrum of $(\Sigma^0 + \bar{\Sigma^0})/2$ fitted with a Lévy-Tsallis function and systematic uncertainties averaged over p_T -bins with a value of 0.116 (left plot), fitted with a Boltzmann-Gibbs-Blast-Wave function (right plot).

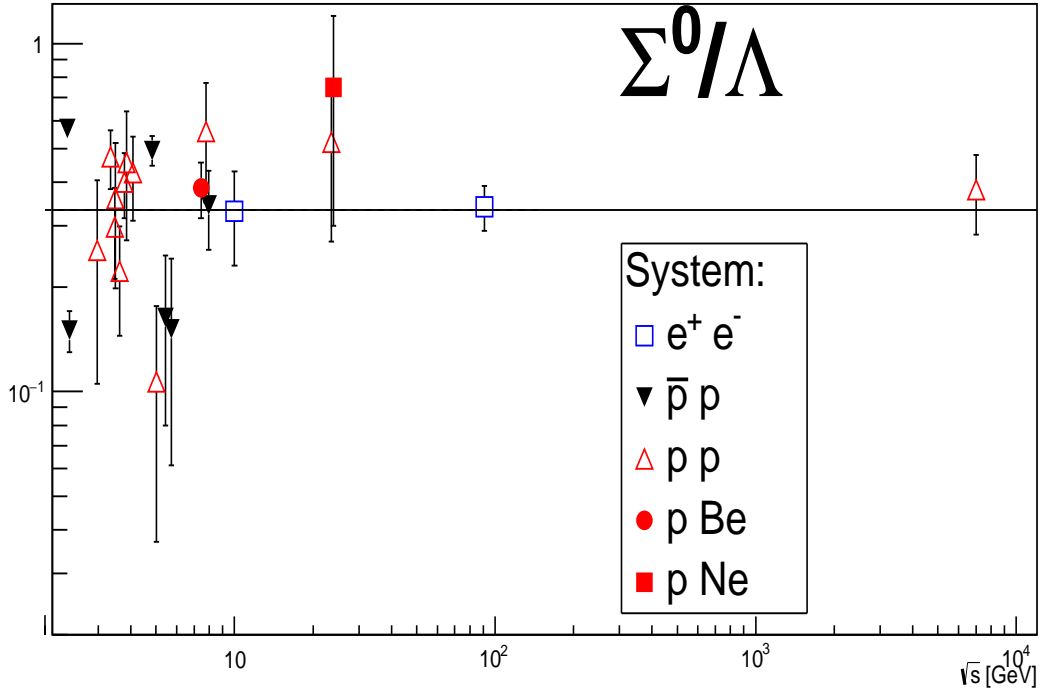


Fig. 32: Σ^0 to Λ cross section ratio in dependence of center of mass energy. Plot from Ref. [5] was modified with ALICE data at $\sqrt{s} = 7\,000$ GeV, **ALICE Preliminary** will be asked.

554 8.1 World data on $\frac{\Sigma^0}{\Lambda}$ cross section ratio

555 World data on the $\frac{\Sigma^0}{\Lambda}(\sqrt{s})$ ratio are quite poor, see Fig. 32. The reasons to extract $\frac{\Sigma^0}{\Lambda}$ ratio are perfectly
 556 presented by G.Van Buren in Ref. [5]: “These two hyperons share the same quark content, differing only
 557 in isospin and mass, separated by a mere $77\text{ MeV}/c^2$. Reconstructing the Σ^0 requires reconstructing the
 558 Λ , so comparing the ratio of yields of the two species provides a simple test of whether conditions are
 559 different for these two similarly-composed hyperons. Are they produced similarly? Are their final state
 560 interactions the same? Without measurements, these traits may only be assumed.”

561 While yields of Σ^0 have been measured in many different colliding systems at low and intermediate/
 562 moderate energies, only one measurement exists in high energy nuclear collisions. The STAR detector
 563 reconstructed the electromagnetic $\Sigma^0 \rightarrow \Lambda + \gamma$ decay via the weak decay of the $\Lambda \rightarrow p + \pi^-$ and γ
 564 conversions into e^+e^- pairs in the detector material [5]. There, the cross section ratio $\Sigma^0/\Lambda = 0.16^{+0.41}_{-0.09}$
 565 was measured in minimum bias 0.2 TeV d+Au collisions. Note that STAR data with so large errors were
 566 not published by the collaboration due to the limited statistics. High energy nuclear collisions are of
 567 particular interest due to the possibility of measuring isospin degeneracy factors from Σ^0 and Λ yields
 568 and of opening new channels of hyperon production via partonic degrees of freedom [30].

569 The most precise data are from L3 experiment in point 2 of LEP where both Σ^0 and Λ have been measured
 570 as a products of Z boson decay, see Fig. 32 and Ref. [4], where $\sigma^{\Sigma^0}/\sigma^\Lambda \approx 0.33 \pm 0.03$.

571 The relatively new and more precise COSY-TOF pp data from Ref. [6], see Fig. 33, have been published
 572 as the function of $\varepsilon = \sqrt{s} - (m_p + m_K + m_{\Lambda,\Sigma^0})$ and correspond to $\sqrt{s} \approx 1\text{ GeV}/c$. The cross section ratio
 573 $\frac{\Sigma^0}{\Lambda} \approx 0.45 \pm 0.05$.

574

575 The current status of the understanding of the calculations for the physics determined by the $\frac{\Sigma^0}{\Lambda}$ ratio is

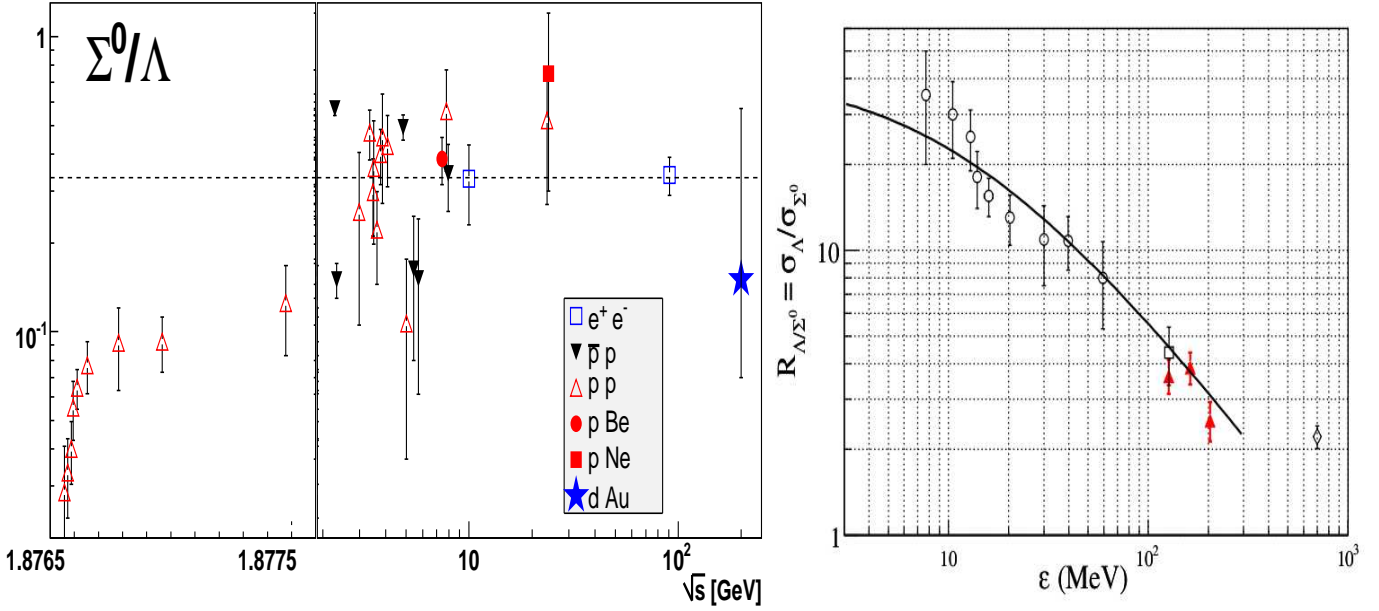


Fig. 33: Λ to Σ^0 to cross section ratio as a function of center of mass energy from Ref. [5], left plot, and Ref. [6], right plot.

well reproduced in the summary of low-energy data in Ref. [6]: “Thus, one of the key results of this paper is the proof that the reaction mechanisms for Σ^0 and Λ production differ decisively. With this differential data at hand theory is now challenged to advance a model which simultaneously describes the data presented.”

9 Summary

Σ^0 and $\bar{\Sigma}^0$ hyperon production is studied in pp collisions at $\sqrt{s} = 7$ TeV from 2010 pp data. The mass position and width of its invariant mass distribution are extracted as a function of p_T between 1.1 and 8 GeV/c. Good agreement with the Σ^0 PDG value of mass is observed. The width of the mass distributions is in agreement with the results of Monte Carlo simulations.

The main preliminary result is the cross section ratio $\frac{\Sigma^0}{\Lambda} = 0.380 \pm 0.098$ which was measured from the Lévy-Tsallis fits of Σ^0 and Λ spectra. This result was compared with COSY-TOF pp data at $\sqrt{s} \approx 1$ GeV: $\frac{\Sigma^0}{\Lambda} \approx 0.45 \pm 0.05$, see Ref. [6] and Fig.33. The L3 experiment at LEP reported on e^+e^- data at $\sqrt{s} \approx 100$ GeV, where both Σ^0 and Λ were detected from Z boson decays: $\frac{\Sigma^0}{\Lambda} = 0.33 \pm 0.03$, see Ref. [4] and Fig.32. Note absence of a model describing the pp data on the $\frac{\Sigma^0}{\Lambda}$ ratio at low and high energies.

590

PHOS data support the observation of Σ^0 and $\bar{\Sigma}^0$ by means of the another method of photon detection, as a proof-of-principle.

593

We thank F. Bock and A. Knospe for the detailed discussions.

595 10 References

596 References

- 597 [1] D.D. Chinellato ANA-501, <https://aliceinfo.cern.ch/Notes/node/32>; arXiv:1211.7298;
- 598 [2] D.D. Chinellato, L. Bianchi, R.D. de Souza, ANA-2593, <https://aliceinfo.cern.ch/Notes/node/429>;
- 599 [3] ATLAS collab. arXiv:1111, CERN-PH-EP-2011.
- 600 [4] M. Acciarri et al, Phys. Lett. B 479 (2000) 79-88.
- 601 [5] G.Van Buren arXiv:nucl-ex/0512018.
- 602 [6] M. Abdel-Bary et al., COSY-TOF Collab., Eur.Phys.J A 46, 27-44 (2010).
- 603 [7] P.Huhn, PF 9.01.2017, <https://indico.cern.ch/event/597358/>; J.Otwinowski, APW, 7.03.2016,
604 <https://indico.cern.ch/event/503876>.
- 605 [8] J. Felix Modern Physics Letters A, Vol.14, 13 (1999), 827-842.
- 606 [9] J. Ellis and D.S. Hwang Eur. Phys. J. C (2012) 72:1877.
- 607 [10] E.C. Dukes et al., Phys. Let. B, Vol. 193, 1 (1987), 135-139.
- 608 [11] ALICE collab., arXiv:1606.07424 [nucl-ex],
- 609 [12] M. Floris, F. Fionda, ALICE analysis note ANA-3048, <https://aliceinfo.cern.ch/Notes/node/478>.
- 610 [13] A. Borissov, ALICE analysis note ANA-1683, <https://aliceinfo.cern.ch/Notes/node/321>.
- 611 [14] A. Borissov, ALICE analysis note ANA-2589, <https://aliceinfo.cern.ch/Notes/node/423>.
- 612 [15] N.V. Schmidt, L. Altenk, F. Bock, D.Mühlheim, K. Reygers, ALICE analysis note ANA-3460,
613 <https://aliceinfo.cern.ch/Notes/node/567>.
- 614 [16] ALICE collab., Phys. Lett. B 754 (2016) 235-248.
- 615 [17] ALICE collab., EPJC 75 (2015) 146.
- 616 [18] F.Bock et al., ALICE analysis note ANA-1052, <https://aliceinfo.cern.ch/Notes/node/217>.
- 617 [19] ALICE Collaboration, Int. J. Mod. Phys. A **29**, 1430044 (2014).
- 618 [20] ALICE Collaboration, Eur. Phys. J. C **75** (2015) 75:1.
- 619 [21] ALICE Collaboration, Eur. Phys. J. C **71**, 1594 (2011).
- 620 [22] B. Abelev et al., ALICE Collaboration, Physics Letters B 728 (2014) 2538.
- 621 [23] F. Bock et al., ALICE analysis notes ANA-120 and ANA-118 in
622 <https://aliceinfo.cern.ch/Notes/node/51> and <https://aliceinfo.cern.ch/Notes/node/50>.
- 623 [24] J. Song, A. Borissov, ALICE analysis note ANA-2559, <https://aliceinfo.cern.ch/Notes/node/409>.
- 624 [25] K.A. Olive et al. (Particle Data Group), Chin. Phys. C, 38, 090001 (2014).
- 625 [26] C. Tsallis, J. Stat. Phys. **52**, 479 (1988).
- 626 [27] E. Schnedermann, J. Sollfrank, J. and U.W. Heinz, U.W. Phys. Rev., C48, 2462-2475, 1993; arXiv:
627 nucl-th/9307020. doi = "10.1103/PhysRevC.48.2462"

- [28] B.I. Abelev et al, STAR collab., Phys. Rev., C79, 034909”, 2009.
- [29] J. Adams et al, STAR collab., Phys. Rev., C71, 064902, 2005; arXiv: nucl-ex/0412019v2.
- [30] P. Koch and J. Rafelski, Nucl. Phys. A **444**, 678 (1985).

Data [b-f]	N_{MB}	N_{norm}	$\frac{N_{out}}{N_{MB}}$	$\frac{N_{vertexZ}}{N_{MB}}$	$\frac{N_{mvtxcontr}}{N_{MB}}$	$\frac{N_{pileup}}{N_{MB}}$
Σ^0	4.28e8	3.81e8	0.815	0.087	0.081	0.016
PCM	4.64e8	4.16e8	0.819	0.082	0.087	0.013
MC [b-f]						
Σ^0	4.39e8	3.98e8	0.820	0.085	0.094	0.000
PCM	4.64e8	4.20e8	0.820	0.085	0.094	0.000

Table 2: Comparison of event selection with PCM analysis tabulated for pass-4 2010 pp data.

Data [d]	N_{MB}	N_{norm}	$\frac{N_{out}}{N_{MB}}$	$\frac{N_{vertexZ}}{N_{MB}}$	$\frac{N_{mvtxcontr}}{N_{MB}}$	$\frac{N_{pileup}}{N_{MB}}$
Σ^0	1.11e8	9.68e	0.79	0.105	0.09	0.012
PCM	1.58e8	1.39e8	0.79	0.104	0.09	0.010
Data [e]						
Σ^0	1.29e8	1.11e8	0.80	0.110	0.07	0.018
PCM	1.31e8	1.14e8	0.79	0.112	0.09	0.008

Table 3: Comparison of event selection with PCM analysis tabulated for pass-2 2010 pp data.

Data	N_{MB}	N_{norm}	$\frac{N_{out}}{N_{MB}}$	$\frac{N_{vertexZ}}{N_{MB}}$	$\frac{N_{mvtxcontr}}{N_{MB}}$	$\frac{N_{pileup}}{N_{MB}}$
Σ^0 b	2.67e7	2.64e7	0.900	0.004	0.092	0.003
PCM b	2.74e7	2.71e7	0.900	0.004	0.092	0.003
Σ^0 c	5.12e7	4.98e7	0.887	0.009	0.086	0.017
PCM c	7.59e7	7.39e7	0.888	0.009	0.087	0.016
Σ^0 d	1.21e8	1.05e8	0.792	0.107	0.089	0.012
PCM d	1.75e8	1.53e8	0.795	0.103	0.089	0.013
Σ^0 e	1.83e8	1.57e8	0.797	0.112	0.071	0.019
PCM e	1.47e8	1.27e8	0.795	0.113	0.081	0.011
Σ^0 f	4.69e7	4.21e7	0.821	0.071	0.083	0.025
PCM f	3.89e7	3.53e7	0.822	0.068	0.091	0.019
MC [b-f]						
Σ^0 b	2.87e7	2.86e7	0.906	0.004	0.091	0.
PCM b	2.79e7	2.78e7	0.905	0.004	0.091	0.
Σ^0 c	7.00e7	6.87e7	0.889	0.018	0.093	0.
PCM c	7.29e7	7.22e7	0.898	0.008	0.093	0.
Σ^0 d	1.28e8	1.14e8	0.799	0.105	0.095	0.
PCM d	1.76e8	1.55e8	0.797	0.107	0.096	0.
Σ^0 e	1.66e8	1.45e8	0.790	0.115	0.095	0.
PCM e	1.48e8	1.29e8	0.790	0.115	0.094	0.
Σ^0 f	4.60e7	4.22e7	0.830	0.076	0.094	0.
PCM f	3.98e7	3.66e7	0.832	0.073	0.094	0.

Table 4: Comparison of event selection with PCM analysis tabulated for pass-4 2010 pp data splitted per period of data taking (b,c,d,e,f).

631 11 Appendices

632 11.1 Comparison of selected events with the analysis of PCM group

633 Below are tables of the comparison of the selected events for pass-4 and pass-2 2010 pp data productions
634 from the current, labeled as Σ^0 , and PCM group analysis. For the details of PCM analysis see Ref. [15].

635 11.2 Run lists used for the comparison of pass-2 and pass-4 productions of 2010 pp data

636 Lists of good quality runs used for the comparison of pass-2 and pass-4 productions:

637 2010 d runs:

638 122374 124751 125097 125296 125848 126004 126007 126008 126073 126078
639 126081 126082 126088 126090 126097 126158 126160 126168 126283 126284
640 126285 126351 126352 126359 126403 126404 126405 126406 126407 126408
641 126409 126422 126424 126425 126432,

642

643 2010 e runs:

644 128494 128503 128504 128582 128605 128609 128611 128615 128677 128678
645 128777 128778 128820 128823 128824 128833 128835 128836 128843 128853
646 128855 128913 129512 129513 129514 129520 129523 129527 129528 129540
647 129586 129587 129599 129639 129641 129647 129650 129652 129653 129659
648 129666 129723 129726 129729 129735 129736 129738 129744 129959 129960
649 129961 130149 130157 130158 130172 130178 130342 130343 130354 130356
650 130517 130519 130696 130704 130793 130795 130798 130799 130834 130840.

651

Binning	dN/dy	$< p_T >$	χ^2/ndf
1.0, 1.5, 2.0, 2.4, 2.8, 3.2, 4., 6.0, 10.0	$0.0283 \pm 0.0045^{.0034}_{.0030}$	$1.1500 \pm 0.0757^{.0656}_{.0379}$	3.5/5
1.0, 1.5, 2.0, 2.4, 2.8, 3.2, 4., 5.0, 8.0	$0.0275 \pm 0.0044^{.0034}_{.0028}$	$1.1603 \pm 0.0780^{.0685}_{.0374}$	3.8/5
1.1, 1.6, 2.0, 2.4, 2.8, 3.2, 4., 6.0, 10.0	$0.0287 \pm 0.0042^{.0031}_{.0029}$	$1.1425 \pm 0.0670^{.0579}_{.0337}$	3.7/5
1.1, 1.6, 2.0, 2.4, 2.8, 3.2, 4., 5.0, 8.0	$0.0280 \pm 0.0045^{.0035}_{.0029}$	$1.1526 \pm 0.0763^{.0666}_{.0372}$	4.0/5
1.1, 1.6, 2.0, 2.4, 2.8, 3.4, 4., 5.0, 8.0	$0.029470 \pm 0.0050^{.0039}_{.0032}$	$1.1292 \pm 0.0814^{.0701}_{.0415}$	6.3/5
1.2, 1.6, 2.0, 2.4, 2.8, 3.2, 4., 6.0, 10.0	$0.0303 \pm 0.0054^{.0043}_{.0033}$	$1.1202 \pm 0.0777^{.0666}_{.0401}$	3.8/5
1.2, 1.6, 2.0, 2.4, 2.8, 3.2, 4., 5.0, 8.0	$0.0295 \pm 0.0056^{.0044}_{.0034}$	$1.1298 \pm 0.0870^{.0741}_{.0455}$	3.8/5
1.3, 1.6, 2.0, 2.4, 2.8, 3.2, 4., 6.0, 10.0	$0.0335 \pm 0.0071^{.0061}_{.0038}$	$1.0765 \pm 0.0843^{.0703}_{.0466}$	2.0/5
1.3, 1.6, 2.0, 2.4, 2.8, 3.2, 4., 5.0, 8.0	$0.0285 \pm 0.0055^{.0045}_{.0032}$	$1.1400 \pm 0.0886^{.0752}_{.0470}$	4.0/5
1.3, 1.8, 2.1, 2.4, 2.8, 3.2, 4., 5.0, 8.0	$0.0284 \pm 0.0057^{.0047}_{.0033}$	$1.1492 \pm 0.0928^{.0765}_{.0526}$	7.8/5
1.4, 1.7, 2.0, 2.4, 2.8, 3.2, 4., 5.0, 8.0	$0.0262 \pm 0.0055^{.0048}_{.0027}$	$1.1757 \pm 0.0922^{.0774}_{.0501}$	8.8/5
1.4, 1.8, 2.1, 2.4, 2.8, 3.2, 4., 5.0, 8.0	$0.0283 \pm 0.0061^{.0052}_{.0033}$	$1.1475 \pm 0.0941^{.0763}_{.0551}$	7.9/5

Table 5: Raw yields and mass fit results at different p_T -binnings

652 **11.3 Optimization of p_T -bins of Σ^0 spectrum**

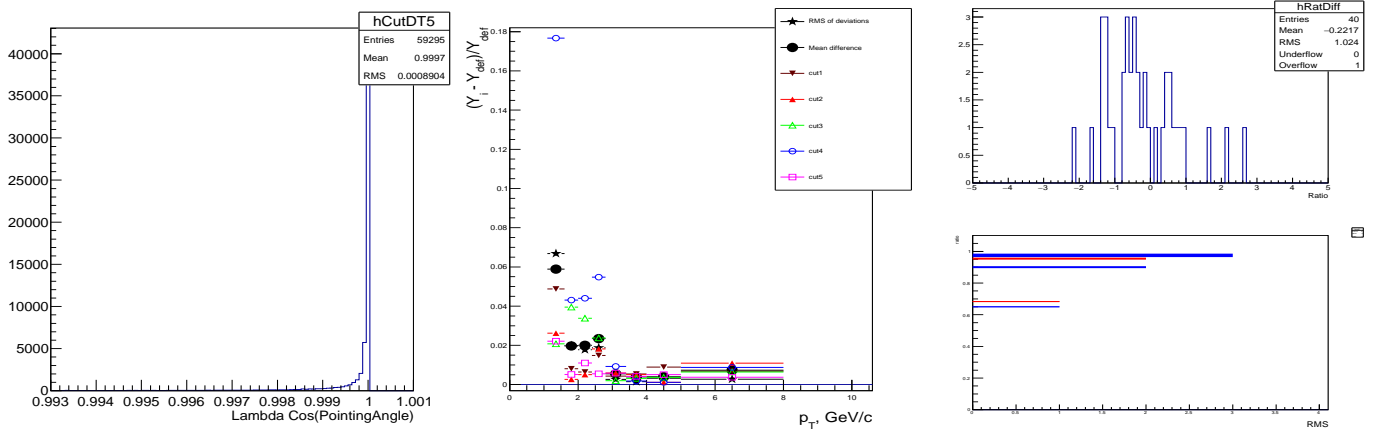


Fig. 34: $\cos \Lambda$ pointing angle, standard deviation (black star) mean deviation and Barlow check Variations from 0.993: $\cos PA > 0.9990, 0.9994, 0.9996, 0.9998, 0.9999$.

653 11.4 Systematic studies of Λ detection

654 D.D.Cinellato node 429 M.Floris node 478
Topological Variable

V0 transv. decay radius > 0.50 cm
DCA Negative Track to PV > 0.06 cm
DCA Positive Track to PV > 0.06 cm
V0 Cosine of Pointing Angle > 0.995
DCA V0 Daughters $< 1.0\sigma$

Selection

V0 Vertex Type with Offline Vertexer
Rapidity Interval $|y| < 0.5$
Proper Lifetime (mL/p) < 30 cm
Competing V0 Rejection 10 MeV /c2
TPC dE/dx Selection (Real data only) $< 5\sigma$
Primary Selection (MC Only)
MC Only PDG for V0 and for daug. tracks
Tracking flags for daughters kTPCrefit
Daughter Tr. Pseudrap $|\eta| < 0.8$
Daughter Tr. Ncrossedrows > 70
Daughter Tr. Ncrossed /N findable > 0.8

This analysis
Topological Variable

V0 transv. decay radius < 180 cm, 0.5-syst
DCA Negative Track to PV > 0.06 cm
DCA Positive Track to PV > 0.06 cm
V0 Cosine of PA > 0.993 , syst > 0.995
DCA V0 Daughters -NO, syst $< 1.0\sigma$

Selection

V0 Vertex Type with ON-line Vertexer, as γ
Rapidity Interval only $\Sigma^0 |y| < 0.5$
Proper Lifetime (mL/p) NO, syst < 30 cm
Competing V0 Rej. NO, syst 10 MeV /c2
TPC dE/dx Selection NO, syst $< 5\sigma$
Primary Selection (MC Only)
MC Only PDG for V0 and for daug. tracks
Tracking flags for daughters YES kTPCrefit
Daughter Tr. No, can be syst rapid. $|\eta| < 0.8$
Daughter Tr. No, see syst Ncrossedrows > 70
Daughter Tr. No, see syst Ncros. /N find. > 0.8

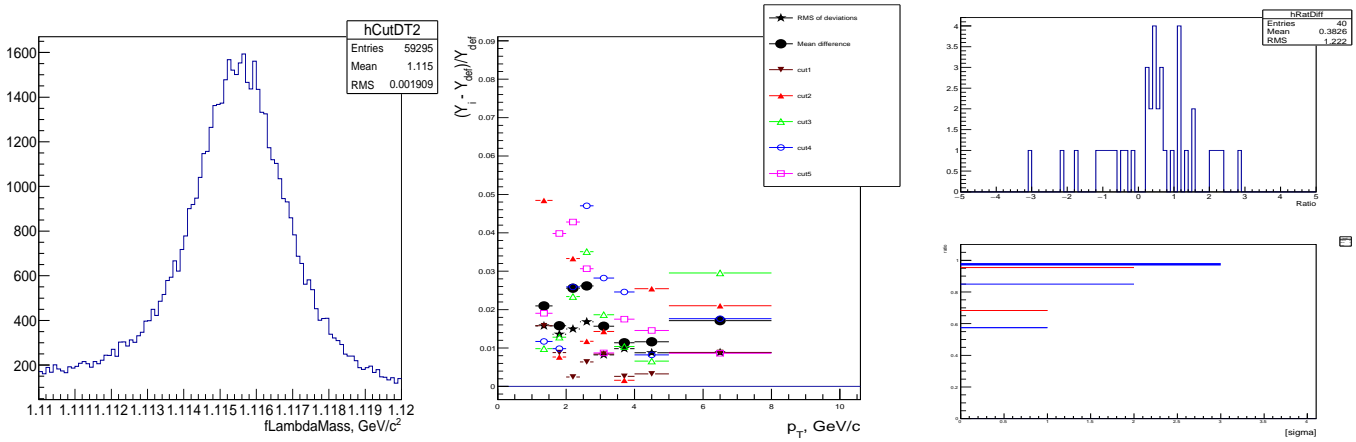


Fig. 35: Λ invariant mass region and standard deviation (black star) mean deviation and Barlow check. Base: min = 1.111, variations of min 1.110 ; 1.112 ; 1.113 ; 1.114 ; 1.115. Base max = 1.120, variations of max 1.120 ; 1.119 ; 1.118 ; 1.117 ; 1.116.

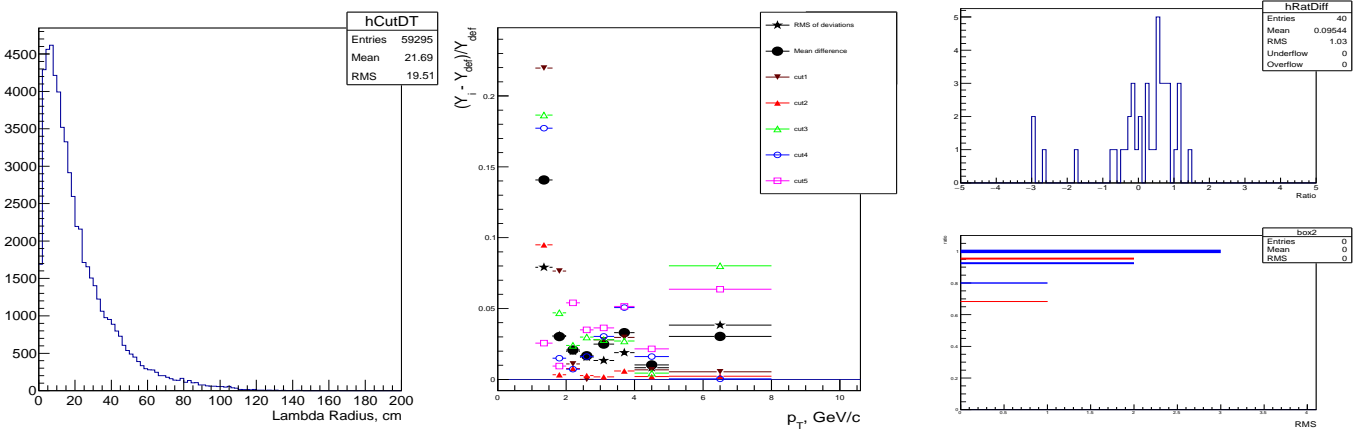


Fig. 36: Λ radius $R = \sqrt{x_{V0}^2 + y_{V0}^2}$. Variations from $R > 0.5$ cm: 2.0, 4.0, 5.0, 6.0, 8.0 cm.

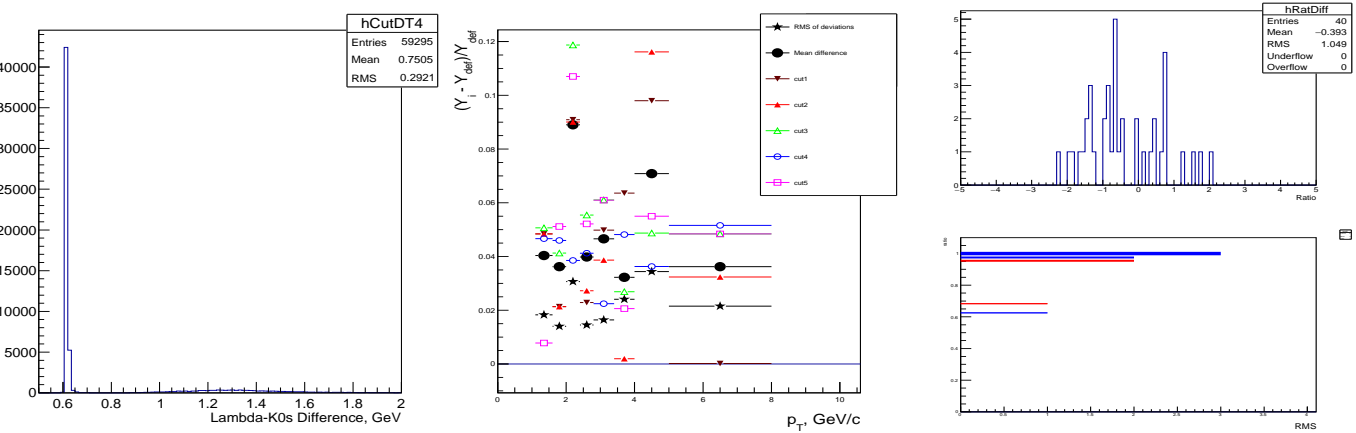


Fig. 37: $\Lambda : M_\Lambda - M_{K_0^s}$. Base: min = 0.8, variations of min 0.5 ; 0.5 ; 0.5 ; 0.5 ; 0.6 ; base max = 0.75, variations of max 2.0 ; 1.5 ; 1.2 ; 0.9 ; 2.0.

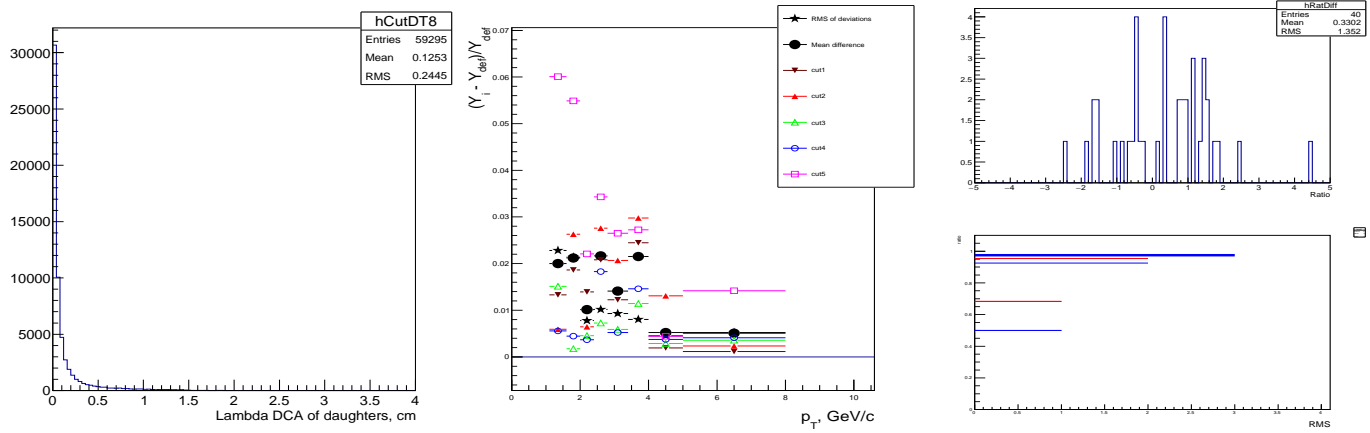


Fig. 38: DCA daughters, standard deviation (black star) mean deviation and Barlow check. Variations from DCA < 4.0 cm: 1.0, 0.8, 0.6, 0.4, 0.2 cm.

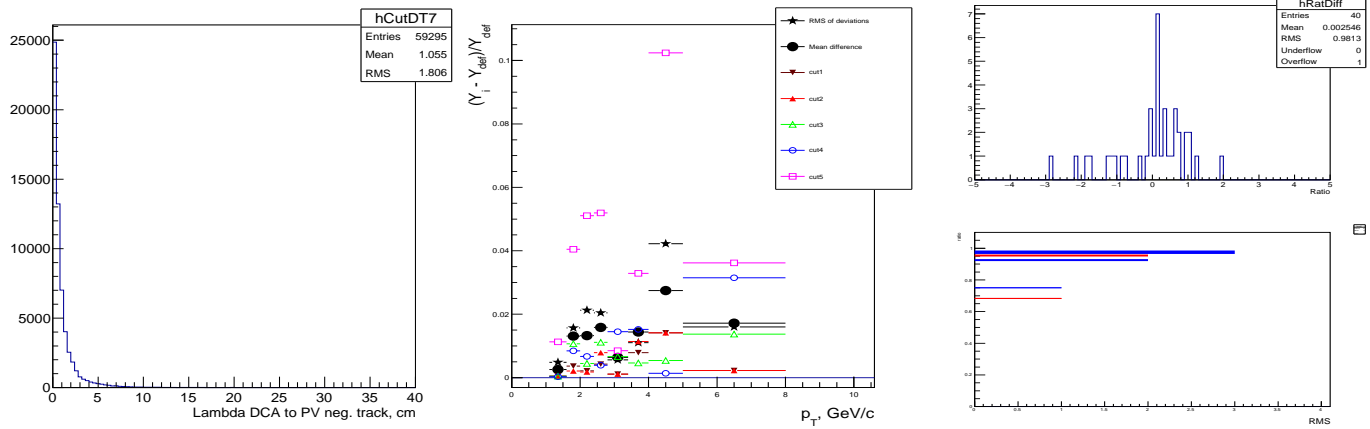


Fig. 39: DCA to PV negative track, its standard deviation (black star) mean deviation and Barlow check. Variations from DCA < 40.0 cm: 10.0, 8.0, 6.0, 4.0, 2.0.

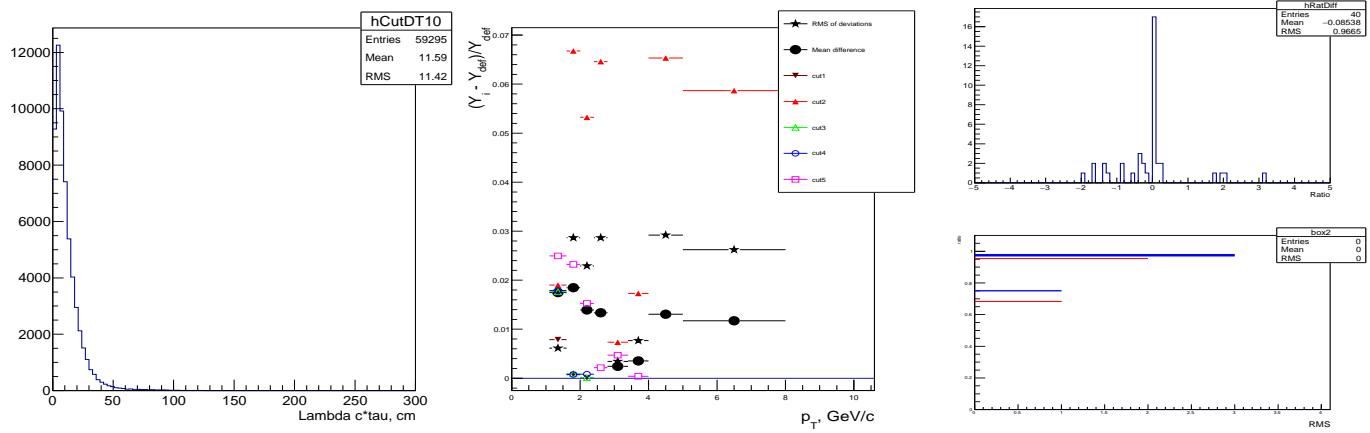


Fig. 40: $\Lambda c \times \tau$, its standard deviation (black star) mean deviation and Barlow check Variations from $c \times \tau < 120$ cm: 100.0, 90.0, 80.0, 70.0, 50.0.

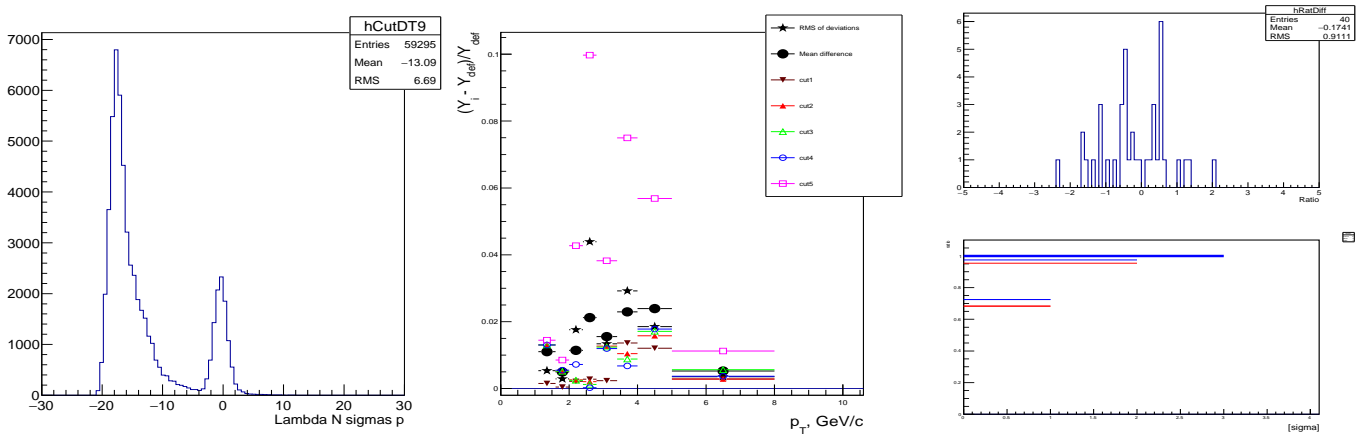


Fig. 41: Λ N sigmas p, its standard deviation (black star) mean deviation and Barlow check. Base: min = -25, variations of min -22.0 ; -20.0 ; -20.0 ; -20.0 ; -20.0 . Base max = 15, variations of max 22.0 ; 20.0 ; 10.0 ; 5.0 ; 0.0. fPIDResponse->NumberOfSigmasTPC(pTrack, AliPID::kProton);

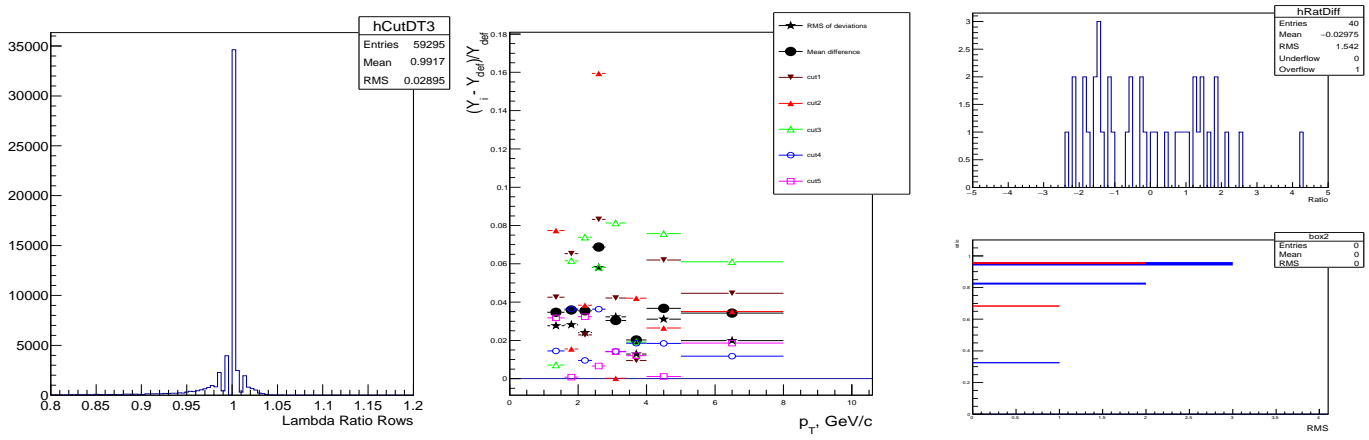


Fig. 42: Λ ratio TPC raws, its standard deviation (black star) mean deviation and Barlow check. Base: min = 0.8, variations of min 0.9 ; 0.92 ; 0.94 ; 0.96 ; 0.98. Base: max = 1.5, variations of max 1.1 ; 1.08 ; 1.06 ; 1.04 ; 1.02.

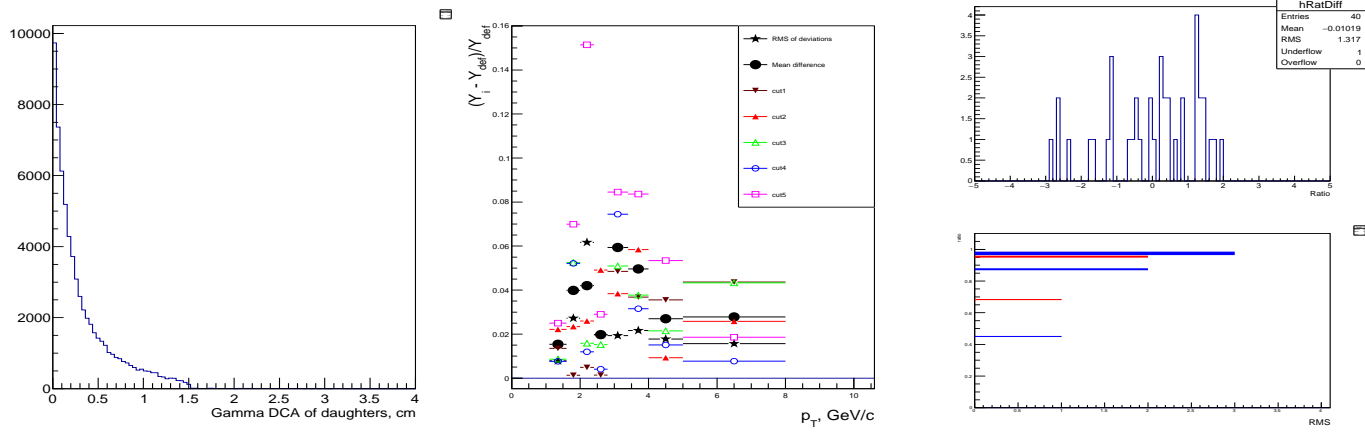


Fig. 43: γ DCA daughters. Base: max = 2.0, variations of max 1.2 ; 1.0 ; 0.8 ; 0.6 ; 0.4.

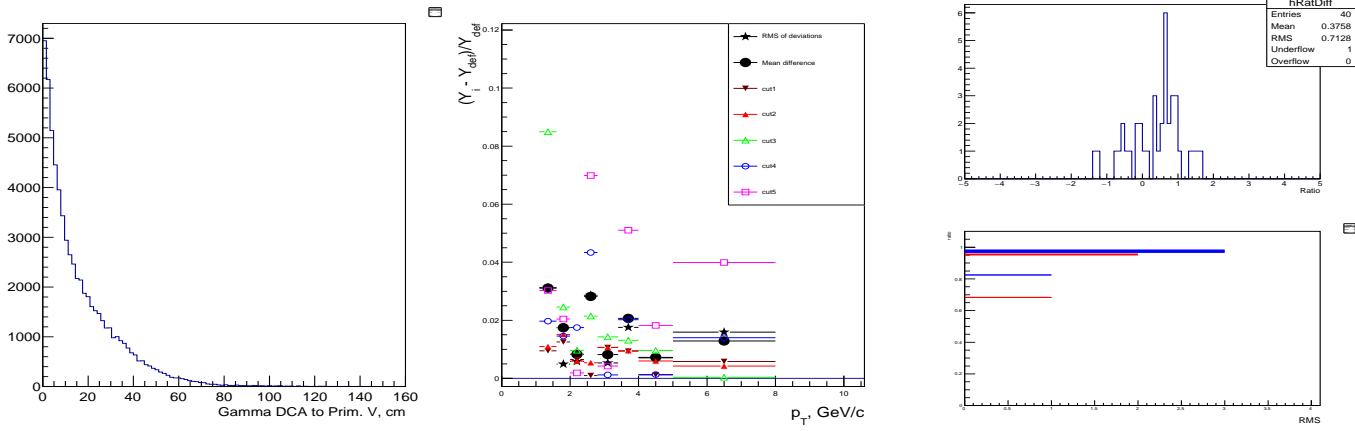
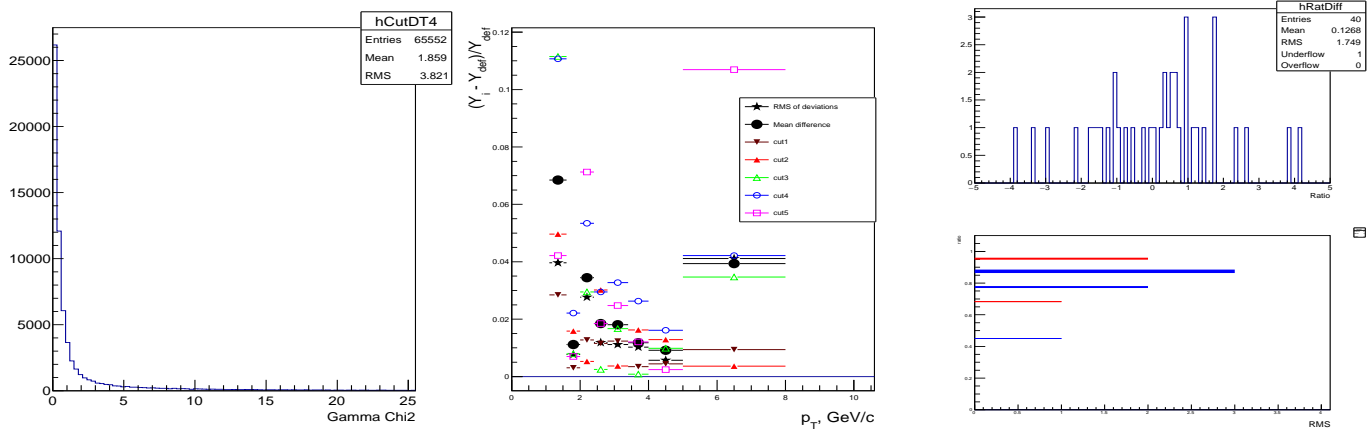
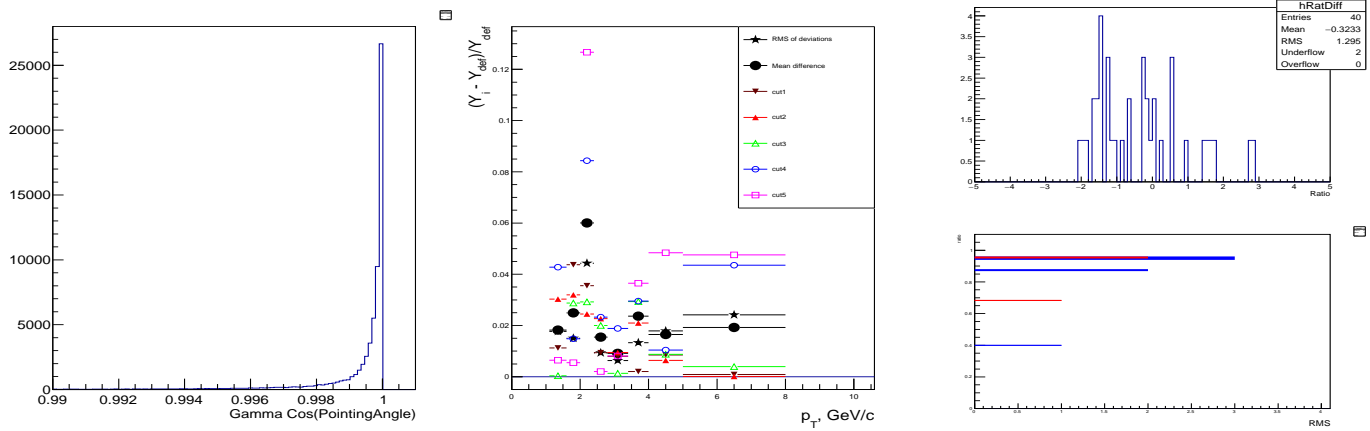
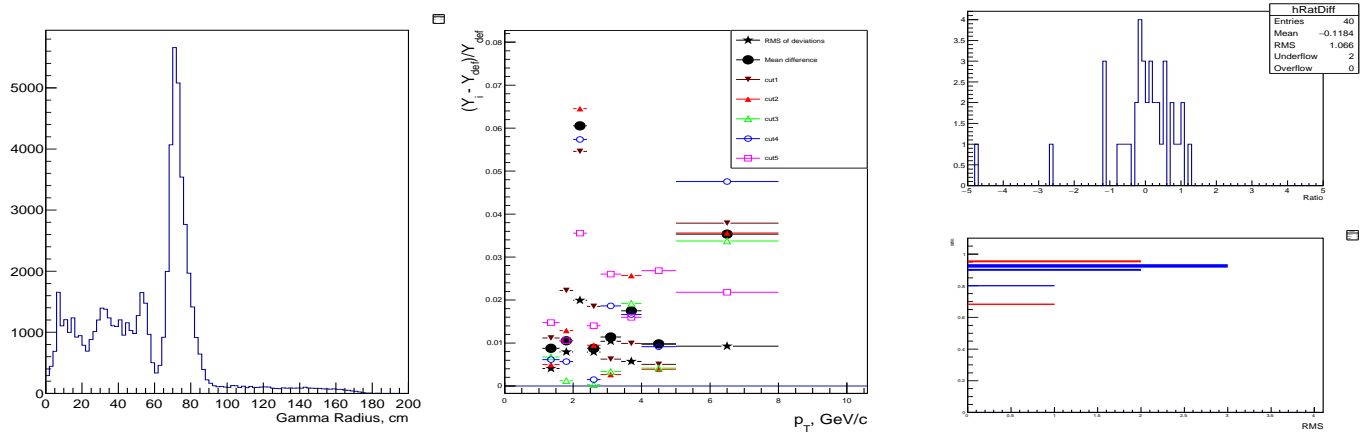


Fig. 44: γ DCA to PV. Base: min = 0.990, variations of min 0.993 ; 0.994 ; 0.996 ; 0.998 ; 0.999.

655 11.5 Systematic studies of γ detection


Fig. 45: $\gamma \chi^2$. Base: max = 25, variations of max 15. ; 10. ; 5. ; 3. ; 1.5.

Fig. 46: $\gamma \cos(\text{PA})$ Base: min = 0.990, variations of min 0.993 ; 0.994 ; 0.996 ; 0.998 ; 0.999.

Fig. 47: γ Radius = $\sqrt{x_{V0}^2 + y_{V0}^2}$. Base: min = 0, variations of min 0.00 ; 5.00 ; 5.00 ; 5.00 ; 7.00. Base: max = 200, variations of max 100. ; 100. ; 90.0 ; 85.0 ; 85.0.

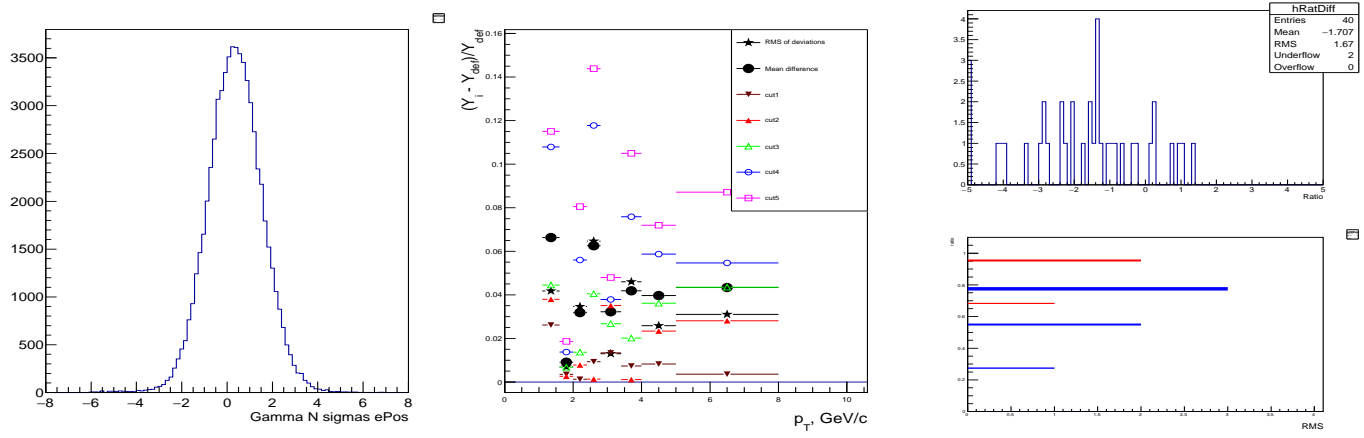


Fig. 48: $\gamma N \sigma e^+$. Base: min = -8, variations of min -4. ; -3 ; -2.5 ; -2.0 ; -1.8. Base: max = 8, variations of max 4. ; 3. ; 2.5 ; 2.0 ; 1.8.

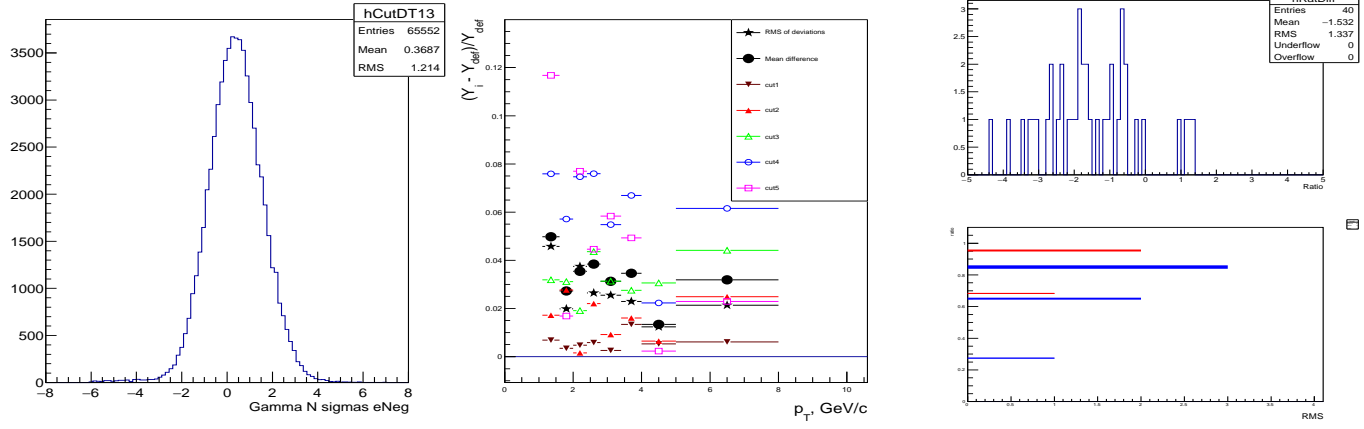


Fig. 49: $\gamma N \sigma e^-$ Base: min = -8, variations of min -4. ; -3 ; -2.5 ; -2.0 ; -1.8. Base: max = 8, variations of max 4. ; 3. ; 2.5 ; 2.0 ; 1.8.

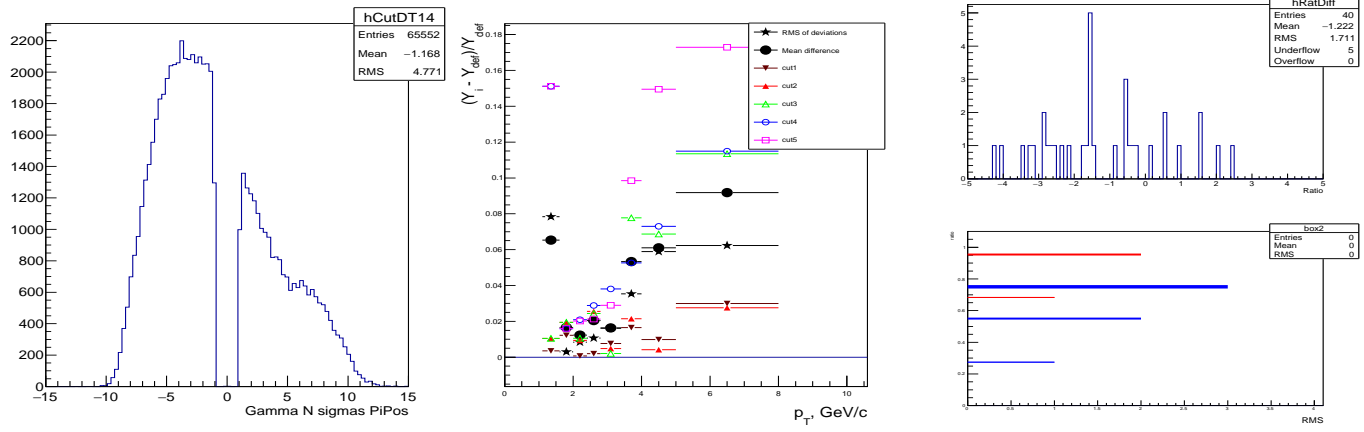


Fig. 50: $\gamma N \sigma \pi^+$. Base: min = -15, variations of min -9. ; -8. ; -8. ; -7. ; -7. Base: max = 15, variations of max 11. ; 10. ; 9. ; 9. ; 8.

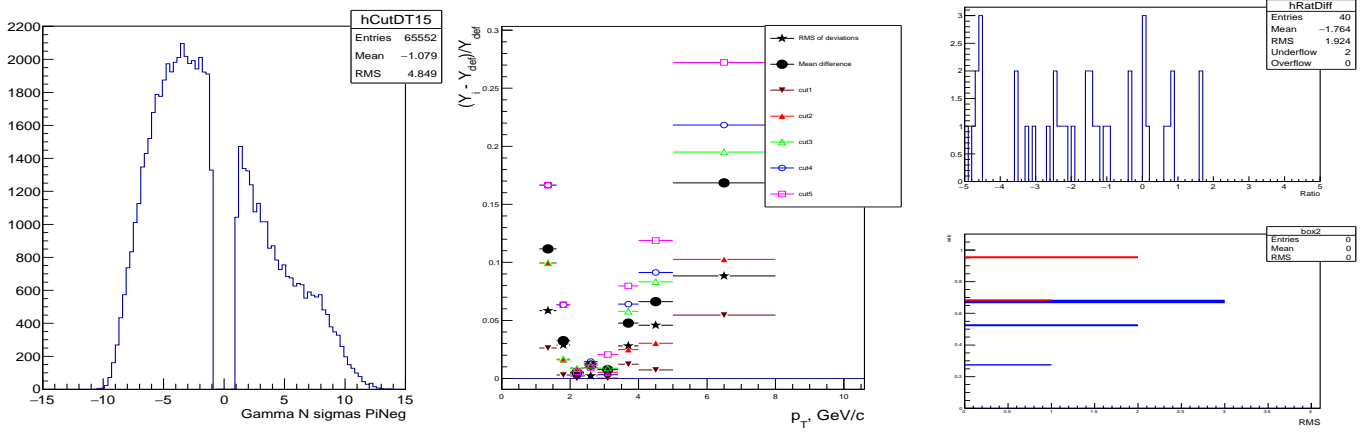


Fig. 51: $N \sigma\pi^-$. Base: min = -15, variations of min -9. ; -8. ; -8. ; -7. ; -7. Base: max = 15, variations of max 11. ; 10. ; 9. ; 9. ; 8.

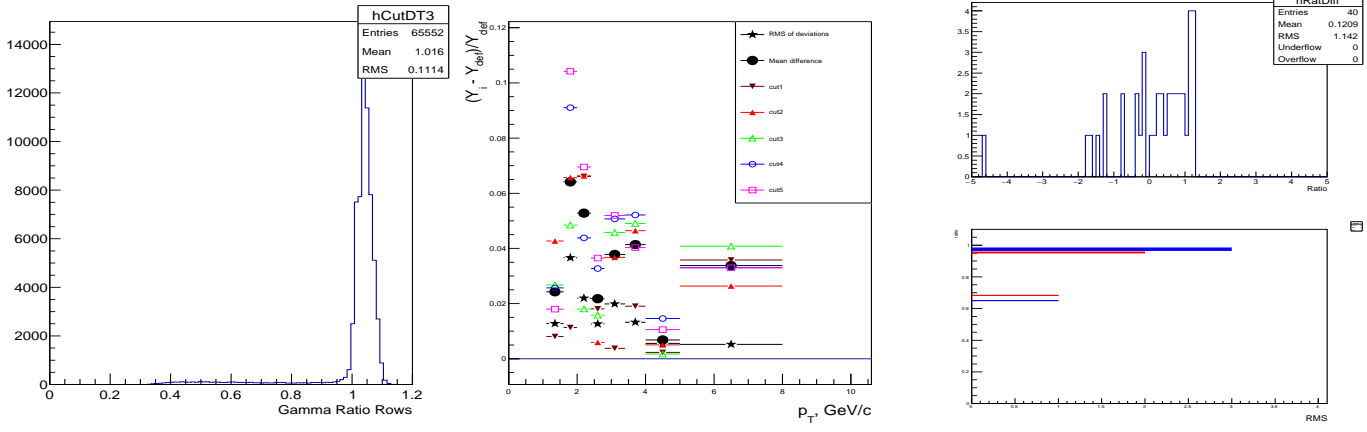


Fig. 52: γ ratio TPC rows. Base: min = 0.3, variations of min 0.9 ; 0.92 ; 0.94 ; 0.96 ; 0.97 Base: max = 1.2, variations of max 1.1 ; 1.08 ; 1.075 ; 1.072. ; 1.071.

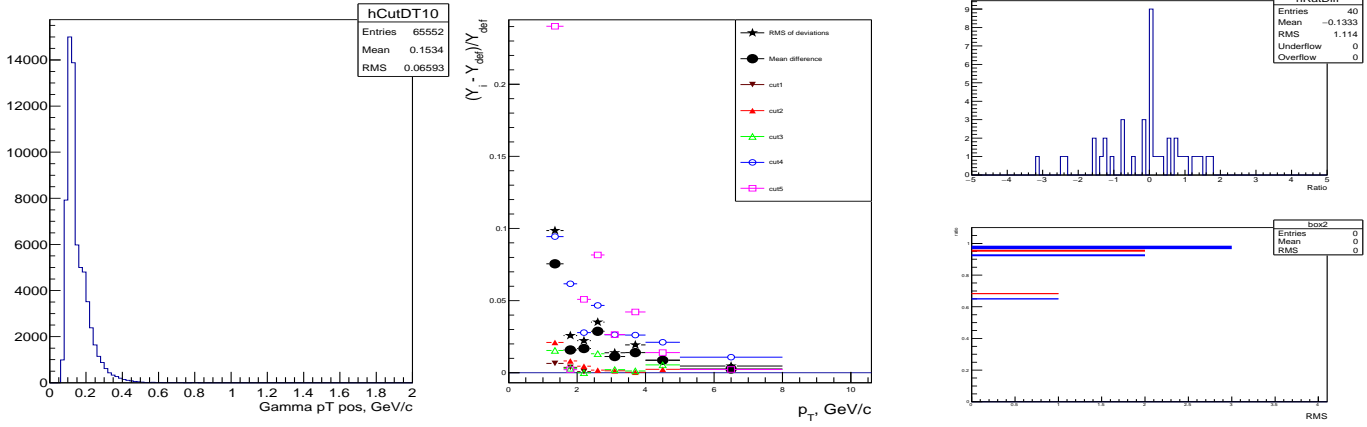


Fig. 53: $\gamma p_T e^+$. Base: min = 0.5, variations of min 0.6 ; 0.7 ; 0.8 ; 0.9 ; 1.0.

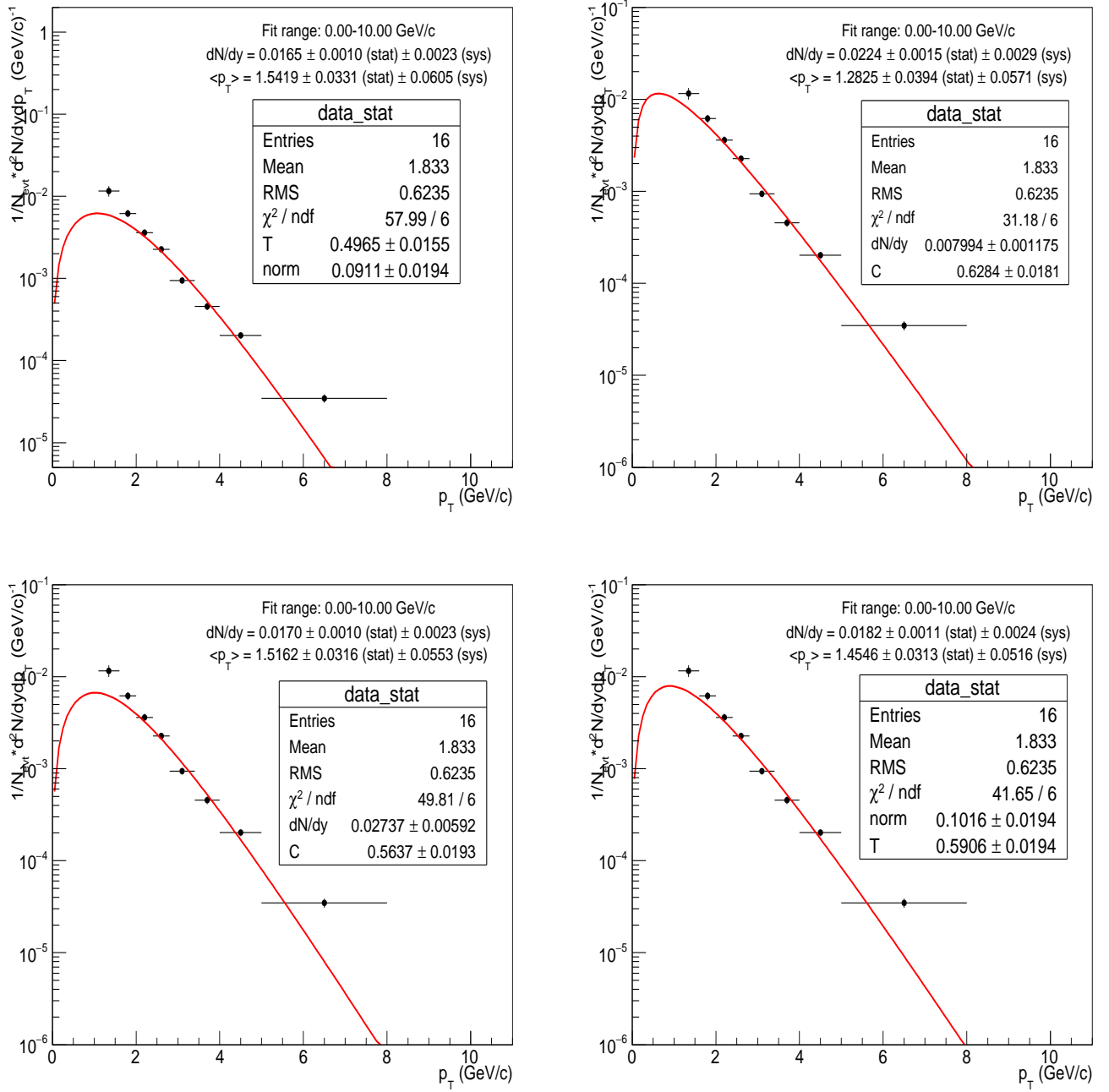


Fig. 54: The transverse momentum spectrum of $(\Sigma^0 + \bar{\Sigma^0})/2$ fitted with Boltzmann, pT, mT and Bose-Einstein fits.

656 **11.6 Fits of Σ^0 spectrum resulting to large values of χ^2/NDF**

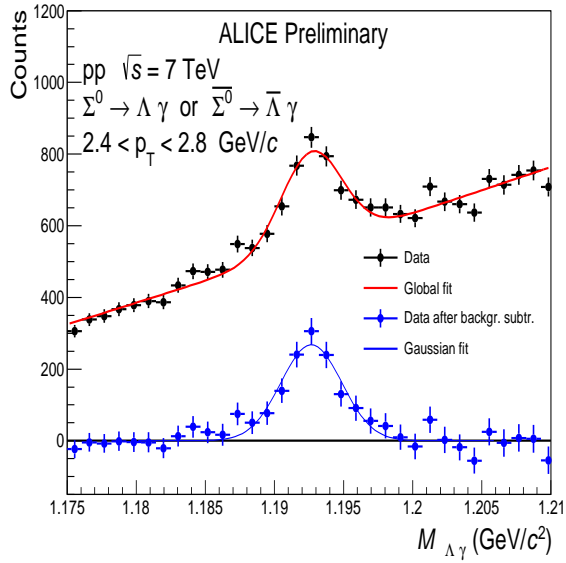


Fig. 55: Polynomial background plus Gauss fit of invariant mass of the detected conversion photon and $\Lambda(\bar{\Lambda})$

657 11.7 ALICE Preliminary plots of Σ^0 and/or $\bar{\Sigma}^0$ mass and width

658 The fitted invariant mass distributions of separated Σ^0 and $\bar{\Sigma}^0$ data in different p_T bins are presented
659 correspondingly in the left and right plot of Fig. 56 before and after background subtraction.

660 The fit results on the mass and width of separately analyzed Σ^0 and $\bar{\Sigma}^0$ in different p_T bins are presented
661 in Fig. 57. Fits of the data give a mass of 1192.64 ± 0.13 MeV/c² and a resolution of 2.14 ± 0.13 MeV/c²
662 for the Σ^0 and a mass of 1192.66 ± 0.14 MeV/c² and a resolution of 2.20 ± 0.17 for the $\bar{\Sigma}^0$. One can
663 see that the mass and width of separately analyzed Σ^0 and $\bar{\Sigma}^0$ baryons are in agreement with each other
664 within the statistical uncertainties, that allows the analysis of the combined Σ^0 and $\bar{\Sigma}^0$ data.

665 The fit results on the mass and width of combined Σ^0 and $\bar{\Sigma}^0$ data in different p_T bins are presented in
666 Fig. 58. The fit results of the combined of $\Sigma^0 + \bar{\Sigma}^0$ Monte Carlo data from PYTHIA+PHOJET generators
667 are shown in Fig. 58 as red squares. From the combined data on Σ^0 and $\bar{\Sigma}^0$ its mass $M^{\Sigma^0 + \bar{\Sigma}^0} = 1192.65 \pm$
668 0.099 MeV, see Fig. 58 left plot. The mass of Σ^0 ($\bar{\Sigma}^0$) extracted from simulated events is $M = 1192.43 \pm$
669 0.13 MeV. The measured mass of the Σ^0 hyperon is in full agreement with the PDG value of Σ^0 ($\bar{\Sigma}^0$),
670 which is $M^\Sigma = 1192.642 \pm 0.024$ MeV, see Ref. [25].

671 The mean width of the mass distribution extracted from combined data on Σ^0 and $\bar{\Sigma}^0$ is $\sigma_{M^{\Sigma^0 + \bar{\Sigma}^0}} = 2.27 \pm$
672 0.12 MeV, Fig. 58 right plot. The mean width of mass distribution of simulated events is $\sigma^{MC} = 2.08 \pm$
673 0.13 MeV.

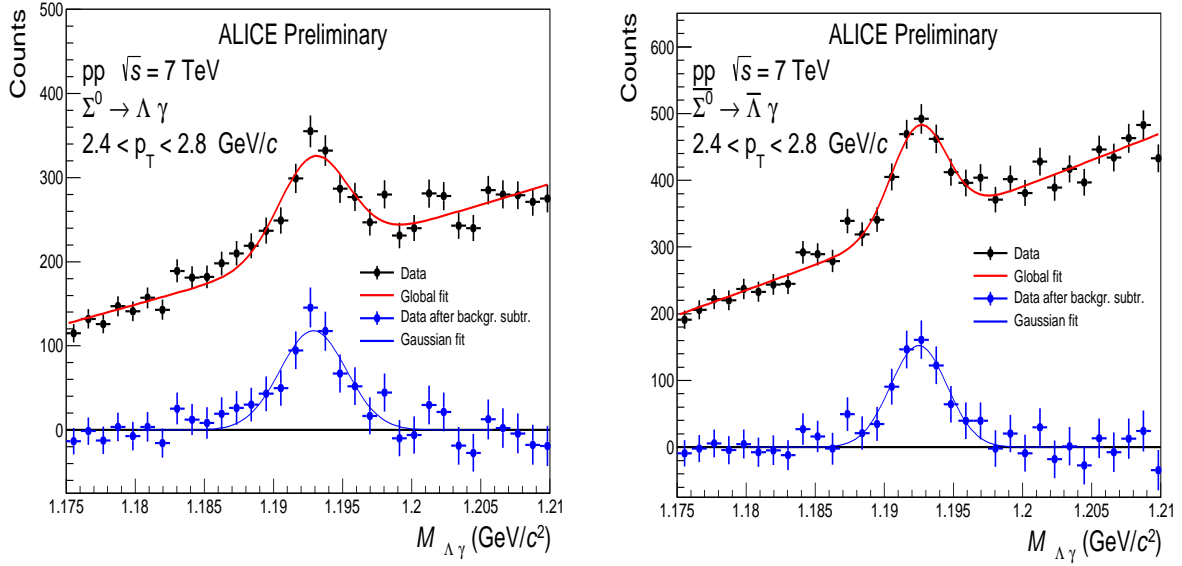


Fig. 56: Polynomial background plus Gauss fit of invariant mass of the detected conversion photon and Λ (left plot) and $\bar{\Lambda}$ (right plot).

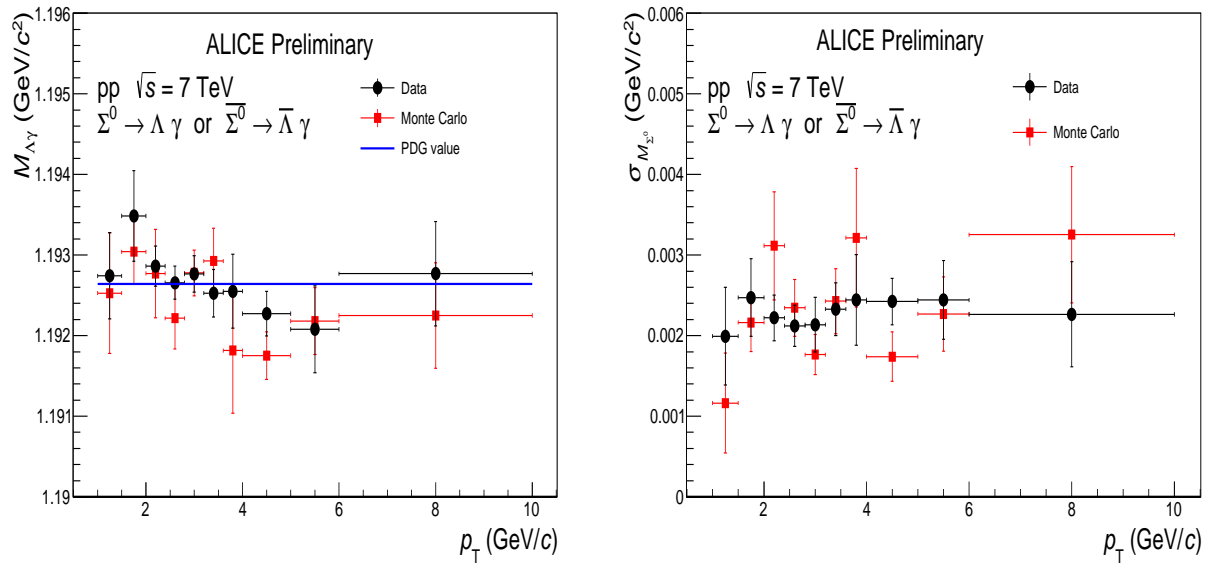


Fig. 57: Mean value (left panel) and width (right panel) of the extracted Σ^0 and $\bar{\Sigma}^0$ invariant mass as functions of p_T bins from 2010 data (black circles) and simulated events (red squares). Blue line represents the PDG value of Σ^0 mass.

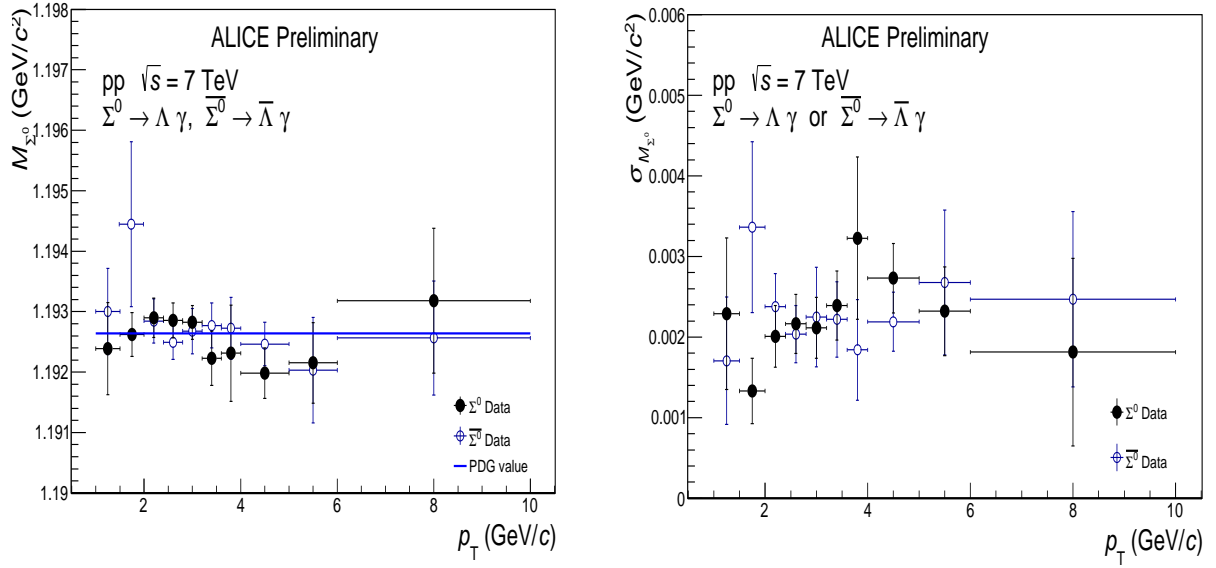


Fig. 58: Left plot: Mean value of the extracted Σ^0 (black circles) and $\bar{\Sigma}^0$ (open blue circles) invariant mass in the p_T bins from 2010 ppdata. Blue line represents the PDG value of Σ^0 mass. Right plot: Width of the extracted Σ^0 (black circles) and $\bar{\Sigma}^0$ (open blue circles) invariant mass in the p_T bins from 2010 ppdata.

674 11.8 $\Sigma^0 \rightarrow \Lambda + \gamma^{PHOS}$ from 2011 d+e data

675 These data have been released for Quark Matter 2014 and are used as a proof-of-principle, see Ref. [13].
 676 Here the resulting plots are added in Fig. 59 for the presentation of the completeness of the analysis.

677

678 The electromagnetic calorimeter PHOS, see Ref. [19], is made of PbWO₄ crystals and has fine granularity
 679 with crystal size $2.2 \times 2.2 \times 18$ cm³. It is located 4.6 m from the interaction point. PHOS subtends $260^\circ <$
 680 $\phi < 320^\circ$ in azimuth and $|\eta| < 0.13$ in pseudorapidity. Its energy resolution is $\Delta E \sim 3\% / \sqrt{E_\gamma(\text{GeV})} \oplus$
 681 1.1%.

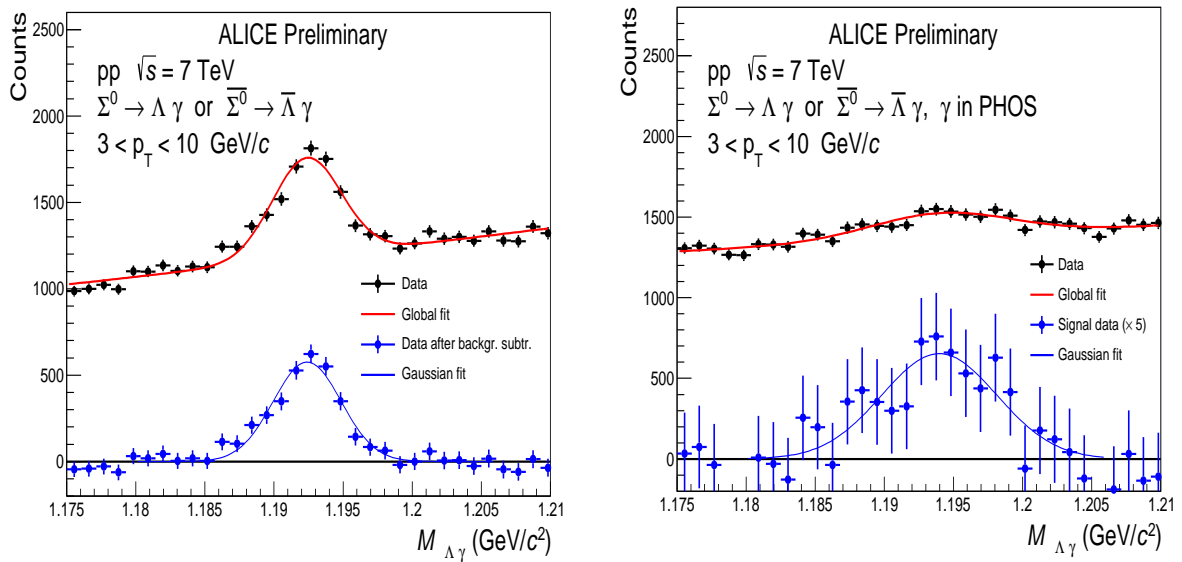


Fig. 59: Invariant mass of $\Lambda \gamma$ and $\bar{\Lambda} \gamma$ pairs, where the Λ or $\bar{\Lambda}$ is detected in the central tracking system and the photon is detected using the PCM (left) or PHOS (right). The red curves are fits to the data using Gauss fits plus fourth-order polynomials to describe the background. The invariant mass distribution after the background subtraction is presented on the bottom part of the plot.